



Università degli studi di Firenze
Scuola di Scienze Matematiche, Fisiche e Naturali

Corso di Laurea Magistrale in Scienze Fisiche
e Astrofisiche

Evidence of superfluidity in a dipolar supersolid through non-classical rotational inertia

Dimostrazione della superfluidità di un supersolido
dipolare tramite effetti di rotazione non classica

CANDIDATO:
Giulio Biagioni

RELATORE:
Prof. Giovanni Modugno

Anno Accademico 2018/2019

Contents

Introduction	3
1 Superfluids and supersolids under rotation	7
1.1 Superfluidity tested by rotations	7
1.2 Leggett’s argument: can a solid be superfluid?	14
1.3 The helium case	20
1.4 Scissors mode and moment of inertia	22
2 Dipolar Quantum Gases	29
2.1 Dipolar interaction	29
2.2 Mean-field approach	33
2.3 Quantum Fluctuations	41
3 Dipolar Supersolids	45
3.1 Soft-core models	45
3.2 Trapped dipolar bosons as a soft-core model	49
3.3 Observation of a dipolar supersolid	57
3.4 Goldstone modes in dipolar supersolids	58
4 How to make a supersolid	67
4.1 Dysprosium	67
4.2 Experimental apparatus	69
4.3 Imaging and fitting	74
5 NCRI in a Dipolar Supersolid	79
5.1 Why the scissors mode?	79
5.2 Measurement of the scissors mode	81
5.3 Moment of inertia and superfluid fraction	87
5.4 Thermal Measurements	93
6 Building an Optical Lattice	97
6.1 Scientific motivation	97
6.2 Characterization of the lattice	100
6.3 Observation of the lattice on the atoms	111
Conclusions	117
Bibliografy	126

Introduction

Quantum mechanics challenges our intuition since the very first days of its laborious birth. The theory deals with a world of which we do not have everyday experience, on scales of length that go from atoms and molecules further down. This is perhaps the reason why macroscopic quantum phenomena are so intriguing and interesting: they bring quantum mechanics on much larger scales. The first evidence of such quantum macroscopic effects came from liquid ^4He , which becomes superfluid under the temperature of 2.17 K, and from the closely related field of superconductors [1]. In the 90s, it has been shown that also the gaseous phase of alkali atoms undergo a transition to a Bose-Einstein condensate (BEC), which possesses superfluid properties [2,3]. The key ingredient in all these systems is the macroscopic occupation of a single quantum state, allowed by the Bose statistic obeyed by their constituents [4]. Given that the classical liquid and gaseous phases have their analog in the quantum realm, we can wonder if this is valid for the solid state too. One could be induced by its intuition to promptly answer no: one of the most distinctive properties of a superfluid is that it can flow without friction, while one of the most distinctive properties of a solid is that it can resist to shear stress, so that the two phases seem incompatible. As it turns out, the answer is, instead, yes: the supersolid exists, and it is the object of this thesis. One possible way to think about the supersolid is as a quantum phase of matter which possesses two kinds of order [5]. In a crystalline solid, the order comes from the fact that atoms (or molecules) are arranged in a periodic lattice, occupying therefore specific points in space. If we call $\delta\rho(\mathbf{r})$ the local deviation of the density from its averaged value, ordering in the solid is expressed as

$$\delta\rho(\mathbf{r}) = \delta\rho(\mathbf{r} + \mathbf{T}), \quad (1)$$

where \mathbf{T} belongs to the discrete set of lattice vectors. Such an ordering is linked to the breaking of space translational symmetry and is absent in a fluid or in a gas. On the other hand, order in a superfluid is a more abstract concept. We define the one-particle density matrix as $n(\mathbf{r}, \mathbf{r}') = \langle \hat{\Psi}^\dagger(\mathbf{r})\hat{\Psi}(\mathbf{r}') \rangle$, where $\hat{\Psi}^\dagger(\mathbf{r})$ ($\hat{\Psi}(\mathbf{r})$) is the field operator which creates (annihilates) a particle at the point \mathbf{r} and the operation $\langle \rangle$ indicates both a quantum mechanical and a statistical average. It is possible to show [3] that the macroscopic occupation of a single quantum state implies that

$$n(s) \xrightarrow{s \rightarrow \infty} n_0, \quad (2)$$

with $s = |\mathbf{r} - \mathbf{r}'|$ and n_0 the fraction of atoms in the condensed state. Eq. (2) expresses the presence of order in the superfluid state, linked to the breaking of

the $U(1)$ symmetry due to the phase acquired by the macroscopic wavefunction. It can be understood as a consequence of the delocalization of the single particle over the whole system: a state in which a particle is removed at the point \mathbf{r} has a finite quantum mechanical amplitude over a state in which an identical particle is removed in another arbitrary point \mathbf{r}' . A supersolid is a state of matter in which the two previous kinds of order exist simultaneously for the same species of particles, featuring both superfluid properties and density modulation.

The first theoretical discussion of a supersolid was made by Gross in 1957 [6]. The first suggestion of a physical mechanism that could be responsible for the occurrence of supersolid order in a quantum crystal came from the papers of Andreev and Lifschitz in 1969 [7] and of Chester in 1970 [8]. The mechanism involves the presence of vacancies in the ground state of a quantum many-body system, that is, the number of atoms is not equal to the number of lattice sites. The vacancies behave as mobile particles since they can move in the lattice through quantum tunnelling. If this happens in a bosonic system, the vacancies obey Bose statistic and can undergo Bose-Einstein condensation. The result is a superfluid flow in a crystalline background, i.e. a supersolid phase. In another seminal paper that appeared in 1970 [9], Leggett suggested that the supersolid should possess a lower moment of inertia than a classical system, in analogy to what happens for ordinary superfluids. Leggett's argument furnished a conceptually simple method to measure the superfluid response of a supersolid, observing its anomalous properties under rotation, often referred to as non-classical rotational inertia (NCRI). In the first phase of the search for supersolidity, the most likely candidate was a crystal of solid ^4He . Thanks to the combination of the light mass of its constituents and weakness of the interatomic potential, solid ^4He offers a promising scenario where to observe strong effects of quantum delocalization of its particles. A breakthrough in the study of supersolid ^4He happened in 2004, when Kim and Chan published two papers [10,11] about the observation of a reduced moment of inertia in solid ^4He . The experiment was the realization of Leggett's original proposal through a torsional oscillator. Since then, many experimental and theoretical works have been performed to understand and interpret the experimental data, an issue that turned out to be problematic [12]. Today it is believed that the experimental results collected so far don't need the existence of supersolid helium to be explained [13].

In the last two decades, the astonishing progress in the degree of control and manipulation of ultracold atoms made experiments on quantum gases an attractive platform where to study quantum many-body physics and simulate condensed matter systems in a highly ideal environment. For what concerns the search for supersolidity, in a quantum gas experiment the starting point is a BEC, a system which obeys the hydrodynamic equations of superfluids [2,3]. The challenge, therefore, contrary to solid helium, is to engineer an interaction that induces the system to break translational invariance. Some theoretical proposals considered a soft-core two-body interaction, which doesn't diverge in the limit of small inter-particles distances. Simulations show that such an interaction produces a supersolid phase in an appropriate range of parameters [14]. Quantum gases of Rydberg atoms might in principle be employed to produce soft-core interactions, but technical challenges have prevented from an effective realization of the theoretical models so far. Striped

phases with supersolid properties have been realized in BECs of spin-orbit coupled atoms (SOC) [15] and atoms in optical cavities [16]. In these two systems, a mechanism of spontaneous symmetry breaking produces a density modulation with a period that is not present *ab initio* in the hamiltonian. However, the resulting supersolid is infinitely stiff: the lattice period is imposed externally by the Raman beams which induce the spin-orbit coupling, in the first case, and by the wavelength of the light in the optical cavities, in the second case. Another possibility is offered by dipolar quantum gases, realized with strongly magnetic atoms that interact with the anisotropic and long-ranged dipolar interaction. Among the many interesting effects which the dipolar interaction produces, there is the rotonization of the excitation spectrum, which possesses a minimum at finite momentum, as in liquid ^4He [17]. The minimum, contrary to SOC and optical cavities BECs, arises genuinely from the interactions between the particles. Tuning the roton gap allows inducing an instability which creates an array of quantum droplets, self-bound systems stabilized by quantum fluctuations [18].

Finally, a supersolid phase has been observed in 2019 in a dipolar gas of dysprosium atoms by the Pisa group directed by Prof. G. Modugno [19]. In a small range of parameters, the dipolar droplets overlap establishing phase coherence thorough the whole system but keeping the density modulation. The result has been promptly confirmed by two other groups in Innsbruck [20] and in Stuttgart [21]. The dipolar supersolid has a different nature compared to the one expected for solid helium: it has thousands of atoms in each lattice site and few sites, of order unity. It is thus also called cluster supersolid. Each cluster is usually called droplet, in analogy with the self-bound dipolar droplets previously observed. In the first experiments the phase coherence between droplets has been observed through the study of the interference pattern which forms after the free expansion of the cloud. A second kind of experiments focused on the excitation modes. Two kind of excitations have been observed, one associated with the crystal lattice and the other with the superfluid background, which correspond to the two Goldstone modes arising from the two broken symmetries of the supersolid [22–24]. Such an observation has demonstrated the supersolid nature of the dipolar system produced in the laboratories, including the compressibility of its crystal structure, a feature lacking in the SOC and optical cavities experiments.

This thesis reports the experimental activity carried out in the Pisa group that I joined in the summer of 2019. The subjects treated here fit in the first experiments which try to understand the intriguing properties of the recently discovered supersolid state of matter. The project aims to study the superfluid response of the dipolar supersolid and understand how it is modified by the crystal structure compared to a homogeneous superfluid. Superfluidity of the dipolar supersolid has been indirectly demonstrated by the experimental observation of the Goldstone modes, whose frequencies are in agreement with those calculated with the hydrodynamics equations of superfluids. However, a direct demonstration of the superfluid properties of the dipolar supersolid is still lacking. In this thesis I describe an experiment which provide such a demonstration, probing the supersolid with a rotational excitation. Together with persistent currents, the reduced response to a rotation is the most spectacular consequence of superfluidity. The anomalous behavior of the

supersolid under rotation has been even proposed, in the seminal paper by Leggett, as the definition itself of supersolidity. The work described in this thesis, indeed, highly inspires to the original Leggett's proposal, despite the many differences that will be highlighted in details, and, therefore, ideally prosecute the first experiments attempted with solid helium. Throughout the thesis, I explain how I have been able to induce a rotational excitation and to observe its effects on the supersolid. I employ a particular excitation mode existing in anisotropic traps, the scissors mode, used also in the past to test superfluidity in ordinary BECs [25], which enables to reduce the measurement of the moment of inertia to a frequency measurement, as in the helium case. From the experimental data I estimate the superfluid fraction, a key quantity for the characterization of the supersolid, which quantifies the fraction of the system that decouples from the rotation. A superfluid fraction equal to one indicates a standard superfluid, like the BEC, while a superfluid fraction equal to zero indicates a classical system. We will see that the supersolid is expected to place itself between these two extremities.

The thesis is organized as follows. In chapter 1, I discuss the link between superfluidity and rotations, highlighting the fact that in many different fields of physics the demonstration of superfluidity of a system has dealt with rotations. Then, I explain what happens to a supersolid under rotation, following the original Leggett's argument. This discussion is useful to understand how a density modulation modifies the superfluid behavior. I also describe the scissors mode, the experimental tool employed to detect rotations in our trapped system. In chapter 2, I review the basic physics of dipolar quantum gases, which is needed for an understanding of our experimental system. In chapter 3, I focus on dipolar supersolids. I propose an analogy between a trapped dipolar system and the soft-core ones previously cited, offering an alternative qualitative understanding of the supersolid formation in the dipolar case. Then I discuss the seminal experiments on the dipolar supersolids. In chapter 4, I describe the experimental apparatus and the experimental procedure employed to create a supersolid. In chapter 5, I report the principal result of this thesis: the measurement of the moment of inertia of the dipolar supersolid. I also estimate a superfluid fraction from the experimental data and make a qualitative comparison with the original Leggett's prediction. Finally, in chapter 6, I describe the construction of an optical lattice for future experiments on the supersolid, related to the Josephson effect between supersolid droplets and to a possible manipulation of the superfluid-supersolid transition. Much of the work reported in this thesis is the object of a scientific article [26], under consideration for the publication by the journal Science.

Ringraziamenti

Mi preme ringraziare il gruppo sperimentale di Pisa, che mi ha accolto negli ultimi mesi: Andrea, Carlo, Luca, Giovanni e Julian, per i momenti passati insieme. Un grazie particolare a Luca, per tutti i consigli che mi ha dato e per quello che mi ha insegnato in laboratorio, e soprattutto a Giovanni, che, oltre ad avermi seguito attentamente, mi ha fatto vedere, per la prima volta, cosa significa *fare* fisica, e non solo *studiare* fisica.

Chapter 1

Superfluids and supersolids under rotation

In this chapter, we discuss the properties of superfluids and supersolids under rotation. First, we briefly review some of the basic features of superfluids, especially the ones linked with rotations, highlighting their generality through a list of experiments in different fields and from different years. We then present in detail Leggett's idea of a supersolid, which comes directly from the peculiar properties it should exhibit under rotation, halfway between a rigid solid and a superfluid. We briefly review the attempts made to observe such effects in solid helium, without success, and finally, we discuss a method for the measurement of the moment of inertia of a quantum gas, the scissors mode, used in this thesis.

1.1 Superfluidity tested by rotations

The complex of phenomena that are collected under the term superfluidity concerns a number of different physical systems, signaling the extreme generality of the field. We can think of a superfluid as something which transports some kind of "charge" without friction. Historically, superfluidity was discovered in liquid helium, when Kapitza [27] and Allen and Misener [28] found that under the critical temperature of 2.17 K helium could flow in narrow channels with no detectable viscosity. In this case, the frictionless flow is a mass flow of the ^4He atoms. Some years before, Onnes discovered that the electrical resistance of mercury drops to zero under the temperature of 4.2 K: it was the first evidence of superconductivity. Today, superconductors are counted in the class of superfluids system, being seen as charged superfluids. In this case, the quantity to be transported without friction is, of course, the electrical charge. Superfluidity in a fermionic system, such as the electronic gas in metals, is explained by the BCS theory [1]. In this case, the formation of Cooper pairs, which obey the Bose statistic, is needed for the macroscopic quantum mechanical occupation of a single state. Superfluidity of neutral fermions is shown by ^3He , the fermionic isotope of helium [1]. Other superfluids are proton and neutron clouds in nuclei, whose superfluidity is thought to play a significant role in extreme astrophysical situations such as the core of neutron stars [29]. More recent laboratory-systems showing superfluidity are the Bose-Einstein condensates and degenerate Fermi gases

realized in ultracold and dilute atomic samples [2, 3]. To this list also other exotic phases can be added, such as exciton-polariton condensates in semiconductor microcavities [30]. Superfluidity has been even suggested recently as a mechanism to explain the problem of dark matter [31].

Superfluids

Following [4], we define superfluidity as a generalization of Bose-Einstein condensation: for a system to be superfluid, at any time t it must exist a single-particle wave function $\Psi_0(\mathbf{r}, t)$ which is occupied by a finite fraction of all the particles, while all the other single-particle states are occupied by a number of particles which is of the order of 1 or less. The wave function $\Psi_0(\mathbf{r}, t)$ is called the wave function of the condensate, and the N_0 particles occupying it are the condensate. The number N_0 is in general different from the total number of particles N , even at zero temperature. In dilute atomic BECs the difference $N - N_0$, called quantum depletion, is of the order of 1%, while in liquid ^4He the number of particles in the condensate is of the order of only 10 % of the total number of particles. Other than with the wave function $\Psi_0(\mathbf{r}, t)$, the condensate can be described with its density $n(\mathbf{r}, t)$ and phase $S(\mathbf{r}, t)$, defined as

$$\Psi_0(\mathbf{r}, t) = \sqrt{n(\mathbf{r}, t)} e^{iS(\mathbf{r}, t)}. \quad (1.1)$$

The condensate density is therefore the modulus squared of the wave function $|\Psi_0(\mathbf{r}, t)|^2 = n(\mathbf{r}, t)$. A very useful description for a superfluid is given in terms of two-fluid hydrodynamics. In this picture, the total momentum density of the fluid is written as the sum of two components

$$\mathbf{j} = \rho_s \mathbf{v}_s + \rho_n \mathbf{v}_n, \quad (1.2)$$

where the first is called the superfluid component and the second the normal component. The superfluid component is of course associated with the condensate, while the normal component is associated with the excitations and it is the one responsible for the presence of dissipation. The superfluid velocity \mathbf{v}_s is linked to the condensate wave function through the relation

$$\mathbf{v}_s(\mathbf{r}, t) = \frac{\hbar}{m} \nabla S(\mathbf{r}, t). \quad (1.3)$$

The superfluid density ρ_s is not, in general, equal to the condensate density. In fact, for standard superfluids, ρ_s and ρ_n depend on temperature, with

$$\lim_{T \rightarrow 0} \rho_s(T) = \rho \quad \lim_{T \rightarrow 0} \rho_n(T) = 0, \quad (1.4)$$

where $\rho = \rho_s + \rho_n$ is the total density, while we have seen that the condensate density isn't the total one even at zero temperature. Over the critical temperature we have $\rho_n = \rho$ and $\rho_s = 0$. Despite the form of the current density (1.2), the two components don't correspond to two physically distinguishable species. For example, it can be shown that in a weakly interacting Bose gas the normal component ρ_n is identified with the density of the thermal atoms, i.e. the non-condensed ones, only near to the critical temperature [2]. Otherwise it has different forms which depend

on the collective excitations of the system.

With the two variables \mathbf{v}_s and ρ_s we can describe the dynamics of the superfluid at $T = 0$ (when $\rho = \rho_s$) with the hydrodynamic equations of a fluid with zero viscosity

$$\begin{cases} \frac{\partial \rho}{\partial t} + \nabla \cdot (\mathbf{v}_s \rho) = 0 \\ m \frac{\partial \mathbf{v}_s}{\partial t} + \nabla \left(\frac{m}{2} \mathbf{v}_s^2 + \mu(\rho) + V_{ext} \right) = 0. \end{cases} \quad (1.5)$$

The first equation is the continuity equation which expresses the conservation of mass. The second equation is the Euler equation for the flow of a non-viscous liquid, in an external potential V_{ext} . The relation $\mu(\rho)$, which gives the chemical potential μ in terms of the density ρ , is the equation of state of the system¹. The effect of the presence of the condensate is in the form of the velocity field, eq. (1.3), which means that it must satisfy

$$\nabla \wedge \mathbf{v}_s = 0. \quad (1.6)$$

The equations describing a superfluid at zero temperature are therefore in the form of classical irrotational hydrodynamics. The irrotationality condition (1.6) has profound consequences in the behavior of superfluids under rotations, as we will see in the next paragraph.

The Hess-Fairbank effect

The relationship between superfluid velocity \mathbf{v}_s and phase S of the condensate in eq. (1.3) means that the superfluid can't support any motion with vorticity different from zero. First, let us consider a region of space simply connected and completely occupied by the superfluid. Chosen a closed line in the region, we can calculate the circulation of the velocity field around the line using Stokes theorem:

$$\Gamma = \oint \mathbf{v}_s \cdot d\mathbf{l} = \int \nabla \wedge \mathbf{v}_s \cdot d\mathbf{S} = 0, \quad (1.7)$$

from eq. (1.6). The second integral is performed on a surface that lies on the line. The circulation of the velocity field around a closed line is always zero: clearly, this condition rules out all the classical rotational motions characterized by a velocity field of the type $\mathbf{v} = \boldsymbol{\omega} \wedge \mathbf{r}$, with $\boldsymbol{\omega}$ angular velocity, since in this case the circulation on a circle with radius R is $\Gamma = 2\pi\omega R^2$. The condition of zero circulation is at the heart of the Hess-Fairbank effect, a phenomenon which happens if we put a superfluid in a cylindrical container and we rotate the container with angular velocity $\boldsymbol{\omega}$. We are interested in the state of thermodynamic equilibrium. For simplicity, we consider an annulus of radius R , although all the following considerations apply equally in a full disk. In the laboratory frame, the potential between the atoms and the container depends on time, so that it is convenient to move in the frame rotating

¹In chapter 2 the hydrodynamic equations are explicitly derived in the case of a dilute system of ultracold bosonic atoms, in the context of the Gross-Pitaevski equation.

with the container. In this frame, the state of thermodynamic equilibrium is found minimizing the effective free energy

$$F_{eff} = F_{lab} - \boldsymbol{\omega} \cdot \mathbf{L}, \quad (1.8)$$

where \mathbf{L} is the angular momentum in the laboratory frame. For temperatures larger than the critical temperature, when the system is completely normal (i.e. $\rho_s = 0$), the state of thermodynamic equilibrium is the one for which $v_n = \omega R$, with an angular momentum $L = Nm\omega R^2$ along the z axes. We can calculate the moment of inertia through the definition

$$\Theta = \frac{L}{\omega}, \quad (1.9)$$

which results in the classical value, i.e. $\Theta_c = NmR^2$. When we cool down under the critical temperature, a fraction ρ_s of the superfluid is described by the velocity field \mathbf{v}_s , bounded by the circulation condition (1.7). The superfluid can't perform a rigid rotation as the normal component, so that a fraction ρ_s/ρ of the liquid decouples from the rotation, transferring its angular momentum to the container. The resulting angular momentum of the liquid is $L = (1 - \rho_s/\rho)NmR^2\omega$, and thus the moment of inertia below the critical temperature is

$$\Theta = (1 - f_s)\Theta_c, \quad (1.10)$$

where f_s is called superfluid fraction and in the two-fluid model it corresponds to ρ_s/ρ . This phenomenon was first observed by Hess and Fairbank, who measured the increase in angular momentum of the container while lowering the temperature of a sample of liquid helium [32]. They deduced that under a critical angular velocity the angular momentum of the liquid was indeed zero, while the walls of the container were rotating. We discuss which is the expression for this critical velocity and what happens above it in the next paragraph.

Vortices

We have seen in eq. (1.7) that the circulation of the superfluid velocity must be zero, but this is not true in general. To obtain that result, we have applied Stokes theorem, but we can do it only in a simply connected space. If the velocity isn't defined in some regions of the space, we can't make that passage and we can't conclude that the circulation is zero. A general result can, however, be obtained using the fact that the wave function must be single-valued so that the phase can change only by integer multiples of 2π along a closed path. Using the relation velocity-phase in eq. (1.3), we obtain the result

$$\Gamma = \oint \mathbf{v}_s \cdot d\mathbf{l} = n \frac{h}{m}, \quad (1.11)$$

where n is an integer. Eq. (1.11) is also known as Onsager-Feynman quantization formula, since it states that the velocity circulation is quantized in multiples of h/m . In an annulus of radius R as the one considered in the previous paragraph, the velocity field is of the form

$$v_s = n\omega_c R \quad (1.12)$$

where $\omega_c = \hbar/mR^2$. If the circulation Γ acquires a finite value corresponding to $n = 1$ the system is said to possess a vortex line. When does the equilibrium configuration of the superfluid contain a vortex line? Intuitively, this happens when the initial angular velocity of the container is large enough. Calculating the free energy with the velocity $v_n = \omega R$ for the normal part and $v_s = n\omega_c R$ for the superfluid part one obtains that it is minimized if n is the closest integer to ω/ω_c . When $\omega/\omega_c < 1/2$, the closest integer is zero, so no vortex forms and we recover the Hess-Fairbank effect. For larger angular velocity, the angular momentum of the equilibrium configuration increases in steps proportional to \hbar , through the formation of states in which, at $T = 0$, each atom has an angular momentum of $n\hbar$, for a total angular momentum of $nN\hbar$. In the more experimentally relevant case of simply connected space, such as a full disk, the vortex line is a region of space in which the superfluid density vanishes, so that the phase of the wave function, and then the superfluid velocity, aren't defined. Extending the solution (1.12) for the annulus to the whole disk, we obtain a velocity field which is inversely proportional to r , the distance from the center. Such a field is indeed irrotational and would diverge on the axis of the container, but in that point the vortex line forms and the wave function vanishes. For higher angular velocities, it is found that vortices with multiple quanta of circulation are unstable with respect to decay into vortices with a single quantum. The state with the lowest energy, therefore, contains many vortices, which repel each other with a mechanism exactly analog to the Magnus force of classical hydrodynamics [33]. The result is the formation of a triangular array of vortices (see Fig. 1.1 E and Fig. 1.2), also called Abrikosov lattice². For an experimental study of the vortex lattice in a BEC, see [34].

Finally, we note that the rotational effects described so far are conceptually different from the best known phenomenon called metastability of supercurrents. In that case, the previous thought experiments are modified: above the critical temperature the container is rotated with $\omega \gg \omega_c$ and the system is waited to be in equilibrium with it; then the temperature is lowered below the critical temperature and the container is stopped. Although a normal liquid rapidly stops rotating, occupying the new equilibrium state, which is, of course, the one in which it is at rest, a superfluid will persist in the metastable rotating configuration for astonishing long times (to give a number, for superconductors a lower limit of 10^{15} years exists for the relaxation time of the supercurrent [1]).

Evidences of superfluidity from rotation in different systems

As explained in the previous paragraphs, superfluids show clearly a different behavior compared to a classical system when put under rotation. Historically, proofs of superfluidity for a number of different systems have been obtained through the study of rotations. In Fig. 1.1 some images from papers in different fields and different

²Some scientists in the field, as S. Stringari, suggest that the vortex lattice could be thought as a supersolid: it is a superfluid system which breaks the translational invariance through the formation of "holes" in the density, instead of peaks. It would be a supersolid in a state of high angular momentum. However, the issue is not clear, and, at the moment, there are neither experimental nor theoretical studies on the subject.

years are shown. The first system to be studied was, of course, liquid ^4He : the first experiment has been the one from Hess and Fairbank [32], discussed in the previous paragraph (see Fig. 1.1 A). The fermionic isotope of helium, ^3He , has been demonstrated to show superfluidity under 2.5 mK, through the formation of Cooper pairs similarly to superconductors [1](Fig. 1.1 B). Differently from the standard BCS theory, however, ^3He Cooper pairs possess non-trivial internal quantum numbers, since they form in states with non-zero orbital angular momentum and spin. As a consequence, the phenomenology in ^3He is particularly rich: two superfluid states exist, $^3\text{He-A}$ and $^3\text{He-B}$, and vortices can appear in several different forms [35]. In the ultracold regime of quantum gases, superfluidity has been demonstrated, in the context of rotations, through the appearance of quantized vortices. In [36], the angular momentum of the condensate was extracted through the measurement of the frequencies of two collective quadrupole mode (Fig. 1.1 D). Another successful probe for the test of superfluidity in quantum gases has been the scissors mode [25], to which we dedicate the last section of this chapter. Vortices have been studied also in degenerate Fermi gases, across the crossover which brings from standard Bose-Einstein condensate to a superfluid of Cooper pairs in the BCS side, changing the interaction parameter [37] (Fig. 1.1 E). Vortices have been observed also in an exciton-polariton condensate in a semiconductor microcavity [30] (Fig. 1.1 C).

Finally, we comment on the relationship between the physics of rotations in superfluids discussed so far and superconductors, following [1]. The analogy with a superconductor is obtained by substituting the rotational field with a magnetic field. Formally, it can be shown that the Hamiltonian \mathcal{H}' of a rotating neutral system, in the rotating frame, is equivalent to the Hamiltonian \mathcal{H} of a charged system in a static magnetic field, in the laboratory frame, with the substitution $m\boldsymbol{\omega} \wedge \mathbf{r} \leftrightarrow e\mathbf{A}(\mathbf{r})$:

$$\mathcal{H}' = \frac{(\mathbf{p} - m\boldsymbol{\omega} \wedge \mathbf{r})^2}{2m} + V_{ext}(\mathbf{r}) - \frac{1}{2}m(\boldsymbol{\omega} \wedge \mathbf{r})^2 \quad \leftrightarrow \quad \mathcal{H} = \frac{(\mathbf{p} - e\mathbf{A}(\mathbf{r}))^2}{2m} + V_{ext}(\mathbf{r}) \quad (1.13)$$

apart from the centrifugal term in the neutral case. The applied magnetic field is $\mathbf{B} = \nabla \wedge \mathbf{A}$. The analog of the Hess-Fairbank effect in a charged system is the Meissner effect: a superconductor expels from its bulk a static magnetic field, provided it is lower than a critical value B_{c1} , behaving like a perfect diamagnet. More precisely, the magnetic field $\mathbf{B}(\mathbf{r})$ and the vector potential $\mathbf{A}(\mathbf{r})$ decay exponentially inside the superconductor with a typical length scale called the London penetration depth

$$\lambda_L(T) = \sqrt{\frac{m^2}{\mu_0 e^2 \rho_s(T)}} \quad (1.14)$$

where $\rho_s(T)$ is the superfluid density, with the same meaning of the neutral case. The critical value B_{c1} for the magnetic field is the analog of the critical angular velocity ω_c in the neutral case. The counterpart to the vortex state of the neutral system also exists. In the latter, a vortex forms when the velocity exceeds the critical value ω_c , and the angular momentum of the superfluid is quantized in units of \hbar . In the superconductor, when the magnetic field overcomes the critical value B_{c1} a finite magnetic flux $\Phi = \oint \mathbf{A} \cdot d\mathbf{l}$ is allowed to enter in the system, through the appearance

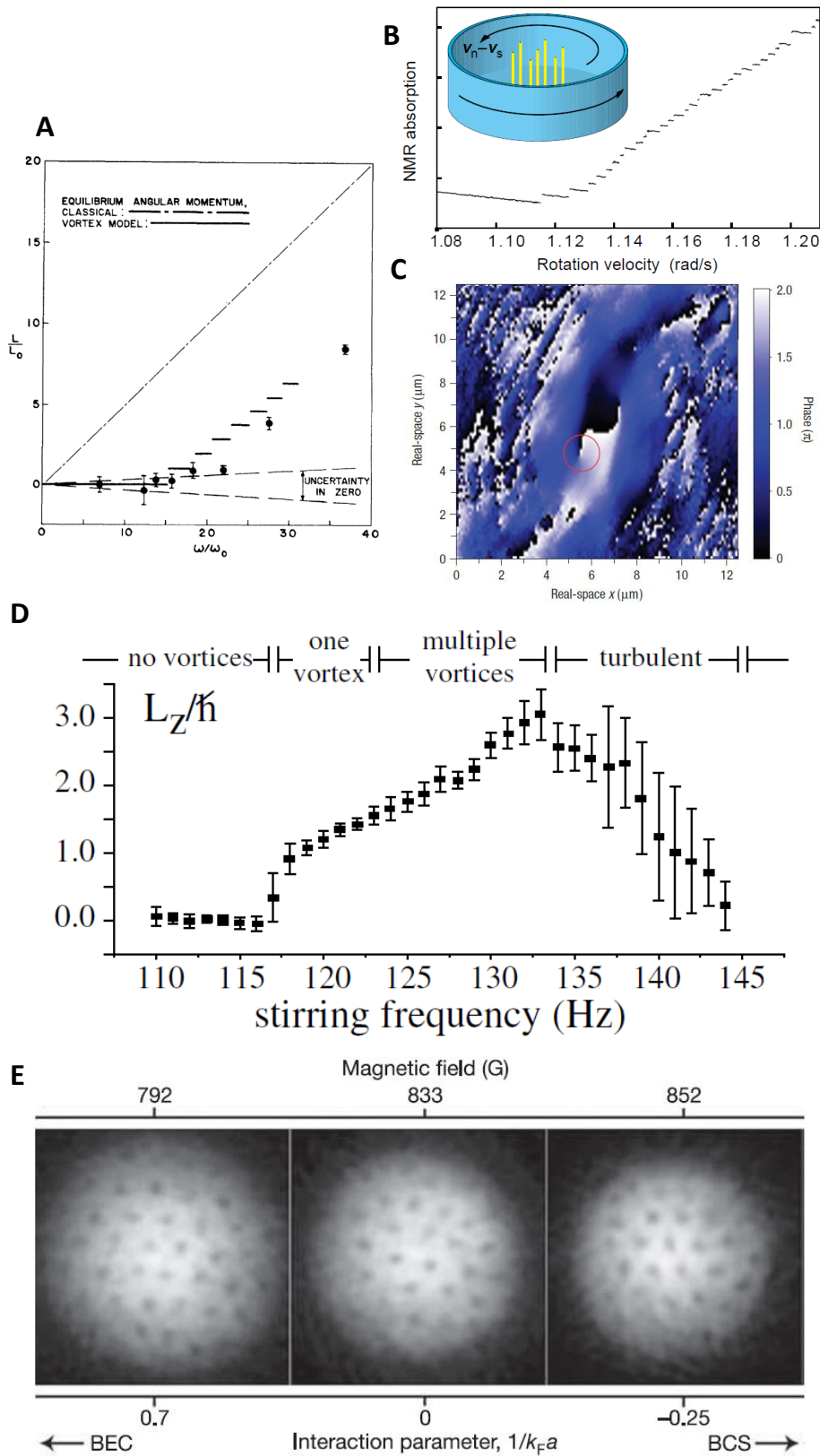


Figure 1.1: Evidence of superfluidity from rotation in several different systems. (A) The Hess-Fairbank effect in liquid ^4He [32]. (B) Vortices in ^3He [35]. (C) Phase diagram with a vortex in an exciton-polariton condensate [30]. (D) Non-classical angular momentum in an atomic Bose-Einstein condensate [36]. (E) Vortices across the BEC-BCS crossover in a degenerate Fermi gas [37].

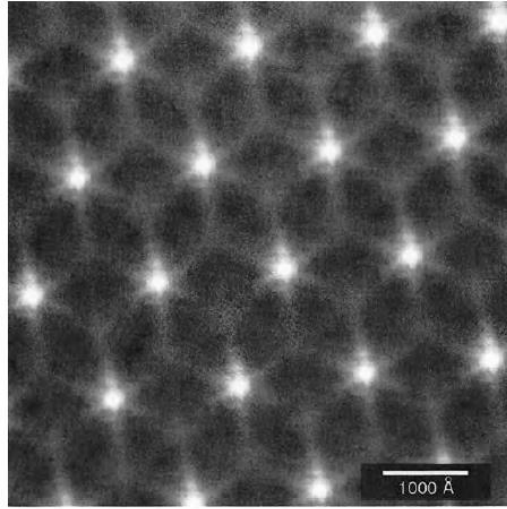


Figure 1.2: Vortex array in a type-II superconductor (NbSe_2), imaged with a scanning tunneling microscope. The vortex cores are the bright regions, while the superconducting regions are the dark ones. Image taken from [38].

of a region in which the wave function vanishes, i.e the metal becomes normal. Such a region is the vortex line in the superconductor phase, around which the magnetic flux is quantized in units of the flux quantum $\Phi_0 = h/2m$, i.e. $\Phi = n\Phi_0$. The core of the vortex is of the order of the Cooper pair radius ξ . Increasing further the magnetic field produces an array of vortices, as in the neutral case (see Fig. 1.2). Over an upper critical field B_{c2} the vortices overlap one with the other and the metal becomes completely normal. Actually, the previous behavior describes only a fraction of the known superconductors, the so-called type-II superconductors, for which the condition $\lambda_L/\xi \gg 1$ holds. In the other limit, the system is called type-I superconductor and doesn't possess the vortex state, although it still shows the Meissner effect.

1.2 Leggett's argument: can a solid be superfluid?

The most intuitive idea of a superfluid as something that can sustain a perfect frictionless flow seems incompatible with a crystalline order since the latter is typical of rigid bodies. However, quantum mechanics can mix the two opposite natures of a superfluid and a solid, as A.J. Leggett suggested in 1970 [9]. We focus on the paper by Leggett and not on the other seminal papers by Chester [8] and Andreev and Lifschitz [7], cited in the introduction, because Leggett proposed the supersolid exactly in the context of rotations, and his work is, therefore, the conceptually nearest to the experiment that we present in this thesis. In this section, we analyze in detail Leggett's argument, trying to understand what happens to an ideal supersolid under rotation. We aim to explain as simply as possible, step by step, the reasoning,

which may appear hard to grasp from the original papers, and sometimes even to elaborate some issues which could be interesting to study in future works.

Leggett generally defined the property of Non-Classical Rotational Inertia (NCRI) through the following thought experiment: N bosonic atoms with mass m are confined in a cylindrical annulus of radius R and thickness d (with $d \ll R$) that is rotated around the axis passing from the center of the annulus with velocity ω . The free energy of the system in the rest frame is assumed to be

$$F(\omega) = F_0 + \Theta_c \omega^2 / 2 + \delta F(\omega), \quad (1.15)$$

where the first two terms are the classical result for a rigid body rotating with the container, and the last term is the departure of the actual free energy from the classical one. F_0 is the free energy in the absence of rotation and Θ_c the classical moment of inertia, i.e. $\Theta_c = NmR^2$ if we neglect terms of order d/R . The superfluid fraction f_S of the system is defined through the relation

$$\delta F(\omega) = -f_S \Theta_c \omega^2. \quad (1.16)$$

By mixing the two formulae (1.15) and (1.16) we see that the definition of the superfluid fraction can be recast in terms of the moment of inertia

$$\Theta = (1 - f_S) \Theta_c, \quad (1.17)$$

meaning that the superfluid part of the system doesn't contribute to the moment of inertia. In the context of standard superfluids, the formula (1.17) is nothing but the Hess-Fairbank effect. For a completely superfluid system, such as liquid helium II or atomic BEC, $f_S = 1$ at $T = 0$. These systems can be described with a superfluid fraction less than 1 when $T > 0$ and a thermal component appears, increasing the moment of inertia. More generally, every two-fluid model allows a description in terms of a superfluid fraction varying between zero and one, in the sense that a part of the system is superfluid, being described by a unique wavefunction, and another part not. An example of a two-fluid model that doesn't involve a thermal component is a Fermi gas: in this case, lowering the temperature, a portion of the system undergoes a superfluid transition via the formation of Cooper pairs, while the left portion is a degenerate Fermi gas. It is thus common, in the field of superfluidity, to talk about a superfluid fraction that varies with the temperature and such that $f_S(T = 0) = 1$. What Leggett pointed out in his 1970 article [9] (and later in [39]) is that it is possible to have $0 < f_S < 1$ at $T = 0$, the necessary condition for this strange behavior being the breaking of translational invariance of the ground state. In other words, Leggett predicted that a matter wave with phase coherence but modulated density distribution, i.e. the supersolid phase of matter, should show non-classical rotational inertia (NCRI) effects with a superfluid fraction less than one even at zero temperature, and not necessarily associated to a two-fluid picture.

To obtain an expression for the superfluid fraction, linking it to the density distribution, we need to solve the quantum mechanical problem of the rotating system. Given the hamiltonian of the system \mathcal{H} , to find the solution of the Shroedinger

equation $\mathcal{H}\Psi_0 = E_0\Psi_0$ one has to specify the boundary conditions to be fulfilled by the wave function Ψ_0 . First, for a system of identical bosons, Ψ_0 must be symmetric with respect to the interchange of two particles. Second, and crucial for the present problem, Ψ_0 must be single-valued with respect to the coordinate \mathbf{r}_i of any particle. In the annular geometry this condition is meaningful for the angular coordinates θ_i (we don't report the dependence on z_i and r_i), and it reads

$$\Psi_0(\theta_1, \dots, \theta_i + 2\pi, \dots, \theta_N) = \Psi_0(\theta_1, \dots, \theta_i, \dots, \theta_N) \quad \forall i = 1, \dots, N. \quad (1.18)$$

In other words, if we take a particle and move it in a circle to the initial position, the wave function can't change. When the confining walls rotate the potential is time dependent. It is therefore convenient to work in the frame rotating with the container, where the potential is time independent, given that the interaction between particles is only a function of positions and not of velocities. Using the canonical prescription to change coordinates in hamiltonian mechanics, with the substitution $\theta'_i = \theta_i - \omega t$, we find the hamiltonian in the rotating frame

$$\mathcal{H}'(\mathbf{r}', \mathbf{p}') = \mathcal{H}(\mathbf{r}', \mathbf{p}') - \boldsymbol{\omega} \cdot \mathbf{L}', \quad (1.19)$$

with $\mathbf{L}' = \mathbf{r}' \times \mathbf{p}'$ the angular momentum. This is not enough, since the wave function Ψ_0 doesn't satisfy the Schroedinger equation with the new hamiltonian. We thus need to multiply Ψ_0 for a phase factor, so that $\mathcal{H}'\Psi'_0 = E'_0\Psi'_0$. The relationship between the wave functions in the two reference frames is found to be

$$\Psi'_0(\theta'_1, \dots, \theta'_i, \dots, \theta'_N, t) = e^{-im\omega R^2/\hbar \sum_j \theta'_j} \Psi_0(\theta'_1 + \omega t, \dots, \theta'_i + \omega t, \dots, \theta'_N + \omega t). \quad (1.20)$$

We finally conclude that in the rotating frame the boundary condition (1.18) is modified into

$$\Psi'_0(\theta'_1, \dots, \theta'_i + 2\pi, \dots, \theta'_N) = e^{-i2\pi m\omega R^2/\hbar} \Psi'_0(\theta'_1, \dots, \theta'_i, \dots, \theta'_N) \quad \forall i = 1, \dots, N. \quad (1.21)$$

Because we neglect terms of order d/R , we can imagine to unroll the annulus and to work in a one-dimensional space, with the substitution $\theta'_i \rightarrow x_i$ for the coordinate of the i^{th} particle. The variable x_i varies between 0 and $2\pi R$. The next step is to search for a solution of the stationary Schroedinger equation in the rotating frame via a variational approach. We make the ansatz

$$\Psi'_0(x_1, \dots, x_i, \dots, x_N) = e^{i\sum_j \phi(x_j)} \psi_0(x_1, \dots, x_i, \dots, x_N) \quad (1.22)$$

where ψ_0 can be taken real, and, to satisfy the boundary condition (1.21), we ask

$$\phi(x + 2\pi R) = \phi(x) - 2\pi m\omega R^2/\hbar. \quad (1.23)$$

The expectation value of the hamiltonian of the system on the ansatz (1.22) results

$$\langle H \rangle_{var} = E_0 + \frac{\hbar^2}{2m} \sum_j \int \left(\frac{d}{dx_j} \phi(x_j) \right)^2 \rho(x_j) dx_j, \quad (1.24)$$

where we have introduced the density distribution of the particles j defined as $\rho(x_j) = \int (\psi_0(x_1, \dots, x_N))^2 dx_1 \dots dx_{j-1} dx_{j+1} \dots dx_N$. The energy of the system at rest is E_0 . We note that the only term appearing due to the rotation is a sum of identical kinetic energy terms. The goal of the variational approach is to minimize such a term, given the density distribution $\rho(x)$. The variational parameter is the phase function $\phi(x)$, that can be determined using the standard variational calculus. Indeed, the terms in eq. (1.24) are in the form of the well known classical action $S = \int \mathcal{L}(q(t), \dot{q}(t)) dt$, for which the procedure of minimization on all the possible paths $q(t)$ leads to the Euler-Lagrange equation $\frac{d}{dt} \left(\frac{\partial}{\partial \dot{q}} \mathcal{L} \right) - \frac{\partial}{\partial q} \mathcal{L} = 0$. To make the correspondence evident, we substitute $q(t) \rightarrow \phi(x)$ and $\dot{q}(t) \rightarrow \frac{d}{dx} \phi(x)$, so that the integrand in eq. (1.24) is a lagrangian $\mathcal{L} \left(\phi(x), \frac{d}{dx} \phi(x) \right) = \left(\frac{d}{dx} \phi(x) \right)^2 \rho(x)$, from which we derive the Euler-Lagrange equation

$$\frac{d}{dx} \left(\frac{d}{dx} \phi(x) \rho(x) \right) = 0, \quad (1.25)$$

satisfied by the function $\phi(x)$ that minimizes the energy (1.24). Solving eq. (1.25) we obtain the solution

$$\phi(x) = \int_0^x \frac{c}{\rho(x')} dx' \quad (1.26)$$

where c is a constant to be determined imposing the boundary condition (1.21). The result is

$$\phi(x) = \frac{-mR\omega}{\hbar} k \int_0^x \frac{1}{\rho(x')} dx', \quad (1.27)$$

where $k = \left(\frac{1}{\lambda} \int_0^\lambda \frac{dx'}{\rho(x')} \right)^{-1}$ and λ is the dimension of the unit cell of the supersolid. The main feature of eq. (1.27) is that the phase of the rotating system depends on the form of the density distribution: for a uniform density one obtains a linear function of x , i.e. $\phi_{unif} = -\frac{mR\omega}{\hbar} x$, while for a supersolid the phase increases more rapidly near a density maximum, as depicted in Fig. 1.3.

Substituting the phase $\phi(x)$ of eq. (1.27) in the variational energy (1.24) we obtain

$$\langle H_{var} \rangle = E_0 + \frac{1}{2} NmR^2 \omega^2 \left(\frac{1}{\lambda} \int_0^\lambda \frac{dx'}{\rho(x')/\bar{\rho}} \right)^{-1}, \quad (1.28)$$

where we have defined the mean density $\bar{\rho} = N/2\pi R$.

Given the phase, it is straightforward to calculate the velocity field, since $v(x) = \frac{\hbar}{m} \frac{d}{dx} \phi(x)$, so that the velocity is proportional to the inverse of the density

$$v(x) = -\omega R \frac{k}{\rho(x)}. \quad (1.29)$$

For a uniform superfluid the velocity is constant and equal to $-\omega R$. This result is valid in the rotating frame; in general, for our one-dimensional system, the velocity in the lab frame is obtained by a Galileian transformation of eq. (1.29) $v_{lab} = \omega R + v$,

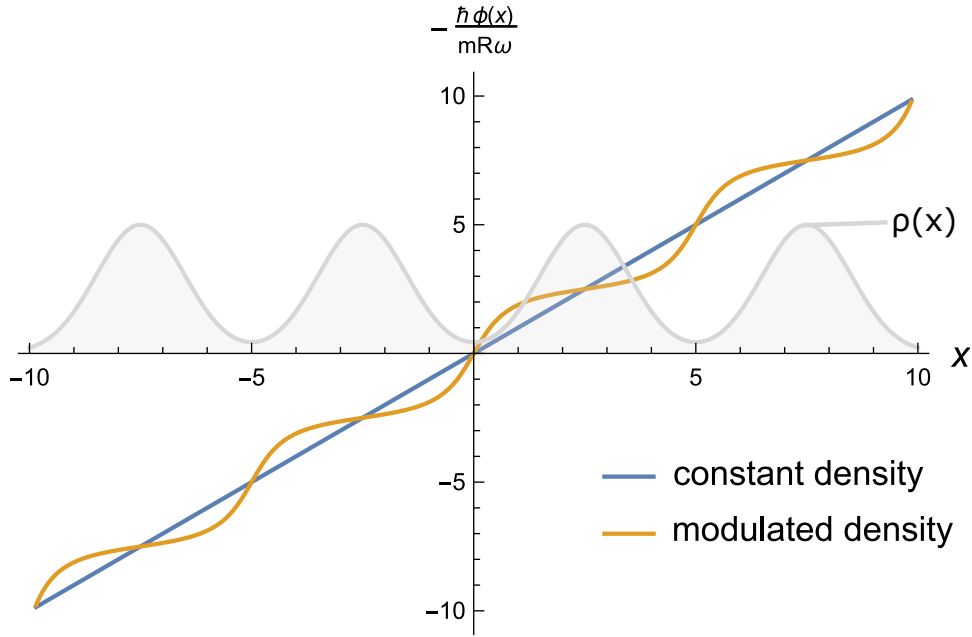


Figure 1.3: The phase of a system with uniform density, in yellow, and with modulated density, in blue, from eq. (1.27). The modulated density $\rho(x)$ is plotted in gray for comparison, not in scale. The boundary condition (1.23) fixes the values of ϕ at the boundaries. For a supersolid, it is energetically more favorable to increase the phase more rapidly where ρ is smaller and more slowly where ρ is larger.

so that in the laboratory frame the superfluid doesn't move, and we find the known result that the superfluid's moment of inertia is equal to zero. On the other hand, for a supersolid the velocity field results

$$v_{lab}(x) = \omega R \left(1 - \frac{k}{\rho(x)}\right). \quad (1.30)$$

This function is plotted in Fig. 1.4. We see that the atoms in a supersolid don't stay still, but move with different velocities: the density maxima follow the rotation of the container, tending to behave classically, while the density minima oppose to the rotation moving in the opposite direction, so that the single-valuedness boundary condition (1.18) is satisfied. In fact

$$\int_0^{2\pi R} v(x) dx = \frac{m}{\hbar} (\phi(2\pi R) - \phi(0)) = 0, \quad (1.31)$$

as can be verified using eq. (1.29).

We expect that the quasi-classical rotation of the density maxima is responsible for the increase of the moment of inertia, and the relative decrease of the superfluid fraction. To calculate the moment of inertia we use the definition

$$\Theta = \frac{\langle L \rangle}{\omega} \quad (1.32)$$

with $L = mRv$ is the angular momentum along the axis of rotation and the operation $\langle \rangle$ means an average on the density distribution $\rho(x)$. From eq. (1.29) and using

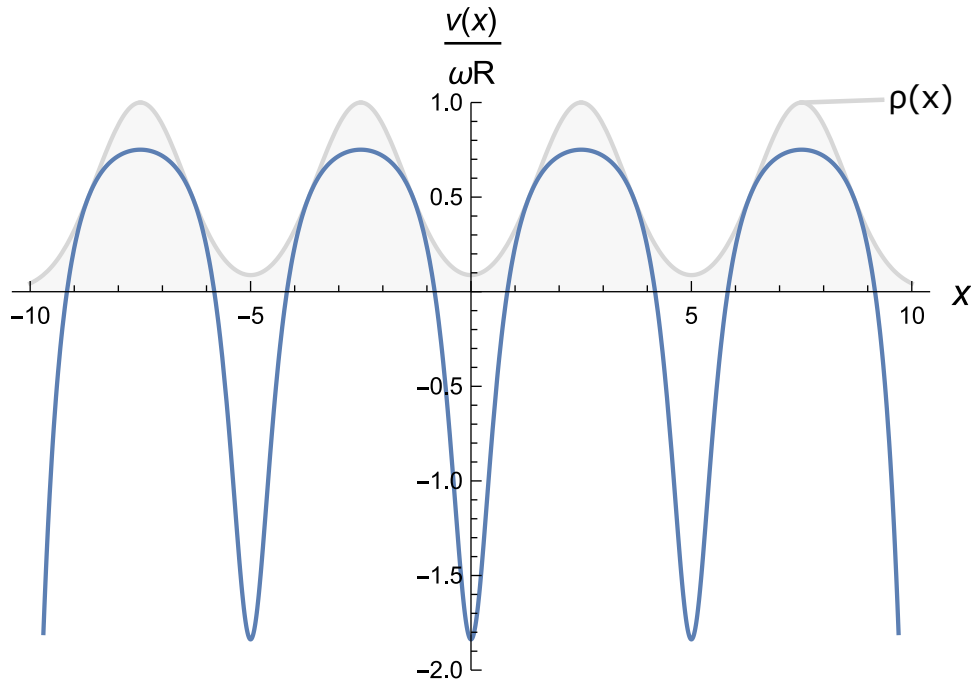


Figure 1.4: Velocity field in the laboratory frame for a system with modulated density, from eq.(1.30). The modulated density $\rho(x)$ is plotted in gray for comparison, not in scale. The density maxima start rotating quasi-classically, while the density minima move in the opposite direction so that the single-valuedness boundary condition (1.18) is satisfied.

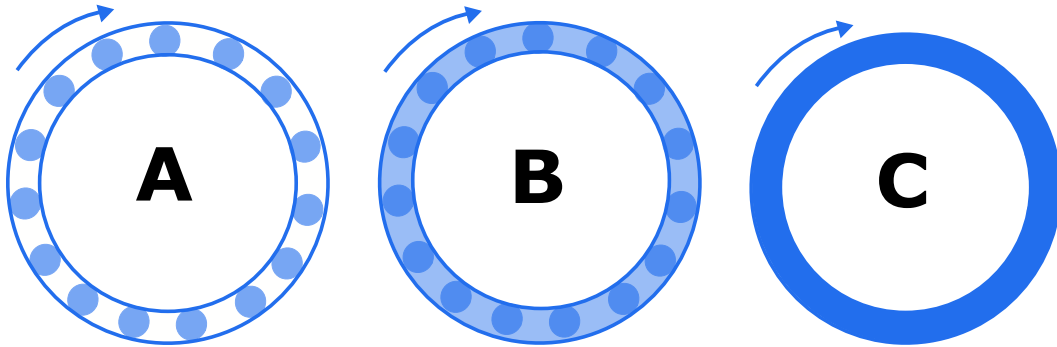


Figure 1.5: Intuitive explanation of the rotating properties in three different cases. (A) Normal crystal. Each density maximum is distinguishable from all the others so that it can be followed in a rotation. The moment of inertia is the classical one. (B) Supersolid. The density maxima are always visible, but they are linked by a superfluid background. Each atom is completely delocalized over the whole annulus, but the density modulation of the ground state allows detecting rotations. The moment of inertia is less than the classical one but different from zero. (C) Completely superfluid. The ground state has a constant density. Each atom is completely delocalized, with no preferable position. No rotation can be induced in this configuration, and the moment of inertia is zero.

the normalization condition $\int_0^{2\pi R} \rho(x) dx = N$ we obtain

$$\Theta = \frac{mR \langle v_{lab}(x) \rangle}{\omega} = mR^2(N - k2\pi R) = mR^2N(1 - Q_0), \quad (1.33)$$

where $Q_0 = \left(\frac{1}{\lambda} \int_0^\lambda \frac{dx'}{\rho(x')/\bar{\rho}} \right)^{-1}$. From the definition (1.17) of the superfluid fraction, we could conclude that $f_s = Q_0$. Actually, since we have employed a variational approach, we have obtained only an upper limit for the superfluid fraction [9]. The final result is

$$f_s \leq Q_0 = \left(\frac{1}{\lambda} \int_0^\lambda \frac{dx'}{\rho(x')/\bar{\rho}} \right)^{-1}. \quad (1.34)$$

To conclude, we propose an intuitive picture of the rotating properties in the three cases: crystal, supersolid, and superfluid, explained in Fig. (1.5).

1.3 The helium case

It is quite obvious that helium has been the first system to be seriously investigated looking for a supersolid phase. For many years superfluidity has been synonymous with helium, since no other superfluid systems were known. As a matter of fact, the first theoretical papers were about helium: the Andreev-Lifschitz mechanism, based on the delocalization of vacancies in an incommensurate crystal, is of course enhanced by the light mass of helium, which corresponds to a large zero-point motion.

The first claim of NCRI in solid helium was made in 2004, in two papers by Kim and Chan [10, 11]. Their experimental approach to supersolidity was very close to Leggett's idea: the supersolid was searched trying to detect an anomalous rotation while lowering the temperature. The experimental set-up was a torsional oscillator, in which a cylindrical cell containing solid helium in an annular channel was suspended on a torsion rod (see Fig. 1.6). At resonance, the period τ of the oscillator is given by

$$\tau = 2\pi \sqrt{\frac{\Theta}{K}}, \quad (1.35)$$

where Θ is the moment of inertia of the whole system and K is the torsional spring constant. The unexpected result they found was a drop in the oscillation period below about 0.1 K, consistent with the formation of a supersolid, whose superfluid component should have stopped participating the rotation, lowering therefore the total moment of inertia Θ in eq. (1.35). The authors found that the fraction of the mass that decoupled from the oscillation, which they called Non-Classical Rotational Inertia Fraction (NCRIF), was of the order of 0.01, as depicted in Fig. (1.6 (B)). Several control experiments were performed, to exclude non-supersolid explanations of the period drop. For example, the same experiment was repeated with a sample of ^3He , and also with ^4He with different concentrations of ^3He , showing that the period drop was observable only if the concentration of ^3He was under a certain

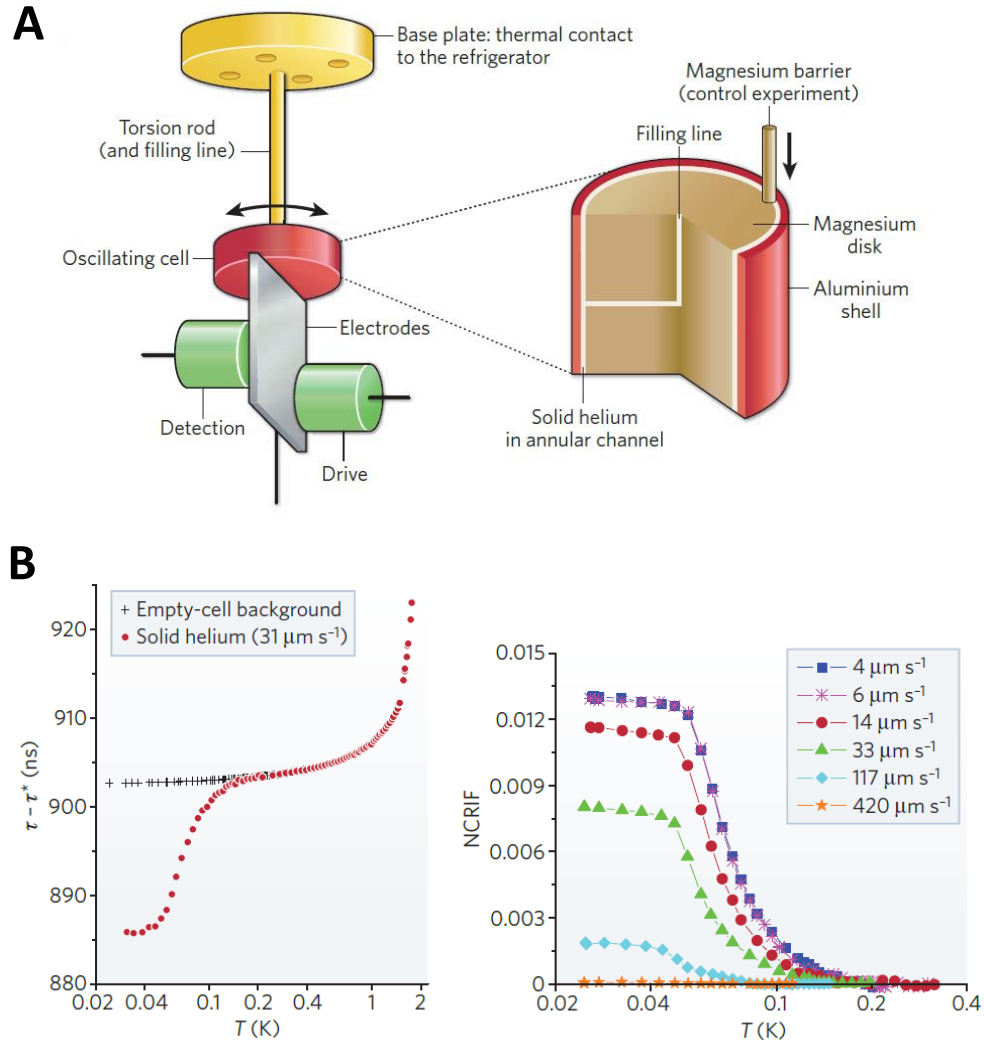


Figure 1.6: The torsional oscillator experiments by Kim and Chan [10, 11], taken from [12]. (A) The experimental apparatus is composed of a torsion rod and an oscillating cell. Helium is introduced in the cell through a filling line and then occupies an annular channel. Electrodes are used to drive and detect the oscillation of the cell. (B) Period drop at about 0.1 K, compared with the measurement effectuated with the empty cell when no drop is detected. τ^* is a reference period. On the right, Non-Classical Rotational Inertia Fraction (NCRIF), i.e. the fraction of the mass which decouples from the oscillation in the hypothesis of supersolidity. NCRIF is of the order of 0.01 and depends on the maximum velocity of the cell during the oscillation.

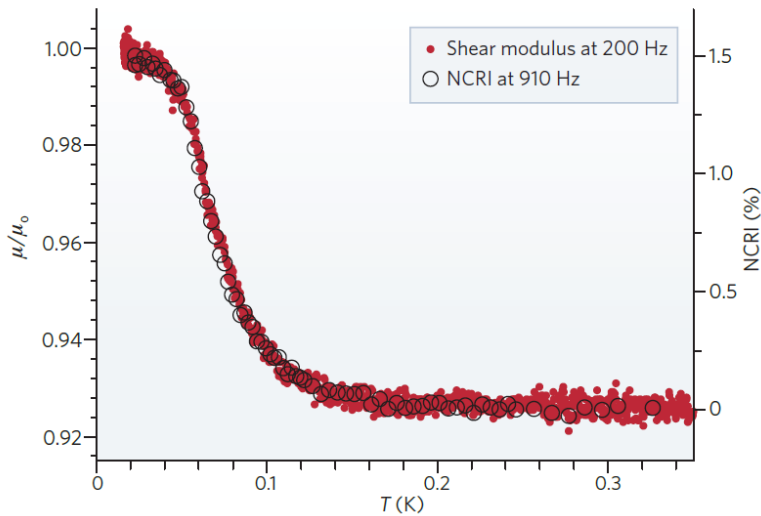


Figure 1.7: Comparison between shear modulus μ and NCRIF as a function of temperature from [12]. Open dots are shear modulus measurements normalized to its value at low temperatures μ_0 . Red dots are NCRIF measured with the torsional oscillator method. After adjustment of the vertical scales, the two sets of data coincide. The elastic anomaly and the rotation anomaly must have a common origin.

value, confirming that the phenomenon originated from the bosonic nature of the atoms.

A great effort, both theoretical and experimental, was made to understand the data and perform new experiments. For a review see [40]. In 2007 it was discovered that solid helium has unexpected elastic properties at low temperatures [41]. Its shear modulus, which measures the resistance to transverse forces, increases exactly in the range of temperatures in which the rotational signal was observed, suggesting that most of the experiments could be explained in terms of changes of the constant K , when the filling line containing helium passed also through the torsional rod, or in terms of a frequency-dependent moment of inertia, whose effects are different depending on the geometry of the cell. The change in shear modulus not only explained the temperature dependence of the observed signals (see Fig. 1.7), but also the dependence on ^3He impurity, with a model based on the displacement of dislocations. The original experiment by Kim and Chan was repeated with a new apparatus designed to minimize the effects of the shear modulus anomaly, and indeed no period drop was found [13].

1.4 Scissors mode and moment of inertia

We here focus on experiments performed on atomic Bose-Einstein condensates. As mentioned before, the rotational properties of a BEC have been investigated in [36], through the measurement of the angular momentum of the system with a

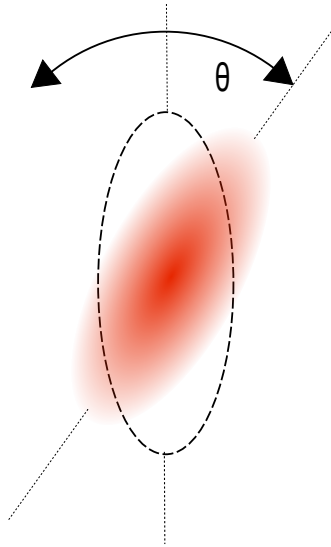


Figure 1.8: Sketch of a scissors oscillation. For small excitation angles θ , the scissors oscillation appears as a rigid rotation of the cloud around its equilibrium configuration.

method consisting of the observation of quadrupole modes frequencies. Here we discuss another method, which has been used to study the effects of superfluidity on rotations of BECs and is employed in this thesis to investigate the properties of the supersolid. In a theoretical paper [42], it was suggested that the moment of inertia of a trapped system can be extracted from the study of a peculiar mode, called the scissors mode, excited when the trap is rotated relative to a symmetry axis. A sketch of the mode dynamics is depicted in Fig. 1.8: the cloud oscillates around its equilibrium position, subject to the torque exerted by the trap, in evident analogy with the helium torsional oscillators. As in the helium case, the measurement of the oscillation frequency determines the moment of inertia. The scissors mode was known from nuclear physics, where it corresponds to an out-of-phase oscillation of the neutron and proton clouds which resembles the movement of the blades of a pair of scissors [43]. Experimental observations of the scissors mode provided a demonstration of superfluidity in ordinary BECs [25, 44]. Here we describe the oscillatory behavior of the scissors mode and its link to the moment of inertia.

Scissors oscillation

In the hydrodynamic formulation of the BEC's dynamics (see chapter 2), the excitation modes are obtained considering small density variations δn from the equilibrium value n_0 and linearizing the hydrodynamic equations around n_0 [2]. While the time variation is assumed to be of the form $\delta n \propto e^{-i\omega t}$, the spatial variation can have different forms depending on the trap geometry and the type of mode. Experiments with quantum gases are often performed with magnetic or optical traps, which can be described as a harmonic potential acting on the atoms, characterized

by the frequencies in the three directions $\omega_x, \omega_y, \omega_z$. The scissors mode appears in an anisotropic trap, whose anisotropy in the xy plane is defined as

$$\alpha = \left| \frac{\omega_y^2 - \omega_x^2}{\omega_y^2 + \omega_x^2} \right|. \quad (1.36)$$

The scissors mode has a two-dimensional nature, and corresponds to a density variation of the form $\delta n \propto xy$. Inserting this ansatz in the linearized hydrodynamic equations one finds that they are satisfied with a frequency

$$\omega_{sc} = \sqrt{\omega_x^2 + \omega_y^2}. \quad (1.37)$$

The scissors mode is excited rotating the trap around the z axis of a small angle θ . Indeed, starting from the equilibrium distribution in a trap and making the small-angle approximation $x \rightarrow x - \theta y$, $y \rightarrow y + \theta x$, the density variation induced by the excitation is

$$\delta n \propto \omega_{sc}^2 \alpha \theta xy, \quad (1.38)$$

and is therefore in the form of a scissors oscillation. Once that the trap is restored in the initial position, the cloud starts rotating around the trap axis. The time evolution of the angle θ is a simple sinusoidal oscillation at the scissors frequency

$$\theta(t) = \theta_0 \cos(\omega_{sc} t). \quad (1.39)$$

The validity condition of the previous equation is that $\theta_0 \ll \alpha$. A large anisotropy α , therefore, favors the scissors oscillations. If the angle is too large, the deformation gets a quadrupole character and the simple scissors geometry is lost.

As described previously, one of the peculiarities of superfluids is that, under a certain critical velocity, they can't acquire any angular momentum from a rotating cylindrical trap. This property derives from the condition of irrotationality which their velocity fields are forced to fulfill, and is often stated saying that a superfluid has zero moment of inertia at $T = 0$. The question is, therefore, how a scissors oscillation can be allowed despite the irrotationality condition. The atoms don't perform a rigid rotation around the z axis, with a velocity field of the type $\mathbf{v} \propto (-y, x, 0)$, but, solving the hydrodynamic equations for the scissors mode excited rotating the trap with angular velocity ω one finds

$$\mathbf{v} = \omega \beta (y, x, 0), \quad (1.40)$$

with the parameter β which quantifies the deformation of the cloud:

$$\beta = \frac{\langle y^2 - x^2 \rangle}{\langle x^2 + y^2 \rangle}. \quad (1.41)$$

The operation $\langle \rangle$ is an average on the density distribution. The velocity (1.40) satisfies the condition $\nabla \wedge \mathbf{v} = 0$, although in the limit of small excitations the global motion corresponds to an oscillation in the xy plane (see Fig. 1.8). The difference between a rotational field and the scissors field is depicted in Fig. 1.9. In the case

of non-dipolar BECs, the deformation of the cloud and that of the trap are equal, i.e. $\alpha = \beta$. On the other side, in dipolar gases the two parameters are different (see chapter 5).

Given the velocity field in the cloud (1.40) it is easy to calculate the angular momentum around the z axis and then the moment of inertia via the definition $\Theta = \langle L \rangle / \omega$. The result is that the parameter β enters two times, one from the modulus of the velocity, and one from its peculiar shape in the xy plane, so that the moment of inertia is proportional to β^2 :

$$\Theta = \beta^2 \Theta_c, \quad (1.42)$$

with $\Theta_c = mN \langle x^2 + y^2 \rangle$ being the classical moment of inertia of a rigid body consisting of N particles with mass m rotating around the z axis. We see, therefore, that in an anisotropic trap, the moment of inertia of a completely superfluid system, such as the BEC, is different from zero but lower than the classical value. In a trap with cylindrical symmetry, we recover the correct result of zero moment of inertia. In this case, the scissors oscillation is forbidden, and the velocity field (1.40) is identically zero. The need for anisotropy can be understood in terms of angular momentum conservation: during the scissors oscillation, the angular momentum isn't conserved, because the trap must exert a torque on the cloud to maintain the oscillation. Formally, this fact is embodied in the commutation relation between the hamiltonian and the angular momentum operator

$$[\mathcal{H}, J_z] = -im(\omega_y^2 - \omega_x^2)xy, \quad (1.43)$$

where m is the mass of the atoms. This commutation relation highlights the connection between the rotation of the cloud and the quadrupole operator xy , which is evident also in the form of the density perturbation, eq. (1.38).

In the classical regime of high temperatures, the same type of excitation is treated in the framework of the Boltzmann kinetic equations [42]. The behavior of the thermal cloud is determined by the collision rate between the atoms. If we call τ the typical time between two collisions, two different regimes exist depending on the value of $\alpha\omega_{sc}\tau$. In the collisionless regime, corresponding to $\alpha\omega_{sc}\tau \ll 1$, the oscillation of the thermal cloud is characterized by two frequencies, given by $|\omega_x \pm \omega_y|$. In the hydrodynamic regime, with $\alpha\omega_{sc}\tau \gg 1$, the low-lying solution becomes overdamped and the oscillation happens at a single frequency, given by ω_{sc} . For the dilute samples in the quantum gases laboratories, very often the regime of operation is the collisionless one so that the behavior of the condensate and the thermal gas is very different. The scissors mode, therefore, offers the possibility of a direct experimental demonstration of the superfluidity of a system.

As previously explained, the scissors dynamics is intrinsically linked to the quadrupole moment. This link leads to a useful and general relation between the system response to a scissors excitation and its moment of inertia, holding for classical as well as quantum systems [42]:

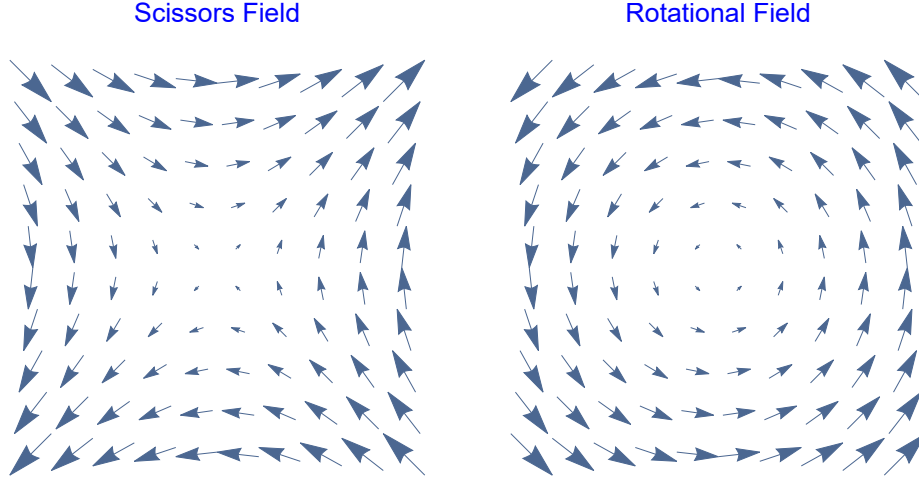


Figure 1.9: Comparison between the scissors and a rotational velocity field. The latter has the form $\mathbf{v} \propto (-y, x, 0)$ and has a non-zero vorticity. The first has the form $\mathbf{v} \propto (y, x, 0)$ and it is irrotational. In a superfluid, only the scissors field is allowed. For small enough excitation angles, the scissors oscillation resembles exactly a rigid oscillation of the whole cloud around the z axis.

$$\Theta = \Theta_c \left| \omega_y^2 - \omega_x^2 \right|_{\beta_{t=0}} \frac{\int F(\omega)/\omega}{\int F(\omega)\omega}. \quad (1.44)$$

The function $F(\omega)$ is the Fourier transform of the quadrupole operator $xy(t)$, and is therefore a measurable quantity. When the oscillation happens at a single frequency ω_{sc} (as in the BEC), so that $F(\omega) \propto \delta(\omega - \omega_{sc})$, from (1.44) we obtain the equation

$$\Theta = \Theta_c \alpha \beta_{t=0} \frac{(\omega_y^2 + \omega_x^2)}{\omega_{sc}^2}. \quad (1.45)$$

Using the hydrodynamic value of the scissors frequency given in eq. (1.37) and the fact that $\alpha = \beta$, we recover the result $\Theta = \beta^2 \Theta_c$ for the non-dipolar BEC. For a thermal cloud, the two-frequencies oscillation gives $\Theta = \Theta_c$: it is the presence of the low-lying frequency in the thermal gas which causes the moment of inertia to assume the classical value. Equation (1.45) can be used to experimentally determine the moment of inertia, through a measurement of the scissors frequency ω_{sc} .

The scissors mode has been experimentally studied in a series of papers from the group of C. Foot [25, 44], with a Bose-Einstein condensate of Rubidium atoms held in a magnetic trap. The mode is excited with a sudden tilt of the magnetic field producing the trap, which causes the BEC to be in an out-of-equilibrium configuration. The oscillations of the angle of the cloud as a function of time are shown in Fig. (1.10), both for a thermal cloud and the condensate. The single-frequency oscillation of the condensate, in agreement with the hydrodynamic result (1.37), demonstrates its irrotational velocity and hence its superfluid nature. A measurement of the scissors frequencies as a function of the temperature is instead reported in Fig. (1.11). Although the BEC oscillates at a single frequency for every temper-

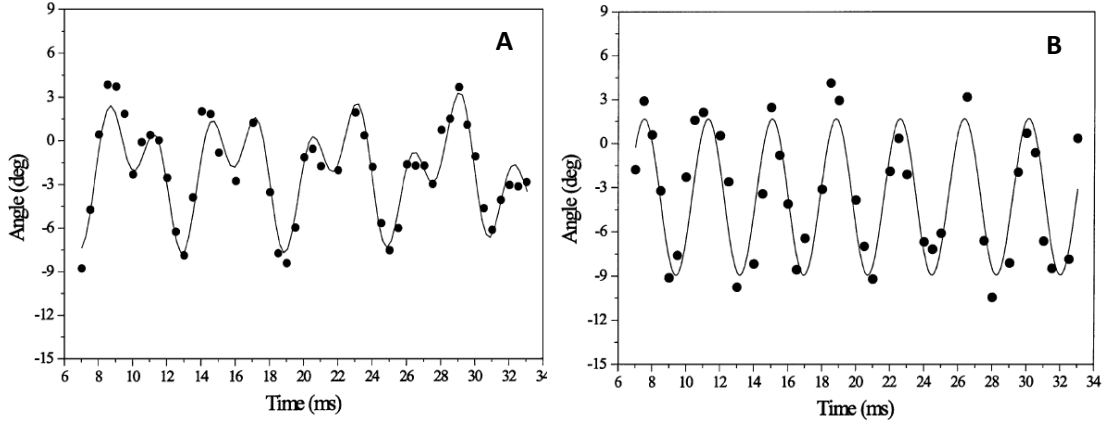


Figure 1.10: Scissors oscillation for a trapped BEC and a thermal cloud from [25]. A BEC of Rubidium atoms is trapped in a magnetic trap. The scissors mode is excited by tilting a symmetry axis of the trap, and the angle of the cloud is obtained through absorption imaging after time of flight. (A) Oscillation of the thermal gas, which shows two frequencies. (B) Single-frequency oscillation of the BEC, in agreement with the result of eq. (1.37), which is a proof of the superfluid nature of the condensate.

ature, the frequency gradually lowers with increasing temperature, a phenomenon which can be understood in terms of the interaction between the condensate and the thermal component. At higher temperatures, the thermal cloud oscillates with the two expected frequencies. From the formula (1.45) it is possible to derive the moment of inertia of both the condensate and the thermal cloud as a function of temperature (see Fig. 1.11 (B)). At low temperatures, the moment of inertia of the condensate is in good agreement with the value $\beta^2\Theta_c$, while at higher temperatures it increases, reflecting the decrease of the scissors frequency. On the other hand, the thermal cloud's moment of inertia is consistent with the classical value Θ_c for all the temperatures. For intermediate temperatures, when both the condensate and the thermal cloud are present, a semi-classical model allows extracting the moment of inertia of the whole system from the measurement of the different oscillations of the BEC and the thermal gas [45]. The result is shown as a continuous line in Fig. 1.11 (B), and it is a proof of the temperature-dependence of the moment of inertia of a quantum gas, which arises from a two-fluid picture: one classical fluid which contributes classically to the rotation, and one superfluid which lowers the total inertia of the system.

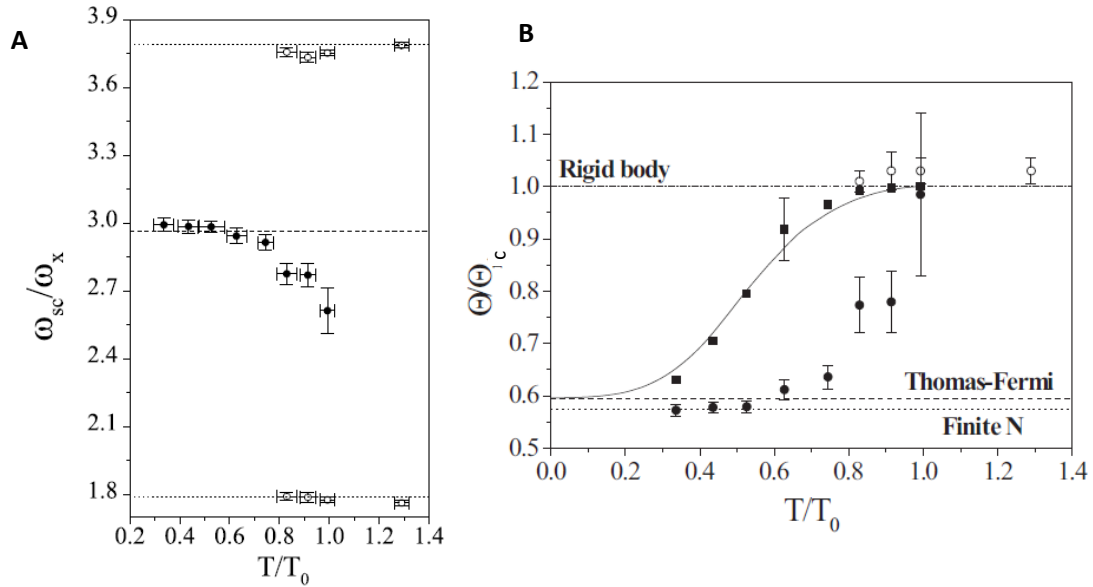


Figure 1.11: Scissors frequencies and moment of inertia as a function of temperature from [44, 45]. (A) Scissors frequencies of the BEC (black dots) are in agreement with the hydrodynamic prediction for low temperatures when the thermal component is absent. For higher temperatures, the frequency decreases, as a consequence of the interaction with the thermal component. Open dots are the results of the thermal gas. (B) Moment of inertia obtained from the scissors measurements. At low temperatures, the BEC (black circles) is in good agreement with the expected value $\beta^2\Theta_c$ (dashed line). A better agreement is reached inserting a correction accounting for the finite atom number (lower dotted line). At higher temperatures the moment of inertia increases, reflecting the decrease of the scissors frequency. For the thermal cloud (open circles) the moment of inertia is always consistent with the classical one. Black squares are the moments of inertia for the whole system, obtained combining the thermal and condensed data with a semiclassical model. The temperature-dependence of the moment of inertia is a consequence of superfluidity.

Chapter 2

Dipolar Quantum Gases

In this chapter, we recall the theoretical background on dipolar quantum gases. We start with a discussion on the dipole-dipole interaction (DDI), which has radically different properties from the contact interaction and produces new and interesting effects in quantum gases. Next, we describe the mean-field approximation and the Gross-Pitaevski equation in the dipolar case. Finally, we discuss the corrections which arise from the phenomenon of quantum fluctuations and the stabilization mechanism which they turn out to provide.

2.1 Dipolar interaction

Two dipoles interact via the potential

$$U_{dd}(\mathbf{r}) = \frac{C_{dd}}{4\pi} \frac{(\hat{e}_1 \cdot \hat{e}_2)r^2 - 3(\hat{e}_1 \cdot \mathbf{r})(\hat{e}_2 \cdot \mathbf{r})}{r^5}, \quad (2.1)$$

where \hat{e}_1 and \hat{e}_2 are the directions of the two dipoles and \mathbf{r} their relative position. The constant C_{dd} is $\mu_0\mu^2$ for particles with permanent magnetic dipole moment and d^2/ϵ_0 for particles having a permanent electric moment. If the dipoles are aligned in the same direction, for example the z direction, the interaction potential reduces to

$$U_{dd}(\mathbf{r}) = \frac{C_{dd}}{4\pi} \frac{(1 - 3\cos^2\theta)}{r^3}, \quad (2.2)$$

with θ the angle between the z axis and the vector \mathbf{r} . Equation (2.2) will be the one employed in the following.

The strength of the dipolar interaction dramatically depends on the nature of the dipoles. The magnetic moments of atoms are of the order of the Bohr magneton $\mu_B = e\hbar/2m_e$, while the electric moment for a molecular system is of the order of ea_0 , e being the electron charge and a_0 the Bohr radius. Using the definition for the coupling constant C_{dd} given above, we can derive an order-of-magnitude ratio

$$\frac{\mu_0\mu^2}{d^2/\epsilon_0} \sim \frac{\mu_0\mu_B^2}{e^2a_0^2/\epsilon_0} \sim \alpha^2 \sim 10^{-4}, \quad (2.3)$$

where $\alpha = \frac{1}{4\pi\epsilon_0} \frac{e^2}{\hbar c}$ is the fine structure constant. The DDI is then much stronger between electric dipoles than between magnetic ones.

An alternative measure of the DDI strength is the dipolar length, defined as

$$a_{dd} = \frac{C_{dd}m}{12\pi\hbar^2}. \quad (2.4)$$

In most experiments on dipolar gases, one has to take into account both the dipolar interaction and the contact interaction, described by the s-wave scattering length a . It is, therefore, useful to define the ratio

$$\epsilon_{dd} = \frac{a_{dd}}{a} = \frac{C_{dd}}{3g}, \quad (2.5)$$

which quantifies the importance of dipolar effects in a quantum gas. The quantity $g = 4\pi\hbar^2a/m$ quantifies the intensity of the contact interaction (see section 2.2).

In the following, we report a brief summary of the existing systems in which dipolar interactions are important. The purpose here is just to give the feeling of the existing dipolar systems; the interested reader is referred to [17] and references therein.

Polar Molecules Molecules can have a very high electric moment, which is often measured in Debye, with $1D \sim 3.335 \times 10^{-30}$ Cm. For example, the dipole moment of $^{40}\text{K}^{87}\text{Rb}$ is 0.57 D, that corresponds to a dipolar length $a_{dd} \sim 0.21\mu\text{m}$. With a scattering length of the order of $100a_0$, typical of atoms in BECs experiments, we have $\epsilon_{dd} = 20$. Thus, a gas of dipolar molecules would be dominated by the dipolar interaction. To possess a permanent dipole moment, a molecule needs to be heteronuclear; otherwise, the expectation value of the dipole operator vanishes because of symmetry. Actually, in the absence of an external electric field, also the ground state of a heteronuclear molecule possesses no dipole moment since it is the state of zero angular momentum ($|J = 0, J_z = 0\rangle$). With the application of an electric field, the hamiltonian becomes $\mathcal{H} = \mathcal{H}_{rot} - \mathbf{d} \cdot \mathbf{E}$, where \mathcal{H}_{rot} is the rotational part. The electric field mixes states with different angular momenta, leading to an averaged dipole moment $\langle d \rangle$ different from zero and dependent on the value of E , approaching the permanent value d for large values of the electric field [3]. The main challenge in the field of polar molecules is the lack of efficient techniques for the cooling mechanism: the quantum degenerate regime in a state with relevant electric dipole has not been reached yet.

Rydberg Atoms A highly excited atom, with an electron with a large principal quantum number n , is called a Rydberg atom. The size of such an atom can be enormous since the Bohr radius scales as n^2a_0 : for $n = 100$ the atom's dimensions are of the order of $0.1\mu\text{m}$, typical of small bacteria. The dipole moment has the same scaling as the radius so that Rydberg atoms can reach a value of the dipolar length as big as several μm . However, the excited electron is very weakly bound: its binding energy is a factor n^2 smaller than the binding energy of the ground state. As a consequence, the excited states have short lifetime due to radiative processes. These systems have been employed so far only as a "frozen system", where the dipolar length greatly exceeds the interparticle separation in a dense gas.

Magnetic Dipoles Alkali atoms have $\mu = 1.0 \mu_B$, and therefore dipolar effects are very small in alkali gases. Other atoms of the periodic table offer better opportunities, having a large magnetic dipolar moment in their ground state: for example, chromium has $\mu \sim 6\mu_B$ and $a \sim 100a_0$, so that $\epsilon_{dd} \sim 0.16$, and the dipolar interaction can be observed as a perturbative effect in this gas [46]. Erbium has $\mu \sim 7\mu_B$ and dysprosium, the element used in this thesis experiments, has $\mu \sim 9.93\mu_B$. The advantage of magnetic dipoles compared to the other systems presented so far is that one can apply all the existing and successful techniques for cooling and trapping atoms to reach the quantum degenerate regime. ^{52}Cr has been the first strongly magnetic atom to be Bose-condensed [47]. Erbium BEC was obtained in [48] and dysprosium BEC in [49].

As mentioned above, dipole-dipole interactions possess some striking new features compared to contact interactions, that make dipolar quantum gases a very attractive research field. In particular, as we can see directly from Eq. (2.2), the two main novelties are the long-range character and the anisotropy of the interaction. Both are discussed in detail below.

Long-range character

Formally, a two-body potential $u(r)$ is defined as a short-range potential if it behaves for large values of r as $|u(r)| \sim C/r^{D+\epsilon}$, where C is some constant, D is the dimension of the space, and $\epsilon > 0$. For example, the Van der Waals interaction, usually dominant in a gas of neutral particles, scales as $1/r^6$ for large r , and so it is a short-range interaction in three dimensions. The definition given above can be simply understood thinking about a particle surrounded by a homogeneous distribution of particles with spherical symmetry, with density n and radius of the sphere a . The interaction energy of the particle at the center of the distribution is

$$U = \sum_i u(\mathbf{r}_i) \approx n \int_{r_0}^a u(\mathbf{r}) r^{D-1} d\Omega dr \quad (2.6)$$

where r_0 is some short-range cut-off and $d\Omega$ indicates the integration over the angular variables. For the interaction to be short-ranged, particles far away from the center should give a vanishing small contribution to the potential energy of the central particle. In other words, the particle "feels" only its local neighbors. Mathematically, this request means that the integral in eq. (2.6) should converge for $a \rightarrow \infty$, that translates in the condition stated above, i.e. $|u(r)| \sim C/r^{D+\epsilon}$ for some value of ϵ . If this condition isn't satisfied, the interaction is called long-ranged. Famous examples of long-ranged interaction are, of course, the gravitational and electrostatic interactions, that have a $1/r$ behavior. From eq. (2.2) we see that also the DDI is a long-range interaction in three dimensions, but short-range in one and two dimensions. From a statistical mechanics point of view, the long-range character of a potential determines the so-called "infrared catastrophe" in a physical system: in the thermodynamic limit, the equilibrium configuration isn't the homogeneous one, but the "close-packing" one, in which the particles condense in regions

with high density separated by empty regions, for attractive interactions ($C < 0$), or the configuration with all the particles mashed at the edges of the space, for repulsive interactions ($C > 0$). The gravitational potential belongs to the former case, while the Coulomb potential for charges of the same sign to the latter. In the Coulomb case, the infrared catastrophe is nothing but the well-known result of classical electrostatics for which the free charges get spread over the surface of a conductor. However, in many physical situations, the long-range character of the Coulomb interaction doesn't need to be accounted for because on large scales matter is neutral, and a mechanism of charge-screening comes out. On the other hand, the gravitational interaction is always attractive, and the close-packing configuration constitutes the result of the fragmentation of a homogeneous mass distribution subject to its own gravitational field, which yields, for example, to star formation. The gravitational case is however very delicate and is the subject of intense research in the field of long-range interactions [50]. Returning to the case of the DDI, the close-packing configuration clearly remembers the formation of the droplets which constitute the dipolar supersolid. Theoretical simulations have indeed shown that in two dimensions, where the DDI is short-ranged, no supersolid state exists [51].

The long-range character of the DDI interaction has interesting consequences on the scattering properties of the dipolar gas. As a general result [2], for a central potential falling off at large distances as $1/r^n$, the scattering phase shifts in the ultra-cold regime ($k \rightarrow 0$) behave as

$$\delta_l(k) \rightarrow \begin{cases} k^{2l+1} & \text{for } l < (n-3)/2 \\ k^{n-2} & \text{otherwise.} \end{cases} \quad (2.7)$$

We see that for a short-range potential, such as the Van der Waals interaction ($n = 6$), the dominant phase shift at low energies is the one with $l = 0$, which behaves as $\sim k$. This property allows to describe all the scattering process in term of a single parameter, the scattering length a , and to substitute the real interaction potential with a delta-like and isotropic pseudopotential having the same value of the scattering length of the real one. On the other hand, for the DDI $n = 3$ so that all the phase shifts have the same dependence $\sim k$ and all the partial waves contribute to the scattering amplitude. As a consequence, no pseudopotential can be introduced for the dipolar interaction. An interesting conclusion can be made in the case of Fermi gases: differently from what happens in the contact case, the cross-section for identical fermions colliding via dipolar interaction doesn't vanish at low temperature and can thus be used to perform evaporative cooling, similarly to the boson case. This has been effectively done with fermionic isotopes of erbium [52] and dysprosium [53].

Anisotropy

From Equation (2.2) we see that the DDI is anisotropic, a fact of paramount importance in dipolar systems. The symmetry of the interaction is a d-wave symmetry, described by the second-order Legendre polynomial $P_2(\cos \theta) = (3 \cos^2 \theta - 1)/2$. The numerator in equation (2.2) can be either positive or negative. In particular, the

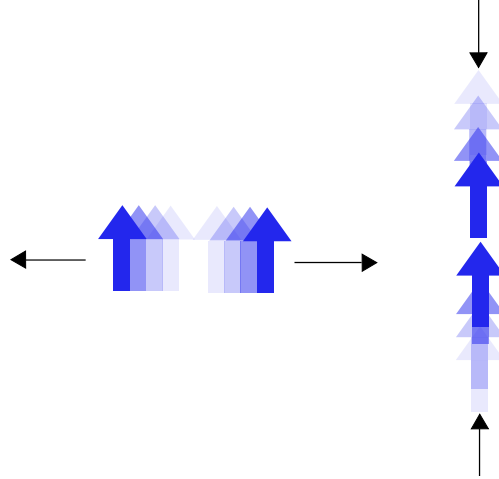


Figure 2.1: Anisotropy of the dipolar interaction. On the left, two dipoles side by side repel each other ($\theta = \pi/2$). On the right, two dipoles in head-to-tail configuration attract each other ($\theta = 0$).

two limiting cases are the "head-to-tail" configuration ($\theta = 0$), for which the DDI is attractive, and the configuration with two dipoles sitting side by side ($\theta = \pi/2$), for which the DDI is repulsive with half the strength of the attractive case (see Fig. 2.1). The DDI can also be zero, for the special value $\theta_m = \arccos(1/\sqrt{3}) \sim 54.7^\circ$, called the magic angle.

It is useful to calculate the Fourier transform of the dipole-dipole interaction U_{dd} and discuss how the anisotropy affects this quantity. The result is

$$\tilde{U}_{dd}(\mathbf{k}) = \int d^3r \frac{C_{dd}}{4\pi} \frac{(1 - 3 \cos^2 \theta)}{r^3} e^{-i\mathbf{k}\cdot\mathbf{r}} = C_{dd}(\cos^2 \alpha - 1/3), \quad (2.8)$$

where α is the angle between the wavevector \mathbf{k} and the polarization axis. We see that the dipolar Fourier transform $\tilde{U}_{dd}(\mathbf{k})$ shares with the contact one $\tilde{V}(\mathbf{k}) = g$ the property of not depending on the wavevector modulus k . However, the anisotropy appears in the dependence on the wavevector direction through the angle α , so that $\tilde{U}_{dd}(\mathbf{k})$ can be either negative or positive.

2.2 Mean-field approach

In this section, we discuss the basic theoretical background for the description of an interacting Bose-Einstein condensate, based on the mean-field approximation: the interactions are treated as a mean field exerted on a given atom by the $N - 1$ other atoms. We first consider the case of contact interactions and then we discuss how to include dipolar interactions.

Contact interactions

Generally, a quantum many body system is treated theoretically with a second quantization approach. For a bosonic system the state is specified by the boson

field operators $\hat{\Psi}(\mathbf{r})$ ($\hat{\Psi}^\dagger(\mathbf{r})$), which annihilate (create) a particle in the position \mathbf{r} , and obey the commutation relation $[\hat{\Psi}(\mathbf{r}), \hat{\Psi}^\dagger(\mathbf{r}')] = \delta(\mathbf{r} - \mathbf{r}')$. The hamiltonian of N particles interacting via a two-body potential $V(\mathbf{r} - \mathbf{r}')$ is written in terms of the boson field operators

$$\hat{\mathcal{H}} = \int d^3r \hat{\Psi}^\dagger(\mathbf{r}) \left(-\frac{\hbar^2}{2m} \nabla^2 + V_{ext}(\mathbf{r}) \right) \hat{\Psi}(\mathbf{r}) + \frac{1}{2} \int d^3r \int d^3r' \hat{\Psi}^\dagger(\mathbf{r}) \hat{\Psi}^\dagger(\mathbf{r}') V(\mathbf{r} - \mathbf{r}') \hat{\Psi}(\mathbf{r}') \hat{\Psi}(\mathbf{r}). \quad (2.9)$$

The first term contains the kinetic and potential energy, while the second term is the interaction energy. In the regime of operation of the current experiments on quantum gases, a lot of simplifying approximations can be made. First, the system is ultracold: the temperatures reached in the condensed phase are of the order of tens of nK. In these conditions, when the atoms interact only with the short-range Van der Waals interaction, all the properties of the interaction are described by a single parameter with the dimensions of a length, the scattering length a , being positive (negative) for repulsive (attractive) interactions. Second, the gas is dilute, with typical density of the order of $n \sim 10^{14} \text{ cm}^{-3}$. Such low densities are necessary to avoid the collapse of the system via three-body losses, that derive from three-body interactions in which two atoms form a molecule and a third atom gets the exceeding energy as kinetic energy. Indeed, the mean separation between atoms is $d \sim n^{-1/3} \sim 200 \text{ nm}$, typically larger than the interaction range, that is of the order of the scattering length. With $a \sim 100 a_0$ one gets that the gas parameter na^3 is $\sim 10^{-5}$. Under these conditions, it is possible to substitute to the real potential $V(\mathbf{r} - \mathbf{r}')$ a pseudopotential that ignores completely the short-range details of the interaction, since the physical properties of the gas are determined only by the asymptotic expression for the wave function of the relative motion during a collision. The most used pseudopotential is then $V(\mathbf{r}) = g\delta(\mathbf{r})$, where the constant g is chosen to reproduce the experimental scattering length a . It is found to be $g = \frac{4\pi\hbar^2 a}{m}$. Whith such a choice the interaction term in the hamiltonian (2.9) becomes

$$\hat{\mathcal{H}}_{int} = \frac{g}{2} \int d^3r \hat{\Psi}^\dagger(\mathbf{r}) \hat{\Psi}^\dagger(\mathbf{r}) \hat{\Psi}(\mathbf{r}) \hat{\Psi}(\mathbf{r}). \quad (2.10)$$

The time evolution of the boson field operator is obtained in the Heisenberg picture

$$i\hbar \frac{\partial}{\partial t} \hat{\Psi}(\mathbf{r}, t) = [\hat{\Psi}(\mathbf{r}, t), \hat{\mathcal{H}}] = \left(-\frac{\hbar^2}{2m} \nabla^2 + V_{ext}(\mathbf{r}) + g \hat{\Psi}^\dagger(\mathbf{r}, t) \hat{\Psi}(\mathbf{r}, t) \right) \hat{\Psi}(\mathbf{r}, t). \quad (2.11)$$

An extremely useful approximation is the mean-field approximation. Generally, the field operators can be expanded on a basis of single-particle wavefunctions $\phi_i(\mathbf{r})$

$$\hat{\Psi}(\mathbf{r}) = \phi_0(\mathbf{r}) \hat{a}_0 + \sum_{i \neq 0} \phi_i(\mathbf{r}) \hat{a}_i, \quad (2.12)$$

where we have written the annihilation operator for the state i as \hat{a}_i . In the presence of Bose condensation a single state (say the $i = 0$ state) is macroscopically populated by $N_0 = \langle \hat{a}_0^\dagger \hat{a}_0 \rangle$ atoms. In the previous expansion, the field operator has a macroscopic component that dominates the other terms. Following the Bogoliubov

prescription, we can replace both the operator \hat{a}_0 and \hat{a}_0^\dagger with the c-number $\sqrt{N_0}$, neglecting the commutator between the two operators (equal to one) with respect to their expectation value (of order $\sqrt{N_0}$). As a result, the expansion (2.12) becomes

$$\hat{\Psi}(\mathbf{r}) = \Psi(\mathbf{r}) + \delta\hat{\Psi}(\mathbf{r}), \quad (2.13)$$

with the classical field $\Psi(\mathbf{r}) = \sqrt{N_0}\phi_0(\mathbf{r})$, and the term $\delta\hat{\Psi}(\mathbf{r})$ that describes quantum fluctuations. The mean-field approximation consists in neglecting this second term and replacing the bose field $\hat{\Psi}(\mathbf{r})$ with the classical field $\Psi(\mathbf{r})$, called the wavefunction of the condensate. The time evolution of this wavefunction is found from eq. (2.11):

$$i\hbar \frac{\partial}{\partial t} \Psi(\mathbf{r}, t) = \left(-\frac{\hbar^2}{2m} \nabla^2 + V_{ext}(\mathbf{r}) + g|\Psi(\mathbf{r}, t)|^2 \right) \Psi(\mathbf{r}, t). \quad (2.14)$$

This is the famous Gross-Pitaevskii equation (GPE), that resembles a standard Schroedinger equation but with the mean field term $g|\Psi(\mathbf{r}, t)|^2$ that takes into account the interactions between atoms and it is responsible for non-linear effects. The mean-field approach of the GPE is analog to the transition from quantum electrodynamics to the Maxwell equations. Indeed, also in this latter case, a large number of photons that occupy the same quantum state allows for a description in terms of classical fields. The GPE depicts the same limit for matter waves, when the corpuscular nature of matter is no longer important.

The stationary solutions of the GPE evolve in time with the chemical potential μ : $\Psi(\mathbf{r}, t) = \Psi_0(\mathbf{r})\exp(-i\mu t/\hbar)$. The GPE assumes in this case its stationary form

$$\left(-\frac{\hbar^2}{2m} \nabla^2 + V_{ext}(\mathbf{r}) + g|\Psi_0(\mathbf{r})|^2 - \mu \right) \Psi_0(\mathbf{r}) = 0. \quad (2.15)$$

The contact mean-field energy for a homogeneous system in a volume V is

$$E_{contact} = \frac{g}{2} \int d^3r |\Psi_0|^4 = \frac{gn^2V}{2}, \quad (2.16)$$

where the density is the squared modulus of the wavefunction, $n = |\Psi_0|^2$.

Dipolar interactions

To describe quantitatively a dipolar quantum gas we need to introduce the dipolar interaction energy in the GPE (2.15). In this case we can't resort to a contact-like potential since the interaction is long-range, so that the dipolar potential in the mean-field approximation reads [17]

$$\Phi_{dd}(\mathbf{r}) = \int d^3r' U_{dd}(\mathbf{r} - \mathbf{r}') |\Psi_0(\mathbf{r}')|^2, \quad (2.17)$$

where U_{dd} is the dipolar potential (2.2). The GPE thus contains two contributions to the mean-field energy

$$\left(-\frac{\hbar^2}{2m} \nabla^2 + V_{ext}(\mathbf{r}) + g|\Psi_0(\vec{r})|^2 + \Phi_{dd}(\mathbf{r}) - \mu \right) \Psi_0(\mathbf{r}) = 0, \quad (2.18)$$

and it becomes a non-local equation, due to the integral appearing in Φ_{dd} .

It is useful to reformulate the GPE exploiting the phase and modulus of the condensate wavefunction: $\Psi_0 = \sqrt{n}\exp(iS)$. Replacing this expression in the time-dependent version of eq. (2.18) and separating imaginary and real part, we get two equations

$$\begin{cases} \frac{\partial}{\partial t}(n) + \nabla \cdot (n\mathbf{v}) = 0 \\ m \frac{\partial}{\partial t}(\mathbf{v}) = -\nabla \left(m \frac{v^2}{2} + gn + \Phi_{dd} - \frac{\hbar^2}{2m} \frac{\nabla^2 \sqrt{n}}{\sqrt{n}} \right) \end{cases} \quad (2.19)$$

These are hydrodynamic equations describing a fluid with density n and velocity $\mathbf{v} = \frac{\hbar}{m} \nabla S$. They are the equations presented in Section 1.1 in the general context of superfluidity, applied to the dilute quantum gases case. The first one is the continuity equation, expressing conservation of the mass, while the second one is an Euler equation for a fluid with zero viscosity, where the last term is called quantum pressure and takes into account inhomogeneities in the density.

Thomas-Fermi approximation

In typical experiments on quantum gases, the trapping potential is harmonic

$$V_{ext}(\mathbf{r}) = \frac{m}{2}(\omega_x^2 x^2 + \omega_y^2 y^2 + \omega_z^2 z^2). \quad (2.20)$$

The mean frequency is defined as $\bar{\omega} = \sqrt[3]{\omega_x \omega_y \omega_z}$, and the mean harmonic oscillator length is $a_{ho} = \sqrt{\hbar/(m\bar{\omega})}$. The Thomas-Fermi approximation consists in neglecting the kinetic energy with respect to the other energies in the GPE [2]. This is legitimate when $Na/a_{ho} \gg 1$, a condition typically fulfilled in a quantum gas. In our experiment, with trap frequencies $2\pi \times (23, 46, 90)$ Hz, $N \sim 4 \times 10^4$, and $a \sim 100 a_0$ we get a value of ~ 176 . The GPE for non-dipolar BEC (2.15) in the Thomas-Fermi approximation has the simple solution

$$n(\mathbf{r}) = |\Psi(\mathbf{r})|^2 = \frac{\mu - V_{ext}(\mathbf{r})}{g}. \quad (2.21)$$

The radii of the condensate are found imposing $V_{ext}(\mathbf{R}) = \mu$, resulting in $R_i = \sqrt{\frac{2\mu}{m\omega_i^2}}$, $i = x, y, z$. Therefore the density can be written as

$$n(\mathbf{r}) = n_0 \left(1 - \frac{x^2}{R_x^2} - \frac{y^2}{R_y^2} - \frac{z^2}{R_z^2} \right), \quad (2.22)$$

where $n_0 = \mu/g$ is the density at the centre of the trap. The BEC has the same aspect ratio of the trap, because $R_i/R_j = \omega_j/\omega_i$, $\forall i, j$. When the density is projected into one dimension, it has the form of an inverted parabola.

The Thomas-Fermi approximation in the dipolar case doesn't lead to a simple solution as in the case of pure contact interactions, because of the presence of the

mean-field dipolar potential Φ_{dd} in the GPE (2.18). One could expect that the solution in this case should be completely different, but, surprisingly, the two cases are quite similar. The calculation is performed in [54]. The trick consists in rewriting Φ_{dd} as

$$\Phi_{dd}(\mathbf{r}) = -C_{dd}\hat{e}_i\hat{e}_j\left(\nabla_i\nabla_j\phi(\mathbf{r}) + \frac{\delta_{i,j}n(\mathbf{r})}{3}\right), \quad (2.23)$$

where

$$\phi(\mathbf{r}) = \frac{1}{4\pi} \int d^3r' \frac{n(\mathbf{r}')}{|\mathbf{r} - \mathbf{r}'|}. \quad (2.24)$$

The problem is reduced to calculate the field $\phi(\mathbf{r})$, which is an "electrostatic potential" generated by a "charge density" $n(\mathbf{r})$. The calculation is therefore tackled using well-known mathematical techniques from electrostatics. The remarkable result is that Φ_{dd} has a parabolic shape, as the trapping potential, so that also the density n of the dipolar gas has the form of an inverted parabola, see eq. (2.22). Of course, the radii R_i have different values, and they can't be expressed analytically. A general feature is that the dipolar cloud becomes elongated in the direction of the magnetic field that aligns the dipoles, a phenomenon called magnetostriction (see Fig. 2.2). The intuitive reason is that the dipoles prefer an head-to-tail configuration, because they feel the attractive nature of the dipolar interaction.

In the Thomas-Fermi limit, a useful expression for the mean-field dipolar energy can be obtained using a Gaussian variational ansatz [17], resulting in

$$E_{dipolar} = -\frac{gn^2V}{2}\epsilon_{dd}f(\kappa), \quad (2.25)$$

where $\kappa = R_x/R_z$ is the aspect ratio of the condensate. The function $f(\kappa)$ monotonically decreases, from $f(0) = 1$ to $f(\infty) = -2$. The magnetostriction effect can then be thought also as an effort to maximize $f(\kappa)$ so that the interaction energy in eq. (2.25) is minimized.

Stability of the dipolar gas

Since the dipolar interaction can be both attractive and repulsive, the conditions for the stability of a dipolar gas aren't obvious. First, we consider a homogeneous gas. In the presence of pure dipolar interaction, we expect that the dipoles should align one over the other and form a long wire, leading to collapse. The presence of a repulsive contact interaction is, therefore, necessary to reach stability. Given an equilibrium density n_0 , we consider small density and velocity excitations with frequency ω and wavevector k around equilibrium. The excitation spectrum that links ω and k is obtained linearizing the hydrodynamic equations (2.19), and reads

$$\omega = k\sqrt{\frac{n_0}{m}\left[g + C_{dd}\left(\cos^2\alpha - \frac{1}{3}\right)\right] + \left(\frac{\hbar k}{2m}\right)^2}. \quad (2.26)$$

This expression is similar to the Bogoliubov spectrum for a homogenous BEC with only contact interactions [2], whose Fourier transform g is complemented by that of the dipolar interaction (2.8), which introduces a dependence on the angle α between

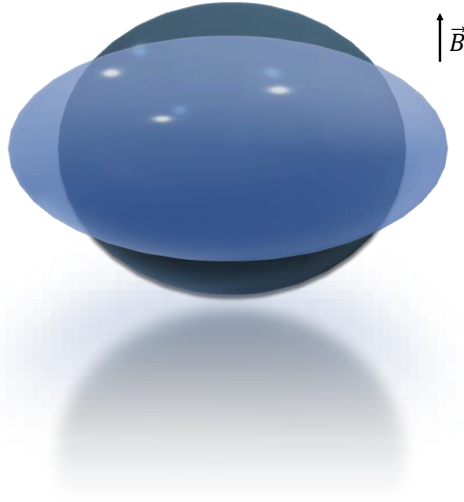


Figure 2.2: Magnetostriction effect. The light blue ellipsoid is an isopotential surface of the trapping potential, while the dark blue ellipsoid is the atomic cloud, elongated in the direction of the magnetic field.

k and the dipole direction z . The spectrum, therefore, is composed of different curves, one for each value of α (see Fig. 2.3). For a fixed α , the spectrum shows a phononic behaviour at low k and a parabolic one in the single-particle regime, for high values of k , when kinetic energy dominates. In the phononic regime $\hbar\omega = \hbar sk$, where the sound velocity s is anisotropic

$$s = \sqrt{\frac{n_0}{m} \left[g + C_{dd} \left(\cos^2 \alpha - \frac{1}{3} \right) \right]}, \quad (2.27)$$

and reduces to the non dipolar case $s_0 = \sqrt{n_0 g / m}$ in the absence of dipolar interaction. The system becomes unstable when phonons acquire imaginary frequencies, i.e. ω becomes imaginary for $k \rightarrow 0$ in eq. (2.26). This phonon instability is driven by the dipolar interaction and happens when $\epsilon_{dd} > 1$. The choice of the constants in the definition (2.4) for the dipolar length was indeed motivated by this stability condition. We can also see that a purely dipolar condensate ($g = 0$) is unstable as expected. Between all the excitation curves, the most unstable is the one with $\alpha = \pi/2$, i.e. the one with the direction of the density modulation perpendicular to the dipoles. Such a modulation, indeed, aligns the dipoles one over the other, while in the opposite case ($\alpha = 0$) the dipoles tend to repel each other side-by-side.

When the gas is trapped, the excitation spectrum is modified. The stability condition doesn't depend anymore only on the interaction parameter ϵ_{dd} , but also on the form of the trap. Intuitively, strong confinement in the direction of the dipoles is needed to avoid head-to-tail configurations and suppress the attraction between dipoles. For simplicity, we consider an axially symmetric trap, with $\omega_x = \omega_y$. We define the trap parameter $\lambda = \omega_z / \omega_x$. For a given value of λ , a critical value of the contact scattering length a_{crit} will exist under which the condensate is unstable.

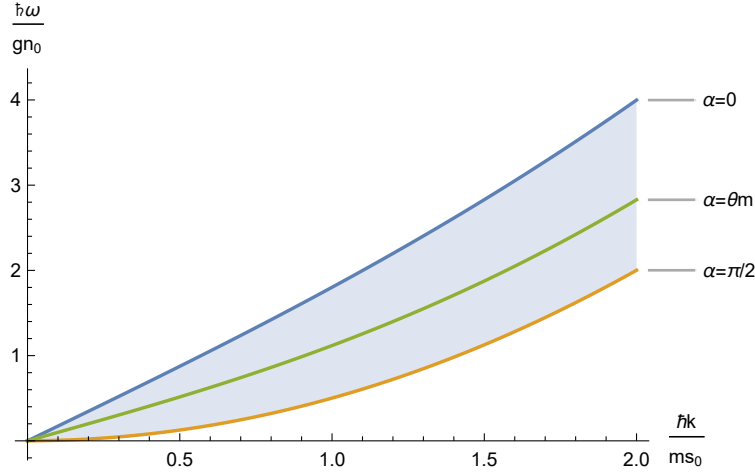


Figure 2.3: Excitation spectrum for a homogeneous dipolar gas. The spectrum has different branches, one for each value of α . For low k the curve is linear, corresponding to the phononic excitations. The most stable (unstable) excitation is the one with $\alpha = 0$ ($\alpha = \pi/2$). For $\alpha = \theta_m$, the magic angle defined in section 2.1, the dipolar Fourier transform is zero, and the spectrum is equal to the non-dipolar one.

The function $a_{crit}(\lambda)$ can be found solving numerically the GPE; an approximate solution can be recovered with a Gaussian variational ansatz, see [17] for details. The intuitive picture is confirmed: in a cigar-shaped trap with the dipoles oriented along the weak trap axis, the dipolar condensate is unstable also with weak repulsive contact interactions, while in a pancake-shaped trap it is stable also with weak attractive contact interactions.

Roton minimum

The excitation spectrum of a trapped dipolar gas shows an interesting feature: a minimum at non-zero momentum, called, in analogy to superfluid helium, a roton minimum (Fig. 2.4). In helium, the minimum arises from the strong inter-particle interactions, which aren't completely understood from a microscopic point of view so far. The position of the minimum scales as the inverse of the interatomic distance. On the other hand, the minimum in dipolar gases appears although the system is dilute, with the range of the inter-particle interactions much smaller than the mean distance between particles. In analogy with helium, however, the roton minimum is purely induced by the inter-particle interactions. An intuitive explanation of the roton minimum is the following, based on the anisotropy of the dipolar interaction. As we have seen, to obtain a stable dipolar BEC we need to strongly confine the system in the dipole direction, that we call z . We consider excitations propagating with wavevector k in the xy plane. When the wavelength of the excitation is much larger than the harmonic oscillator length in the z direction, $l_z = \sqrt{\hbar/(m\omega_z)}$, the dipoles feel only the repulsive character of the dipolar interaction, and the excitation spectrum is phononic, as in the pure contact case (see Fig. 2.4). Increasing k , the wavelength becomes comparable with l_z . At this point, the dipoles form local

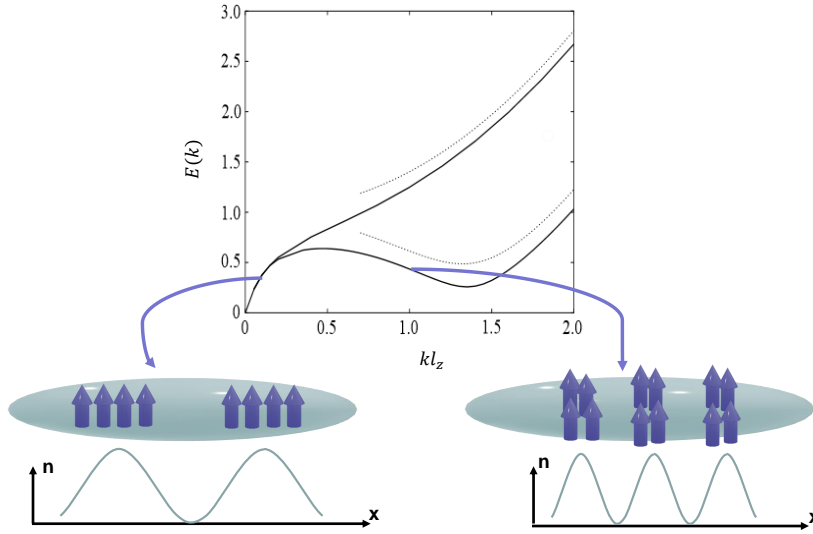


Figure 2.4: Excitation spectrum of a trapped dipolar BEC, from [55]. For low wavevectors k the excitations are phonons because the interaction is mainly repulsive. When $kl_z \sim 1$ a roton minimum occurs because the dipoles feel the attractive part of the dipolar interaction. In the upper curve $\beta = 0.53$ and $\mu/(\hbar\omega) = 46$. In the lower curve $\beta = 0.47$ and $\mu/(\hbar\omega) = 54$. Solid curves are numerical results, while dotted curves are analytical results.

structures in which the 3D nature of the dipolar interaction becomes relevant. Some particles attract each other so that the energy decreases. The attraction is counterbalanced by the repulsive contact interaction and the kinetic energy, which, for higher values of k , starts dominating while the spectrum enters in the single-particle regime.

The existence of a roton minimum in the excitation spectrum of a dipolar condensate was first pointed out in [55]. In this paper, the authors considered an infinite pancake trap, with trap confinement of frequency ω only in the z direction. The system is described by the GPE (2.18) with $V_{ext} = m\omega^2 z^2/2$. The ground state wavefunction is assumed to be independent on the in-plane coordinate $\boldsymbol{\rho}$, so it can be written as $\psi_0(z)e^{-i\mu t}$. The dipolar term in the GPE can be integrated in the coordinate \mathbf{r}' , giving $g_d|\psi_0|^2$, with $g_d = C_{dd}8\pi/3$. The dipolar GPE then becomes a GPE with an effective contact interaction described by the parameter $g + g_d$, with g always considered positive. The solution in the limit $\mu \gg \hbar\omega$ is given by the Thomas-Fermi wavefunction $\psi_0(z) = n_0(1 - z^2/L^2)$, with the central density $n_0 = \mu/(g + g_d)$ and the Thomas-Fermi radius $L = \sqrt{2\mu/m\omega^2}$. The excitation spectrum is then obtained solving the Bogoliubov-de Gennes equations, with the equilibrium density given by $|\psi_0|^2$. Because of the translational invariance in the xy plane, the wavevector k of the excitations is a good quantum number, and it is used to label the excitations. As previously explained, two different regimes are distinguished depending on the value of kl_z . If $kl_z \ll 1$, the excitations are the ones of a gas with repulsive contact interactions with the parameter $g + g_d$, so they are phonons. On the other hand, if $kl_z \gtrsim 1$, we recover the excitations of a gas with contact interactions with parameter $2g - g_d$, which can be both positive or negative.

When the parameter $\beta = g/g_d > 1/2$, the effective interaction is repulsive, and the energy of the excitations always grows with k . When $\beta < 1/2$, i.e. for stronger dipolar interactions, the effective interaction is attractive and the spectrum shows the roton minimum. The roton momentum and the energy gap are given by

$$k_{rot} = \frac{16\mu(1/2 - \beta)}{15\hbar\omega} \frac{1}{l_z}, \quad (2.28)$$

$$\Delta = E(k_{rot}) = \sqrt{(\hbar\omega)^2 - [8\mu(1/2 - \beta)/15]^2}. \quad (2.29)$$

Contrary to helium, the energy gap is tunable by changing the density, the interaction parameter ϵ_{dd} or the trapping frequency. When the Thomas-Fermi approximation can't be applied, the spectrum shows a similar behavior, the principle difference being that, because the kinetic energy in the confined direction is larger, the values of β at which the minimum occurs are less than $1/2$.

The presence of a roton minimum in dipolar quantum gases has been observed experimentally in [56]. The authors induce a roton instability tuning ϵ_{dd} and thus the parameter Δ . The condensate is elongated in the y direction so that the roton minimum develops only for the two modes with $k_y = \pm k_{rot}$. The experimental signature of the roton instability is the transfer of population from $k_y = 0$ to $k_y = \pm k_{rot}$, observed after a free expansion of the gas.

2.3 Quantum Fluctuations

The mean-field theory presented in the previous section has demonstrated to be able to account for several phenomena observed in the first experiments on dipolar quantum gases, for example the modified dynamics in time of flight of Chromium, the d-wave Bose explosion or the form of the excitation spectrum [17]. The mean-field approach, embodied in the GPE, however, completely ignores the quantum fluctuations in the expansion of the field operator (2.13), which means that it doesn't consider the profound quantum nature of the matter waves that form the condensate. The study of the quantum fluctuations for a non-dipolar gas, in the framework of the Bogoliubov theory, leads to two major results: the condensate depletion and a correction to the ground state energy, called the Lee-Huang-Yang correction (LHY). In [57] the authors extended the study of the quantum fluctuations to dipolar gases. One could expect that these effects should lead to small corrections to previously known results, but it turned out that quantum fluctuations in some systems can provide a stabilization mechanism that is responsible for the existence of exotic phases of matters, such as quantum droplets and supersolids.

In section 2.2 we have seen that the boson field operators can be expanded in a basis of single particle wavefunctions, eq. (2.12). The mean-field approximation consists in neglecting all the terms of the expansion other than the one corresponding to the macroscopically occupied state, i.e. the condensed state. Taking into account the next leading terms leads to the Bogoliubov theory. In the homogeneous case (a gas in a box of volume V) the single particle wavefunctions are chosen to be

plane wave characterized by the momentum \mathbf{k} . Substituting the expansion for $\hat{\Psi}$ in the hamiltonian (2.9) and keeping terms to the order $\hat{a}_0^\dagger \hat{a}_0 \sim N$ we obtain the quadratic hamiltonian

$$\hat{\mathcal{H}} = \frac{gn^2V}{2} + \sum \frac{k^2}{2m} \hat{a}_{\mathbf{k}}^\dagger \hat{a}_{\mathbf{k}} + \frac{1}{2} gn \sum_{\mathbf{k} \neq 0} \left(2\hat{a}_{\mathbf{k}}^\dagger \hat{a}_{\mathbf{k}} + \hat{a}_{\mathbf{k}}^\dagger \hat{a}_{-\mathbf{k}}^\dagger + \hat{a}_{\mathbf{k}} \hat{a}_{\mathbf{k}} + \frac{mgn}{k^2} \right). \quad (2.30)$$

The first term is the energy in the mean-field approximation, while the others are corrections due to quantum fluctuations. The last term describes two-body interactions of particles with $\mathbf{k} \neq 0$. It follows that the ground state isn't formed by all the particles in the condensed state $\mathbf{k} = 0$, but a little fraction $(N - N_0)/N \ll 1$ occupies higher-momenta states, where N_0 is the number of atoms in the condensed state. The excited fraction must be very small in order to make significative the expansion of the order parameter. This phenomenon is called quantum depletion and is the first correction to the mean-field theory. The hamiltonian (2.30) can be diagonalized introducing new operators $\alpha_{\mathbf{k}}, \alpha_{\mathbf{k}}^\dagger$, which are a linear combination of the old ones and describe the creation and annihilation of quasiparticles, respectively. The result is

$$\hat{\mathcal{H}} = E_0 + \sum_{\mathbf{k} \neq 0} E(\mathbf{k}) \alpha_{\mathbf{k}}^\dagger \alpha_{\mathbf{k}}. \quad (2.31)$$

The condensate can be thought, then, as a gas of non-interacting quasiparticles which follow the dispersion relation $E(\mathbf{k})$, which is equal to the one obtained linearizing the GPE around the equilibrium solution (2.26). As anticipated, the ground state energy E_0 is the mean-field energy plus the LHY correction

$$E_0 = \frac{gn^2V}{2} \left[1 + \frac{128}{15\sqrt{\pi}} (na^3)^{1/2} \right]. \quad (2.32)$$

The LHY term scales as $(na^3)^{1/2}$, which is small in the limit in which the gas is dilute, the condition for the applicability of the whole theory. In [57] the same calculation was performed including the dipolar interaction. The energy correction in this case is exactly the LHY term with an additional factor

$$\Delta E_{QF}^{dip} = gn^2V \frac{64}{15\sqrt{\pi}} (na^3)^{1/2} Q_5(\epsilon_{dd}), \quad (2.33)$$

where the function $Q_5(x)$ is defined as

$$Q_l(x) = \frac{1}{2} \int d\theta_k \sin \theta_k (1 + \epsilon_{dd}(3 \cos^2 \theta_k - 1))^{l/2}. \quad (2.34)$$

$Q_5(\epsilon_{dd})$ increases monotonically from $Q_5(\epsilon_{dd} = 0) = 1$, in which case we recover the non-dipolar LHY correction, to $Q_5(\epsilon_{dd} = 1) \sim 2.6$. When $\epsilon_{dd} > 1$, $Q_5(\epsilon_{dd})$ acquires an imaginary part, but it is smaller than 10% of the real part in the regimes of interest, so it is usually neglected. A good approximation for the factor Q_5 is given by its Taylor expansion $Q_5 \sim 1 + 3\epsilon_{dd}^2/2$. To theoretically describe an experimental system including also quantum fluctuations as a perturbative effect, an extended

Gross-Pitaevskii equation (eGPE) is usually employed, which is eq. (2.18) with the additional LHY term

$$\left(-\frac{\hbar^2}{2m}\nabla^2 + V_{ext} + g|\Psi_0|^2 + \Phi_{dd} + \frac{32g\sqrt{a^3}}{3\sqrt{\pi}}\left(1 + \frac{3}{2}\epsilon_{dd}^2\right)|\Psi_0|^3 - \mu \right)\Psi_0 = 0. \quad (2.35)$$

Usually, it is very difficult to observe the effects of quantum fluctuations in a quantum gas. One could think to enhance the importance of the LHY term increasing the scattering length a with a Feshbach resonance, but this would increase also the dominant mean-field term. This difficulty can be circumvented in a Bose-Bose mixture, in which two different bosonic species attract each other, while they experience repulsive interactions inside the same species [58]. The mean-field interaction energy depends on an effective scattering length which takes into account both repulsions and attractions, and is zero when the system is expected to collapse in the mean field picture. In a mixture, however, the LHY term is still proportional to the intra-species scattering lengths, and so it will become comparable with the mean field energy near the collapse threshold, while continuing to be positive. Since quantum fluctuations have a steeper dependence on n ($E_{QF} \sim n^{5/2}$, while $E_{MF} \sim n^2$), they represent a stabilization mechanism, which is responsible for the existence of a minimum in the energy also in the region of the mean field collapse. The mixture can then exist as a liquid-like droplet that keeps its form without any external trapping: it is called a quantum droplet and has been observed in mixtures of Potassium in different hyperfine states [59, 60].

A similar effect exists also in dipolar gases, where there is just one species of atoms but two different kinds of interactions at the mean-field level, contact and dipolar ones, which can cancel one another and allow quantum fluctuations to become important, as in the case of the mixture. Tuning the repulsive contact interactions via the scattering length a , it is possible to reach the region in which the attractive part of the dipolar interaction, eq. (2.25), makes the total mean-field energy negative, leading to the collapse. As observed in a dysprosium gas [18], however, the collapse stops forming local self-bound droplets, stabilized by the LHY term, which is isotropic and repulsive also in the case of dipolar gases, see eq. (2.33). Contrary to the mixture case, in the dipolar gas the long-range nature of the interaction produce an array of self-bound droplets (see Fig. 2.5). The formation of a droplet crystal observed in strongly dipolar gases is the analog of the Rosensweig instability well known in classical ferrofluids, where a magnetic field breaks the homogeneous surface of the fluid forming an ordered pattern of density peaks [61].

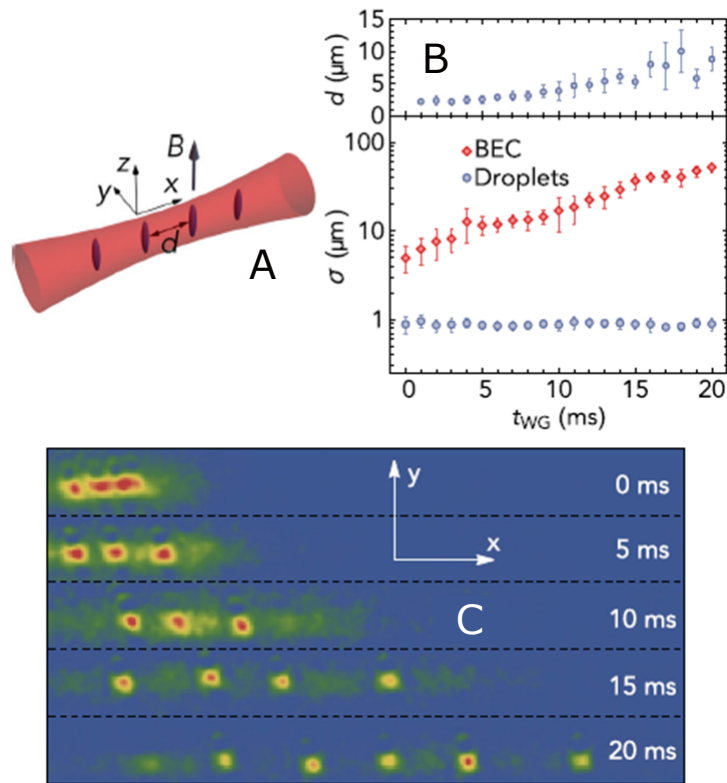


Figure 2.5: Quantum dipolar droplets of dysprosium from [18]. (A) Magnetic droplets in an optical waveguide. They are strongly confined in the y and z directions but free in the x direction. (B) Time evolution of the distance d between droplets and of the dimension σ of the droplets, compared to the BEC expansion. (C) In situ imaging of the motion of the droplets in the waveguide as a function of time. Although the distance between the droplets increases since the initial confining energy is turned into kinetic energy, each droplet keeps its shape, demonstrating that they are self-bound.

Chapter 3

Dipolar Supersolids

This chapter is devoted to the explanation of the main features of the recently discovered dipolar supersolids. Historically, the experimental observation of the dipolar supersolid happened after some years of study of the dipolar incoherent droplets. However, in a logical sequence, the supersolid borders directly with the BEC in the phase diagram and the droplet crystal is a step further. The reason why the observation of the supersolid has been so elusive lies in its narrow parameter space. We then structure this chapter asking why we should expect a supersolid region coming from the BEC side. The discussion is divided into two parts. In the first two sections, we propose an analogy between the theoretical models of soft-core interactions, which predict a supersolid phase, and our trapped dipolar system. We develop a very simple model that explains qualitatively the transition, inspiring to this analogy. In the second part of the chapter, we review the seminal experiments on dipolar supersolids, whose insight has been fundamental, of course, for our experiment on rotations.

3.1 Soft-core models

Some years after Kim and Chan's papers [10, 11], while new experiments and theoretical simulations were casting doubts upon the presence of a supersolid phase in solid helium, some theoretical efforts started focusing on a different and more fundamental question about supersolidity: which kind of interactions between bosonic atoms, if any, could produce a supersolid? Many papers studied two-body interactions which soften at small distances, instead of diverging, and are therefore called soft-core interactions. These are very different from the usual interactions encountered in condensed matter systems, which diverge at small distances and produce normal solids with one particle per lattice site. However, as a matter of fact, simulations of the hard-core crystal of ^4He or similar systems such as parahydrogen show no sign of superfluidity [14]. Also softening the divergence, through slower functions such as the Yukawa potential, doesn't produce any superfluid fraction in a commensurate crystal [62]. On the other hand, many papers reported the presence of a supersolid phase in systems with soft-core interactions, mainly in two dimensions with quantum Monte Carlo simulations [63, 64], or even in three dimensions using the GPE [65]. The fact that a soft-core interaction causes the atoms to group into

clusters is well known in classical physics, for example in the field of colloids and macromolecules [66]. Such a clustering effect can be understood intuitively with the prototype of the soft-core interaction, the step function

$$V(r) = V_0\Theta(R_c - r), \quad (3.1)$$

where $\Theta(x)$ is the Heaviside function, equal to 0 if $x < 0$ and to 1 if $x > 0$. In our case, R_c is the soft-core radius: when the distance between two particles r is less than R_c , the potential gets the finite value V_0 , otherwise it is zero. The step function is plotted in Fig. 3.1 together with other soft-core interactions used in the theoretical papers. The clustering effect happens increasing the density, as it is intuitively explained in Fig. 3.2, due to the finite energy cost for overlapping two or more particles. Indeed, when the mean inter-particle distance is large (so the density is low) the particles don't interact one with the other, and the energy is zero. Increasing the density, when the mean inter-particle distance becomes lower than the soft-core radius R_c , the particles overlap one another and the interaction energy increases. If the system assembles in a normal solid with one particle per lattice site, the interaction energy is NV_0 , with N the number of particles. On the other hand, if the particles overlap in pairs, effectively doubling the lattice constant, the interaction energy lowers to $NV_0/2$: the cluster configuration is thus energetically more favorable. Increasing more the density, more particles occupy the same lattice site and the cluster solid forms. Note, however, that every realistic interaction displays a hard-core at sufficiently short distances. The soft-core models can work when there is a separation in scales between the soft-core radius and the much smaller hard-core one.

In a quantum system, the key ingredient to take into account is the possibility of quantum tunnelling between different clusters, which can establish phase coherence through the system and then induce a superfluid behavior. As pointed out in the theoretical papers cited previously, simulations show that a regime of parameters, typically depending on the density and interaction strength, exists in which atoms in different clusters delocalize and form the so-called cluster supersolid, as opposed to the supersolid expected in solid helium. When the density or the interaction strength are too large, the tunnelling between droplets is suppressed and the system is called an insulating droplet crystal, in which each droplet is superfluid but there isn't any phase coherence between different droplets. Typically, the transitions between the different phases (normal solid, homogeneous superfluid, supersolid, insulating droplet crystal) are described in terms of a parameter defined as

$$\alpha = \frac{V_0}{\hbar^2/(mR_c^2)}\rho R_c^D \sim \frac{E_{int}}{2E_{kin}}N_{cl}, \quad (3.2)$$

where m is the mass of the atoms, ρ the density and D the dimension of the space. Since the droplets radius is of the order of R_c , the parameter α can be interpreted as the ratio between interaction and kinetic energy times the number of atoms in a cluster N_{cl} . When α is low, the system is a homogeneous superfluid, while, for increasing α , first the supersolid and then the insulating droplet crystal are encountered. Typical values of the critical α for the superfluid-supersolid transition are of

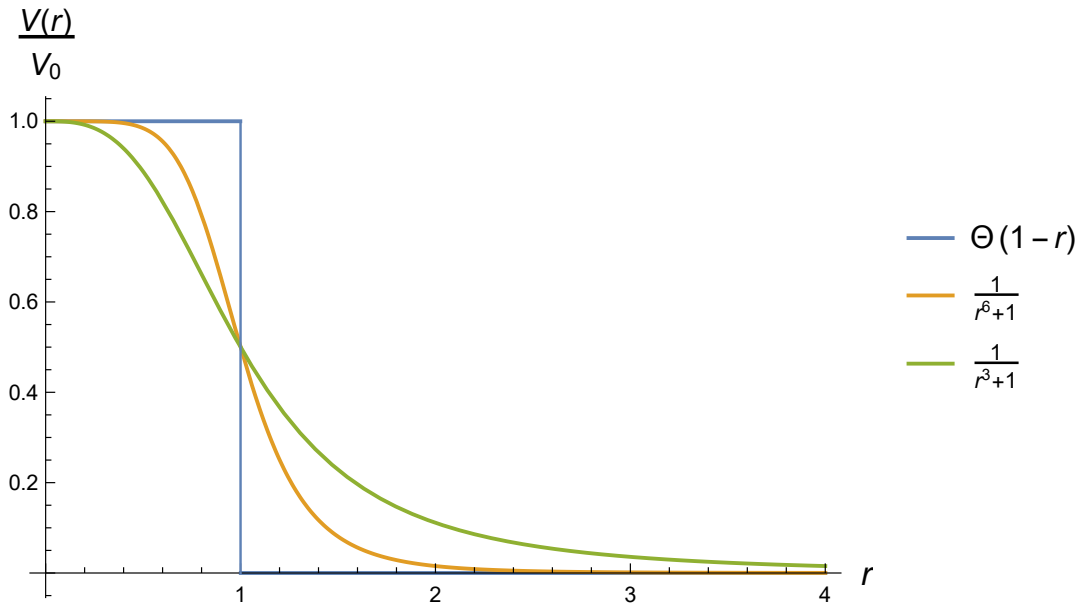


Figure 3.1: Examples of soft-core interactions, with a radius set to $R_c = 1$. The step function of eq. (3.1) is the simplest one and is depicted in blue. Other possibilities are continuous functions with a dipole long-range tale $\propto r^{-3}$ (in green, used in [64]) or a Van der Waals behavior $\propto r^{-6}$ (in yellow, used in [63, 65]).

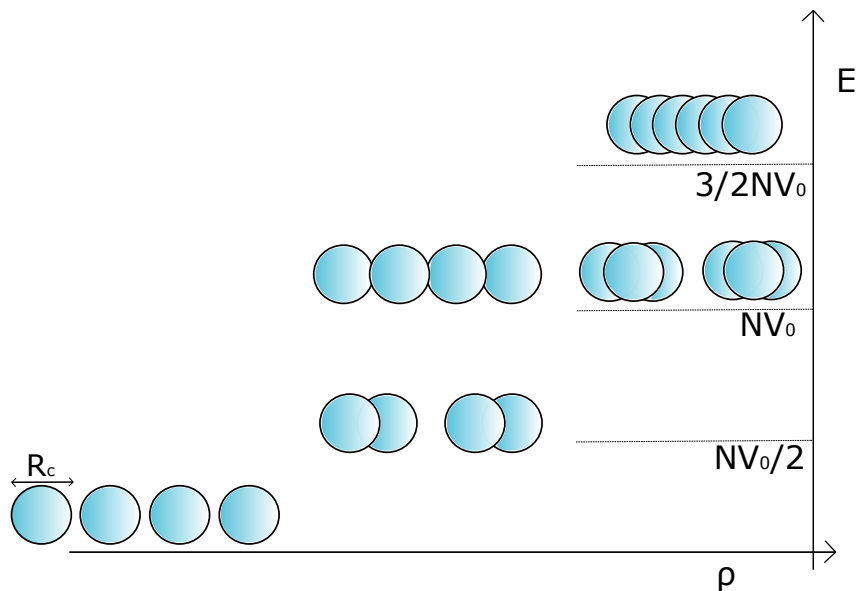


Figure 3.2: Explanation of the clustering effect. With a soft-core interaction such as the step function of eq. (3.1), when the inter-particle distance is lower than the soft-core radius R_c , the most energetic configuration is the one that minimizes the overlaps between particles, which is the cluster state. Increasing further the density ρ , the number of particles per cluster increases.

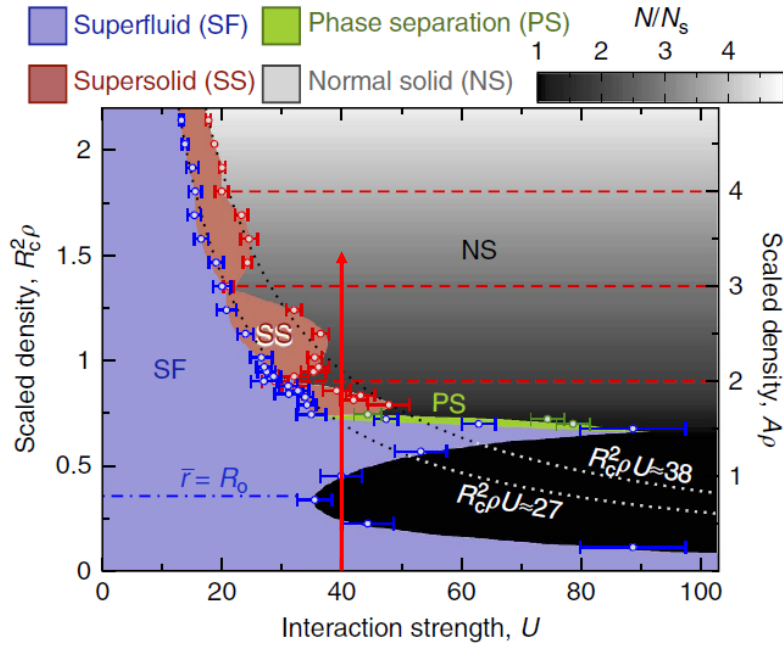


Figure 3.3: Zero-temperature phase diagram of two-dimensional soft-core bosons from [63]. Varying the dimensionless interaction energy U and the dimensionless density ρR_c^2 the system can be in the superfluid (SF), normal solid (NS) or supersolid (SS) phase. The right vertical axis displays the quantity $A\rho$, with A dimension of the unit cell, which is equal to the number of atoms per lattice site, N/N_s . When this number is larger than one, a supersolid phase appears in the phase diagram. If N/N_s is larger than one, but no coherence is established between the droplets, the crystal is called insulating droplet crystal.

the order of 10. How it is demonstrated by the variety of models employed in the literature, the presence of a supersolid phase is quite insensitive to the details of the soft-core interaction, the key ingredient being the finite energy cost for the overlap of two or more particles.

As an example, we show in Fig. 3.3 the phase diagram of a two-dimensional bosonic system interacting through a soft-core potential with a $1/r^6$ tail, obtained with quantum Monte Carlo simulations in [63]. On the horizontal axis, we find the interaction energy U measured in units of kinetic energy (the first factor in the parameter α), while the dimensionless density ρR_c^2 is on the vertical axis. In the graph, lines of constant α are, therefore, hyperbolae. The phase diagram shows the regime of low density and strong interaction, in which a mean-field description isn't successful. To describe the various phases, let's fix the interaction energy U and follow the vertical red line in Fig. 3.3. At low densities, the physics is dominated by the Van der Waals tail of the potential, because the particles are too far apart, on average, to feel the soft-core regime. The system simply crosses a phase transition from a superfluid to a normal solid with one atom per lattice site. When the density increases, the particles are affected by the reduction of the repulsive inter-particle

forces, since they approach one another within distances of the order of R_c : the solid melts again and we find a re-entrant superfluid lobe. After that, the number of particles per lattice site is larger than one, and the clustering effect takes place. Depending on the value of the interactions, the system can be superfluid, supersolid or an insulating droplet crystal. Between the two values $\alpha = 27$ and $\alpha = 38$, supersolid lobes are found, in which the system has a finite superfluid fraction. Interestingly, the supersolid disappears if the atom number per lattice site is an integer, being substituted by a direct superfluid-crystal transition. This is interpreted as a proof of a defect-induced supersolidity, in analogy with the original Andreev-Lifshitz scenario [7]. Increasing the density, this phenomenon disappears and the supersolid is present also with an integer occupation of the lattice sites, signaling the crossover to a regime where the discrete nature of the particles become irrelevant and the mean-field description is correct.

Finally, we point out that the theoretical papers described so far suggested Rydberg BECs as the experimental platform where to search for a supersolid induced by soft-core interactions. The reason is that weakly coupling the atoms to an excited Rydberg state, a soft-core effective interaction settles in between the atoms [65]. However, the experimental implementation of such a system is very challenging, since events of spontaneous emissions or, more dramatically, blackbody radiation can project an atom into the Rydberg state, creating a giant dipole and blocking all the other atoms in their ground state, through the mechanism of dipole blockade [67]. As a result, no experimental study of the supersolid phase with Rydberg atoms has been attempted so far.

3.2 Trapped dipolar bosons as a soft-core model

The dipolar potential

$$U_{dd}(\mathbf{r}) = \frac{C_{dd}}{4\pi} \frac{(1 - 3 \cos^2 \theta)}{r^3} \quad (3.3)$$

doesn't fall, of course, in the group of soft-core potential discussed in the previous section. The clustering effect in dipolar systems is understood in terms of rotonic instability, and the search for dipolar supersolidity has been conducted so far with this kind of physics in mind. Here we propose an alternative approach to supersolidity in dipolar systems, based on the analogy with the soft-core models. In particular, we suggest that the combination of the anisotropy of the dipolar interaction and the presence of a trap could lead to an effective soft-core interaction, which should favor the formation of a supersolid in a proper range of parameters.

To obtain a soft-core model, we want to consider an effective interaction in two dimensions, integrating over the vertical direction z along which the dipoles are aligned. We consider a harmonic trap with length $l_z = \sqrt{\hbar/(m\omega_z)}$ along the z direction and a homogeneous system in the xy plane. The effective two-dimensional interaction is obtained considering a dipole at the center of the trap and integrating over the coordinate θ its dipolar interaction between all the dipoles spread on a

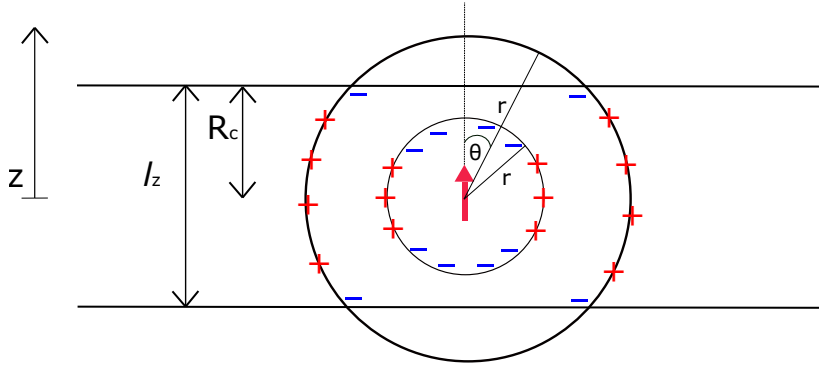


Figure 3.4: Sketch of the geometry used for the integration in eq. (3.4).

spherical surface of radius r , weighted with the density distribution $\rho(z)$ along the z axis. In equations

$$V_{eff}(r) = \frac{C_{dd}}{4\pi} \frac{\int d\theta \frac{(1 - 3 \cos^2 \theta)}{r^3} \rho(z)}{\int d\theta \rho(z)}, \quad (3.4)$$

where $z = r \cos \theta$. See Fig. 3.4 for a sketch of the geometry. The result depends on the form of the density $\rho(z)$. Since we want to justify the transition from a superfluid, the BEC, to a supersolid, the most natural choice for $\rho(z)$ would be the Thomas-Fermi distribution. However, it is known that the density of the dipolar droplets which form crossing the transition can deviate from the usual Thomas-Fermi distribution, having a more rapid decay to zero [68]. Therefore, we choose a more general function

$$\rho(z) = n_0 \left(1 - \frac{|z|^\gamma}{(l_z/2)^\gamma} \right). \quad (3.5)$$

The integral in eq. (3.4) can be solved analytically. The solution is

$$V_{eff}(r) = V_0 \begin{cases} \frac{r^{\gamma-3}}{R_c^\gamma(\gamma+1) - r^\gamma} \frac{2\gamma}{\gamma+3} & \text{for } r \leq R_c \\ \frac{r^2 - \frac{\gamma+1}{\gamma+3} R_c^2}{r^5} & \text{for } r > R_c, \end{cases} \quad (3.6)$$

where we have defined $R_c = l_z/2$. The constant is $V_0 = C_{dd}/(4\pi)$. The reason for the change in behavior at $r = R_c$ is depicted in Fig. 3.4: when the poles of the integration sphere exit from the trap, the effective interaction lacks the contribution from dipoles in a head-to-tail configuration, i.e. a negative contribution. The resulting interaction is mainly repulsive, and for large r it recovers a simple $1/r^3$ shape since the attractive part is negligible. On the other hand, if the sphere is surrounded by the trap, the dipoles contribute with both repulsive and attractive terms, and the effective interaction flattens out. As already said, the result depends

on the form of the density $\rho(z)$, or, given our choice (3.5), on the value of γ . In Fig. 3.5 we report the effective interaction for different values of γ , setting $R_c = 1$. With the standard Thomas-Fermi distribution, $\gamma = 2$, the interaction flattens out at $r = R_c$ but then presents a hard-core, although slower than the pure dipolar one, since it goes as $1/r$. Interestingly, we see that we recover a soft-core interaction with $\gamma = 3$, with the energy that flattens out at the value $V_0/(4R_c^3)$. Actually, the interaction for $r < R_c$ is, in this case, weakly attractive. Increasing the exponent up to $\gamma = 4$, the interaction becomes strongly attractive, with the potential growing linearly with r . In the limit case of $\gamma \rightarrow \infty$, which corresponds to a constant density along z , the interaction jumps to zero for $r < R_c$. Our interpretation of the dipolar BEC-supersolid transition is, therefore, the following: near to the transition, the density along the vertical axis gets a shape that is responsible for the emergence of effective soft-core interaction in the xy plane. The physics of the soft-core interaction, described in the previous section, settles in and leads to the formation of a supersolid in a narrow range of values of density and strength of the dipolar interaction. Incidentally, the fact that, with a further increase in γ , the interaction becomes strongly attractive could explain also the formation of self-bound droplets observed experimentally, and it constitutes a difference compared to the theoretical models described in the previous section, which don't mention the self-boundness properties of the droplet crystal. In that case, indeed, the soft-core interaction can't change in an attractive interaction. Employing the simulated density distributions of [69], we have checked that moving towards the droplet crystal regime, the exponent γ increases. These ideas might be worth investigating in the future to understand the disappearance of global coherence and the transition to an incoherent droplet crystal.

For a better understanding of the most important ingredients which contribute to the supersolid formation, we push forward our soft-core model and use it to extract an order-of-magnitude value for the critical dipolar interaction strength at which the transition happens. To do so, we analyze the various contributions to the total energy of both the homogeneous superfluid and the supersolid and we search which of the two phases is energetically more favorable. Since we want to compare our results with the experimental findings, we consider also a trap in the y direction. We choose to compare two configurations given by the following density distributions

$$\rho_{sf}(\mathbf{r}) = A \left(1 - \frac{r^2}{R_c^2}\right) \quad \rho_{ss}(\mathbf{r}) = B \sin^2\left(\pi \frac{x}{d}\right) \left(1 - \frac{r^3}{R_c^3}\right). \quad (3.7)$$

where $r = \sqrt{y^2 + z^2}$. In the yz plane, we take a standard Thomas-Fermi distribution for the superfluid and its modified version with the exponent $\gamma = 3$ for the supersolid. In the x direction, the superfluid has constant density, while the modulation of the supersolid is approximated with a $\sin^2(\pi x/d)$, which mimics an array of droplets separated by a distance d . The geometry of the cloud is a cylinder with dimension πR_c^2 in the yz plane and height L along the x direction. This is an approximation of the experimental configuration, where soft confinement along x produces a one-dimensional supersolid in this direction. The actual confinement along z is tighter than along y , but the magnetostriction effect tends to make equal the radii of the cloud in these two directions. Going on with the analogy with the

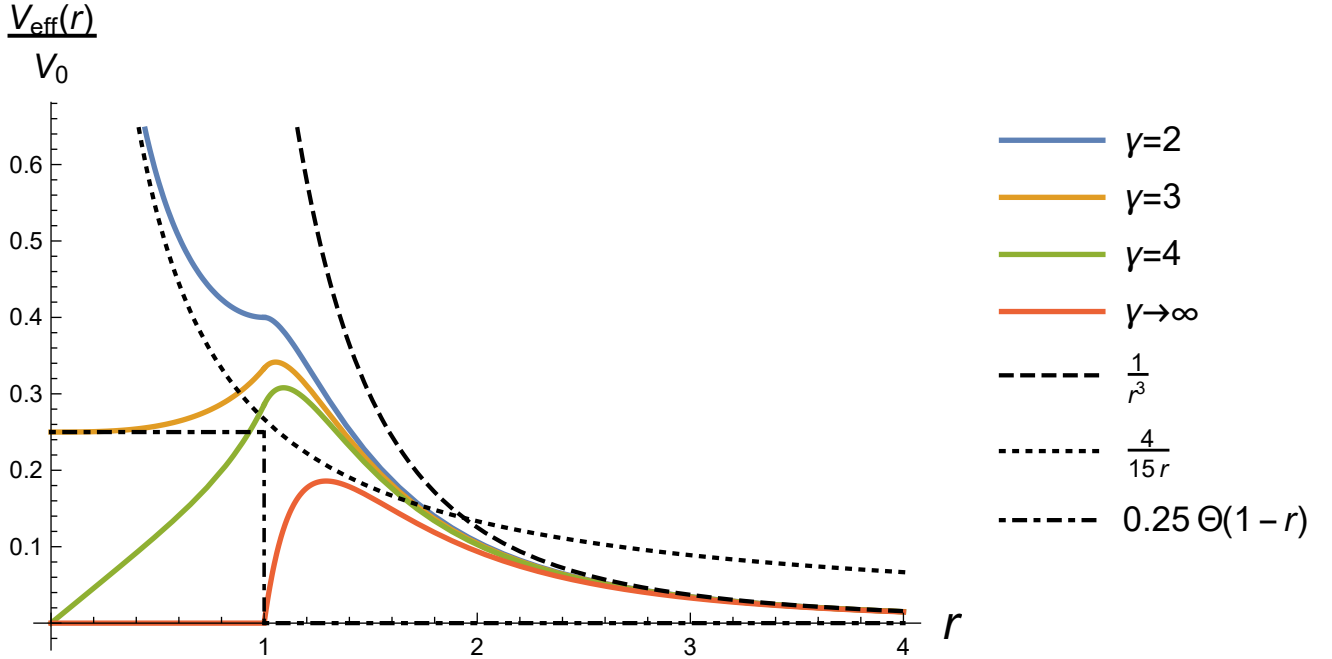


Figure 3.5: Effective interaction in two-dimensions of eq. (3.6), for different exponents γ in the density (3.5), setting $R_c = l_z/2 = 1$. For $\gamma = 3$, which corresponds to a steeper curve than the Thomas-Fermi, we obtain a soft-core interaction with radius R_c . The dashed-dotted line indicates the step function employed in our model, see text.

experimental system, we take $L = 4d$ so that we have 4 droplets. We now set $d = 1$ and use d as unit of length. The constants A and B are determined imposing the normalization condition $\int d\mathbf{r}\rho(\mathbf{r}) = N$, with the atom number fixed, and they are found to be

$$A = \frac{2N}{\pi R_c^2 L} \quad B = \frac{10N}{3\pi R_c^2 L}. \quad (3.8)$$

To evaluate the energy terms we use the mean-field approximation so that kinetic and contact interactions are

$$E_{kin} = \int d\mathbf{r} \left(\frac{\hbar^2}{2m} |\nabla\Psi(\mathbf{r})|^2 \right) \quad E_{contact} = \frac{g}{2} \int d\mathbf{r} \rho(\mathbf{r})^2. \quad (3.9)$$

In principle, we should consider also the trapping energy in the yz plane, but we assume that its change between the two considered configurations is small enough so that it can be neglected. With the same assumption, we also neglect the kinetic energy due to motion in the yz plane, considering only the main contribution which comes from the supersolid modulation in the x direction. To quantify the dipolar energy we employ the soft-core model. Although the calculation of the effective dipolar interaction of eq. (3.6) has been carried out in the hypothesis of a homogeneous system in the yz plane, we performed numerical calculations including a trap also along y . The results show qualitatively the same behavior as the homogeneous case: a soft-core interaction develops for $\gamma = 3$. To make the discussion as

simple as possible, therefore, we approximate the effective dipolar interaction as a step function with coefficient $V_0/(4R_c^3)$ and soft-core radius R_c (see Fig. 3.5), acting only along the x direction, which is the one along which we assumed the supersolid to form. Of course, due to these quite unrealistic assumptions, we can't expect a quantitative agreement with the experiments: the goal here is to sketch a minimal analytical model of the transition, whose principal characteristic is its simplicity.

The dipolar mean-field energy is given by

$$E_{dip} = \frac{V_0}{8R_c^3} \int d\mathbf{r} \int d\mathbf{r}' \Theta(R_c - |x - x'|) \rho(\mathbf{r}) \rho(\mathbf{r}'). \quad (3.10)$$

We first consider the dipolar energy. Our free parameters are the range R_c of the soft-core interaction and its intensity V_0 , which can be recast in terms of ϵ_{dd} through the relation $V_0 = 3g\epsilon_{dd}/(4\pi)$. Experimentally, they can be tuned respectively changing the strength of the trap in the z direction and changing the scattering length through a Feshbach resonance. Both the superfluid and the supersolid have the same dependence on ϵ_{dd} , while their dependence on R_c is found solving analytically the integrals of eq. 3.10. The results are in the form

$$E_{dip}^{sf} = V_0 N^2 F_{sf}(R_c) \quad E_{dip}^{ss} = V_0 N^2 F_{ss}(R_c), \quad (3.11)$$

which are plotted in Fig. 3.6. In the two points $R_c = 1$ and $R_c = 0.55$ the two energies are equal. For the case $R_c = 1$, this happens because it is the analog of the configuration with the hard spheres sitting exactly side-by-side, just before starting to overlap. Lowering R_c , the clustering effect favors the supersolid configuration, whose energy is lower than the superfluid one. Further lowering R_c has also the effect of increasing the intensity of the soft-core interaction, so that, starting from the point $R_c = 0.55$, it is no more convenient to group the atoms together since they interact too strongly.

Now we include also the other energies. We expect the optimal value of R_c to be in between 0.55 and 1, but the exact value depends on the contact energy, which increases while lowering R_c , since the system becomes more compact. Performing the integrals, we obtain

$$E_{tot}^{sf} = \underbrace{\frac{2}{3\pi} \frac{gN^2}{LR_c^2}}_{E_{contact}} + \underbrace{\frac{3g\epsilon_{dd}}{4\pi} N^2 F_{sf}(R_c)}_{E_{dip}} \quad E_{tot}^{ss} = \underbrace{\frac{15}{16\pi} \frac{gN^2}{LR_c^2}}_{E_{contact}} + \underbrace{\frac{3g\epsilon_{dd}}{4\pi} N^2 F_{ss}(R_c)}_{E_{dip}} + \underbrace{\frac{\hbar^2 \pi^2 N}{2m}}_{E_{kin}}. \quad (3.12)$$

We see that the contact energy and, of course, the kinetic energy are larger in the supersolid. This increase has to be counterbalanced by a gain in magnetic energy. To eliminate the dependence on g and keep only the dependence on ϵ_{dd} we substitute $g = \frac{4\pi\hbar^2 a_{dd}}{m\epsilon_{dd}}$, with a_{dd} the dipolar scattering length.

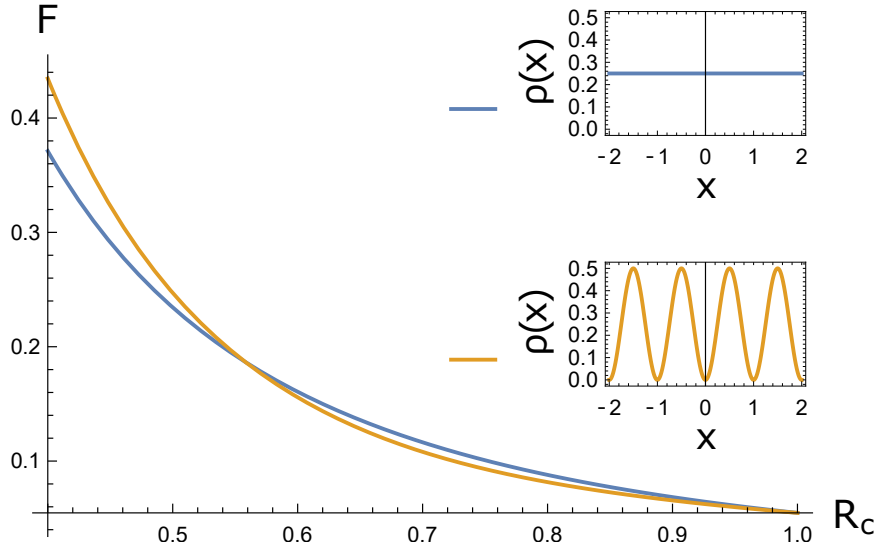


Figure 3.6: Dipolar energy for both a homogeneous superfluid (in blue) and a supersolid (in yellow), as a function of R_c . In the legend the corresponding one-dimensional density distributions in the x direction are shown.

The energies become

$$\begin{aligned}
 E_{tot}^{sf} &= \underbrace{\frac{8\hbar^2 a_{dd}}{3m} \frac{N^2}{LR_c^2 \epsilon_{dd}}}_{E_{contact}} + \underbrace{\frac{3\hbar^2 a_{dd}}{m} N^2 F_{sf}(R_c)}_{E_{dip}} \\
 E_{tot}^{ss} &= \underbrace{\frac{15\hbar^2 a_{dd}}{4m} \frac{N^2}{LR_c^2 \epsilon_{dd}}}_{E_{contact}} + \underbrace{\frac{3\hbar^2 a_{dd}}{m} N^2 F_{ss}(R_c)}_{E_{dip}} + \underbrace{\frac{\hbar^2 \pi^2 N}{2m}}_{E_{kin}}. \quad (3.13)
 \end{aligned}$$

The difference $E_{tot}^{sf} - E_{tot}^{ss}$ is plotted in Fig. 3.7 as a function of the parameters ϵ_{dd} and R_c , using the values of ^{162}Dy . We find, indeed, a transition at $\epsilon_{dd,cr} = 30$ and $R_{c,cr} = 0.73$. For larger values of ϵ_{dd} , the supersolid has lower energy in a whole range of values of R_c . Due to the different scaling of the energies with the atom number N , there is also a critical atom number under which the transition disappears. If N is too low, indeed, the kinetic energy makes the supersolid energy larger than the superfluid one also in the limit of infinite ϵ_{dd} , when the contact energies are zero. This is depicted in Fig. 3.8 for the fixed value $R_c = 0.73$. Under the value $N \sim 4 \times 10^4$ atoms no transition appears. This effect has indeed been observed in the first experiments on dipolar supersolids and in the related simulations [19–21] (see the next section).

So far, we haven't considered the LHY term arising from quantum fluctuations, as described in section 2.3. Other than a probable change in the numerical values of the transition, this term provides a fundamental stability mechanism. Increasing the density, indeed, the soft-core interaction can't prevent the formation of regions at high densities and the consequent collapse of the cloud. Already for the exponent

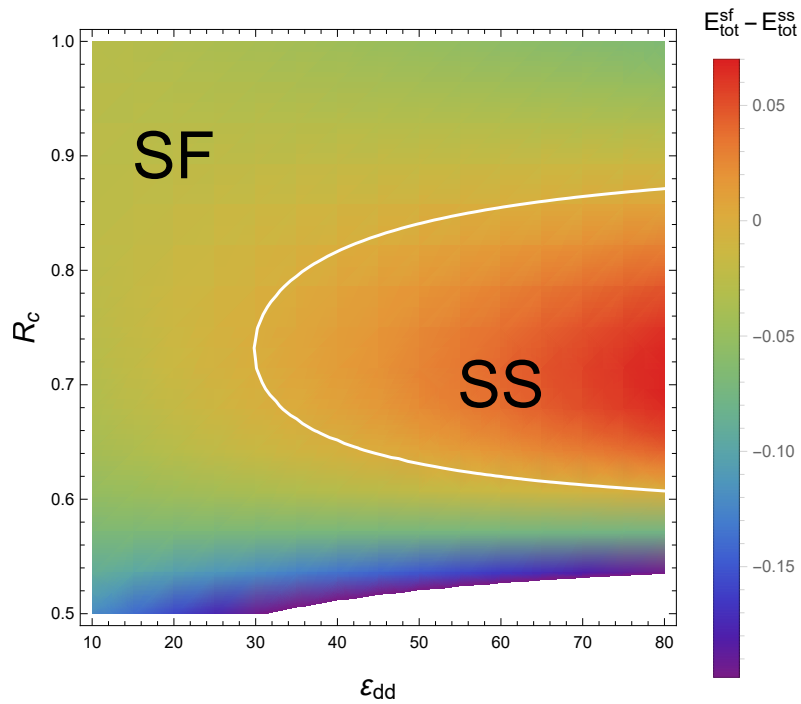


Figure 3.7: Difference between the supersolid and superfluid energies $E_{tot}^{sf} - E_{tot}^{ss}$, from eq. (3.12), as a function of ϵ_{dd} and R_c , for a constant value $N = 10^5$ atoms. The white line indicates the points in which $E_{tot}^{ss} = E_{tot}^{sf}$. Crossing the line means making the transition from a superfluid ground state to a supersolid ground state.

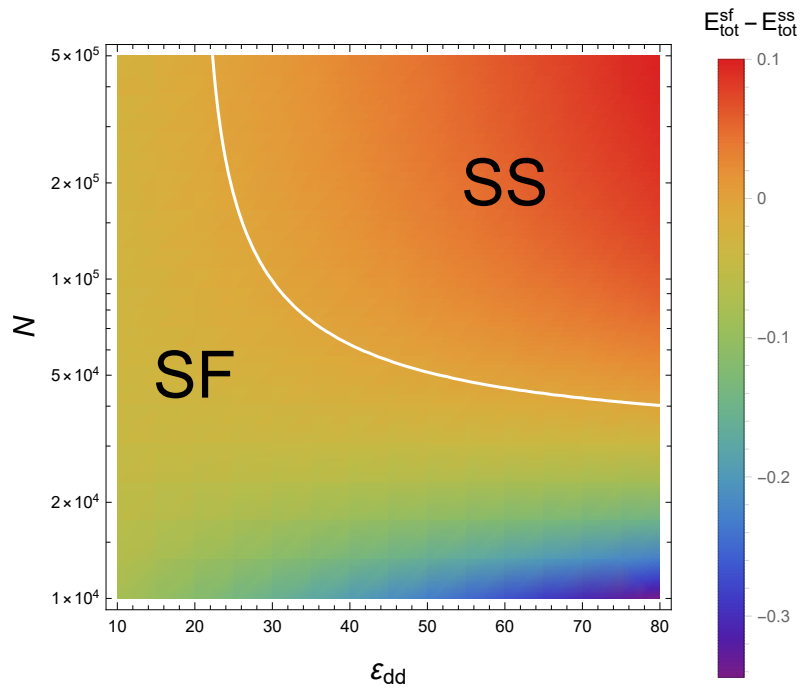


Figure 3.8: Difference between the supersolid and superfluid energies $E_{tot}^{sf} - E_{tot}^{ss}$, from eq. (3.12), as a function of ϵ_{dd} and N , for a constant value $R_c = 0.73$. The white line indicates the points in which $E_{tot}^{ss} = E_{tot}^{sf}$. Crossing the line means making the transition from a superfluid ground state to a supersolid ground state.

$\gamma = 3$, as depicted in Fig. 3.5, the interaction is weakly attractive at short distances, although we have approximated it with a perfect step. With a larger exponent, the interaction becomes even more attractive, as discussed previously.

Despite its failure in producing quantitative predictions, this minimal model is interesting since it gives a simple idea of the different components that are into play in the formation of a supersolid in quantum gases experiments. In the future, we think it would be interesting to make the model more realistic, starting from the effective interaction in two-dimensions, eq. (3.6), and trying to predict some properties of a two-dimensional supersolid, also with the help of simulations. This would be interesting also on the experimental side, since one of the goals of our experiment is to switch from the current one-dimensional supersolid to a two-dimensional array of droplets, with fewer atoms for each droplet so to have a larger droplet number.

3.3 Observation of a dipolar supersolid

In this section, we describe the first experimental observations of a dipolar supersolid. In quantum gases experiments, the starting point is the BEC, a superfluid system, with typical densities of 10^{14} cm^{-3} . To make a comparison with the soft-core models of the previous section, we can take as two-dimensional density $\rho \sim 10^{14} \text{ cm}^{-3} \times l_z \sim 10^{10} \text{ cm}^{-2}$ with $l_z \sim 1 \mu\text{m}$. The dimensionless density of the soft-core model, therefore, would be $\rho R_c^2 \sim 100$, with $R_c \sim l_z$. In the phase diagram of Fig. 3.3 the experimental system would be two orders of magnitude higher, in the region where a mean-field treatment is accurate. To induce the transition to a supersolid state, in the experiments, the scattering length a is tuned through Feshbach resonances, searching the regime in which dipolar interactions spatially modulate the superfluid.

The first observation of a dipolar supersolid was made by the Pisa group in 2018 [19]. The result has been promptly confirmed by the Innsbruck group [20] and the Stuttgart group [21]. Let us discuss the Pisa experiment. The system is a gas of ^{162}Dy atoms, with typical atom number $N \sim 10^4$ and undetectable thermal component, confined in an anisotropic trap with frequencies $\omega_{x,y,z} = 2\pi \times (18.5, 53, 81) \text{ Hz}$. The strong confinement in the z direction, along which the dipoles are aligned, is needed to induce the roton instability, while the weak confinement in the x direction induces the droplets to form in a one-dimensional configuration. The observable is the momentum distribution $n(k_x, k_y)$, detected by absorption imaging after a free expansion. As depicted in Fig. 3.9, three different regimes exist as a function of the scattering length a , tuned with a Feshbach resonance. For $a \gtrsim 100 a_0$, with a_0 the Bohr radius, the ground state is a stable BEC. For $a \lesssim 90 a_0$ the droplet crystal forms, but with no coherence between the droplets, as confirmed by the irregular interference pattern observed in time of flight, with large variation from shot to shot. On the other hand, in the intermediate regime, the momentum distribution shows small side peaks along the weak trap axis, which persist for several tens of milliseconds and keep the same shape in different repetitions of the experiment. The interference patterns observed in time of flight are associated with an in-situ

density modulation. From the images, the position of the peak \bar{k}_x is found to be $1.2(2) \mu\text{m}^{-1}$, similar to the expected roton momentum for an unconfined system in the xy plane, $k_{rot} = 1.53 \mu\text{m}^{-1}$. Also, the phase of the interference pattern is extracted from the momentum distribution (see chapter 4 for details on the fitting procedure and the experimental protocol), whose variance over about 40 realizations for each evolution time is shown in Fig. 3.9, for the supersolid regime. It is clear that coherence between droplets is settled after 10 ms (the time needed for their formation) and is maintained for about 20 ms, before reaching the expectation value for a uniform phase distribution. To support the experimental results, dynamical simulations of the eGPE have been performed by a collaborating group at the University of Hannover, including also the ramp in the scattering length. The simulations contain three-body losses and finite temperature effects. In-trap density distributions are reported in Fig. 3.9 and show the presence of three droplets aligned in the x direction, at a distance of about $4 \mu\text{m}$ one from the other, on top of a BEC background that provides a coherent link between the droplets. In the incoherent regime, the droplets have a small overlap, and the high densities regions induce a rapid decay for three-body losses and strong excitations with high-density variations.

Differently from helium experiments, where supersolidity was searched coming from the classical solid side, the dipolar supersolid stands in the opposite limit, at the transition with a liquid-like superfluid. It is not surprising, then, that it is very different from the hypothetical helium supersolid: it is a cluster supersolid, with very few density peaks, of order unity, and with many atoms per lattice site, of the order of 10^4 .

The other two experiments are quite similar. The main differences are that the Stuttgart group performs also in-situ imaging, with a spatial resolution of $1 \mu\text{m}$, which, however, isn't enough to clearly extract the number of droplets or the overlap between them [21]. The Innsbruck group uses a different isotope of dysprosium, ^{164}Dy , and a different element, ^{166}Er [20]. The trap is more elongated, with trap frequencies $\omega_{x,y,z} = 2\pi \times (300, 16, 222)$ Hz. Erbium has the advantage that the relation scattering length-magnetic field, $a(B)$, is well known, contrary to dysprosium. The results, however, are similar to ^{162}Dy : a supersolid is observed in a narrow range of parameters with lifetimes of the order of 30 ms. On the other hand, ^{164}Dy has a background scattering length smaller than the dipolar length a_{dd} , which allows entering in the supersolid regime tuning B without approaching a Feshbach resonance, therefore limiting the three-body losses. The lifetime of supersolid ^{164}Dy reaches 150 ms. Moreover, this property allows reaching the supersolid regime directly with evaporative cooling, without any magnetic field ramp on the BEC side. With this technique, the Innsbruck group reports lifetimes up to 200 ms.

3.4 Goldstone modes in dipolar supersolids

To gain further insight into the nature of the supersolid state of matter, a series of experiments have been performed to study the spectrum of elementary excitations, which governs the system response to perturbations. Already in the seminal paper of Andreev and Lifshitz [7], it was pointed out that in a supersolid, which is neither

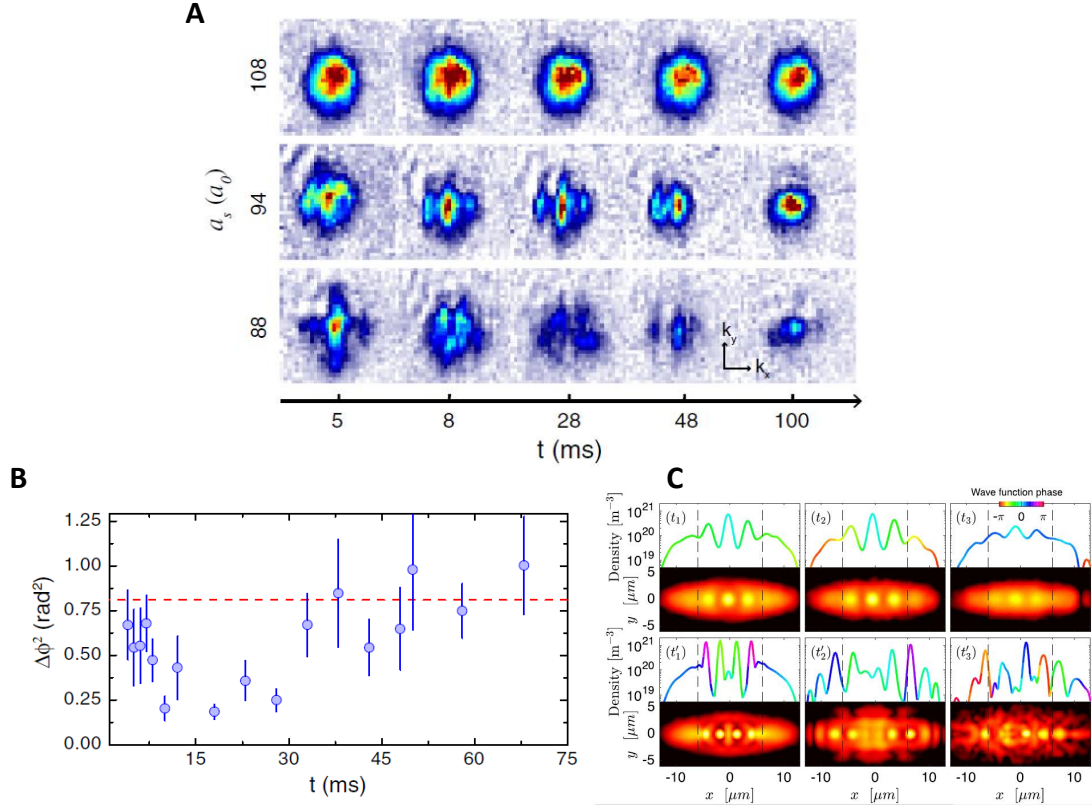


Figure 3.9: Experimental and numerical results from [19]. (A) Momentum distributions as a function of the evolution time for the three regimes, corresponding to three different scattering lengths. In the supersolid regime, side peaks are visible up to tens of millisecond, before a typical BEC is recovered. In the droplet regime, the interference pattern shows no regularity. (B) Time evolution of the phase variance $\Delta\phi^2$. Each point is obtained from about 40 experimental images. The red dotted line is the variance for a uniform phase distribution. Phase coherence is clearly established for about 20 ms. (C) Numerical simulation of the in-trap density, for different times (13.7 ms, 30.9 ms, 55 ms, from left to right). In the upper row, the supersolid is composed of three droplets, which evolve to an excited BEC for longer times. In the lower row, the incoherent droplets have little overlap and rapidly decay. The lines in color show the phase of the system, showing large phase variations in the incoherent regime.

a solid nor a liquid, two kinds of motions should be possible: one associated with the solid nature and the other with the superfluid nature. In their paper, dating back to 1969, the problem was formulated in terms of sound waves. In a more modern language, we should speak about Goldstone modes which appear because of the spontaneous symmetry breaking. Formally, a spontaneous symmetry breaking occurs when the hamiltonian is invariant under a symmetry, but the ground state is not. The most famous example is the Ising model in statistical mechanics: the hamiltonian is invariant under the change of sign of all the spins which form the chain, but, under a critical temperature, the system acquires a finite magnetization M . When this happens, the previous operation isn't a symmetry of the ground state since it changes M into $-M$. In the case of the simple Ising model, no Goldstone mode is expected, since the broken symmetry is a discrete one. When the broken symmetry is a continuous one, the Ginzburg-Landau effective energy near the phase transition has the typical form of a mexican hat, in which a continuum of new energy minima appears [70]. This is the case of generalizations of the Ising model, such as the Heisenberg model, in which the spins are three-dimensional vectors that can point in any direction. In this case, the group of equivalent minima is composed of all the possible directions in which the spontaneous magnetization can point. The Goldstone modes are low-energy modes that link the energy minima one to the other. In the Heisenberg model, they are spin-waves which modify the direction of the magnetization [71]. Another important example is the formation of a crystal, in which case the continuous symmetry to be broken is the translational symmetry. A reduced symmetry persists in the crystal, the one associated with discrete translations. In this case, Goldstone modes are phonon excitations which change the positions of the lattice sites.

The supersolid simultaneously breaks two continuous symmetries: the $U(1)$ symmetry, associated with the locking of the phase of the condensate wavefunction, and, therefore, linked to the superfluid nature of the system, and the translational symmetry, associated with the formation of density maxima and related to the solid properties. As a consequence, the supersolid should exhibit two different Goldstone excitations, each one associated with one of the two natures of the system. Theoretical simulations with Monte Carlo methods for soft-core interactions have indeed predicted that, in a homogeneous system, two different excitations branches appear in the supersolid regime [72] (see Fig. 3.10). One could wonder what is the analog of these kind of excitations, proper of homogeneous systems, in a finite-size system such as the experimental trapped BECs. This is an issue that has been addressed since the first days of experiments on BECs [73, 74]. Differently from the uniform case, where each elementary excitation is determined by its frequency ω and momentum k , in the presence of confinement the momentum k is no more a good quantum number. The elementary excitations are, therefore, classified with other quantum numbers which take into account the symmetries of the problem. For example, in a spherical trap they are the angular momentum l and its third component m . In more general geometries, these modes can mix together. The analog of the phononic branch of the homogenous systems, appearing in the weakly interacting Bose gas explained in the previous Chapter or in liquid helium, are modes which involve the

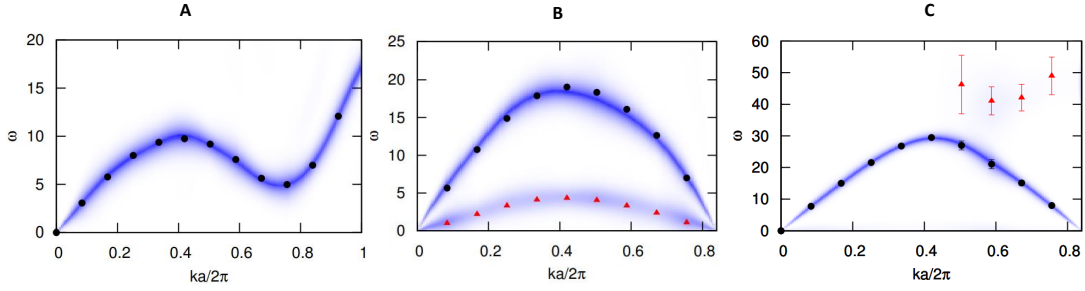


Figure 3.10: Simulations of the excitation spectrum of a soft-core model from [72], in (A) the standard superfluid, (B) the supersolid and (C) the insulating droplet crystal phase. In the supersolid phase, the excitation spectrum is divided into two branches, linked respectively to its superfluid (the lower one) and solid-like (the upper one) nature. The length a is the soft-core radius.

whole condensate, called collective modes. With a back-of-the-envelope calculation, we can convince ourselves that the finite-size of the system determines a minimum excitation energy. In an infinite system, the phononic branch is $\omega = s_0 k$, with $s_0 = \sqrt{\mu/m}$ the sound velocity. If the size (in one dimension) is L , the minimum achievable wavevector is $k_m \sim 1/L$ so that the minimum excitation frequency is $\omega_m \sim s_0 k_m = \sqrt{\mu/(mL^2)}$. In the Thomas-Fermi approximation, the relation between μ and the size L is $\mu = m\omega_{ho}^2 L^2/2$, with ω_{ho} the harmonic frequency of the trap. The minimum excitation frequency is therefore of the order $\omega \sim \omega_{ho}$. The explicit expressions for the excitation frequencies of the collective modes are known for most of the experimental trap geometries [2, 3], obtained solving the hydrodynamic equations in the Thomas-Fermi approximation. The scissors mode explained in section 1.4 is an example of a collective mode. Summarizing, in a trapped gas the excitation spectrum is discretized, and the two branches of the homogeneous system, related to two different sound waves, are mapped onto compressional modes, which are therefore the physical signature of the broken symmetries in the current experiments.

The Innsbruck group studied theoretically the excitation spectrum of a trapped gas of both erbium and dysprosium, near to the transition, simulating the eGPE [24]. They considered only excitations along the weak trap axis. The spectra are composed of discrete modes which, in the BEC region, are arranged in a single branch with a roton minimum (see Fig. 3.11), which resembles that of an infinite system. In the supersolid region, two different branches appear, and the spectrum acquires a periodic structure, similar to the Brillouin zones in a crystal, with a primitive reciprocal lattice vector equal to k_{rot} . These features are more evident in the dysprosium supersolid because it is composed of more maxima and finite-size effects are smaller. In the incoherent droplet regime, the lower branch disappears, signaling the disappearance of global coherence. The upper branch survives and hardens since it is linked to the solid-like properties which persist in the droplet crystal regime.

The Pisa group, in collaboration with the theoretical group in Trento, performed an experiment in which the bifurcation is observed and the two different natures of

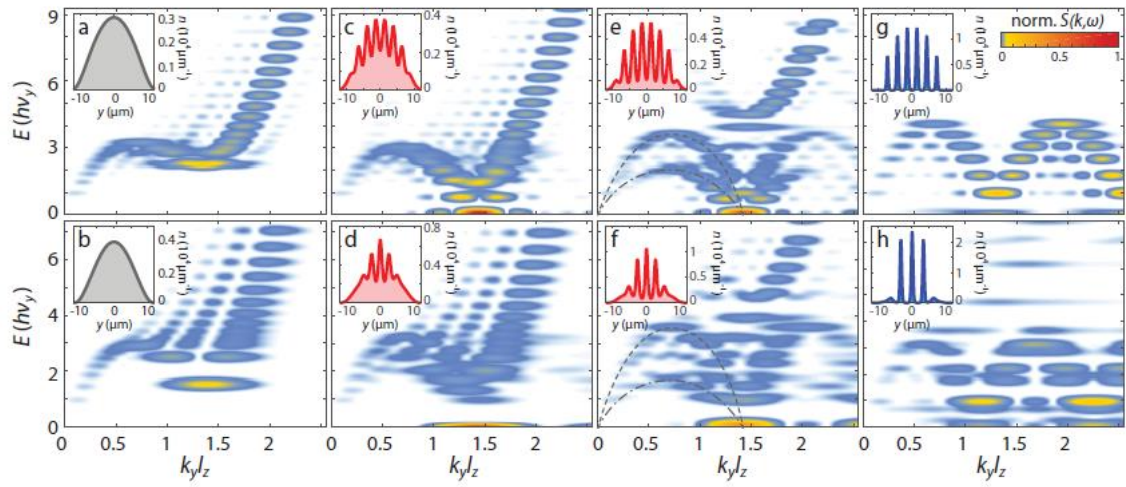


Figure 3.11: Simulation of the excitation spectrum for a trapped Dy (upper row) and Er (lower row) supersolid, from [24]. Each image shows the relation between energy $h\nu_y$ and wavevector $k_y l_z$ for excitation modes in the weak trap axis y , at a given scattering length. l_z is the harmonic length in the z direction. From left to right the scattering length gets lower (92, 91, 90, 81 in units of a_0 , for dysprosium). The colors indicate the dynamic structure factor $S(k, \omega)$, which quantifies the system response to a perturbation with frequency ω and wavevector k . The broadening of $S(k, \omega)$ is a finite-size effect.

the excitations are well illustrated [22]. The study focuses on the lowest compressional mode of the BEC, the so-called axial breathing mode, which consists of an oscillation of the BEC dimension along the weak trap axis x . The simulations of the eGPE from the Trento group study the time evolution of the system width $\sigma_x(t)$, revealing one single frequency in the BEC regime, in agreement with hydrodynamic calculations for a dipolar gas [75], and the beating of two different frequencies in the supersolid regime (see Fig. 3.12 B). In the droplet crystal regime, the lower frequency goes to zero. In the experiment, the observable is the integrated momentum distribution $n(k_x)$ obtained in time of flight. Since the expansion can't be easily modeled, the experimental and theoretical observables aren't directly related. However, the oscillation frequencies aren't affected by the expansion. The breathing mode is spontaneously triggered simply crossing the instability, with an amplitude of 10 %, a fact that could be explained if the transition is of the first order and thus releases energy. While the experimental frequencies for the BEC are in very good agreement with the theory, the time evolution of the momentum width $\sigma_k(t) = \sqrt{k_x(t)^2}$ reveals just one oscillation frequency, larger than the BEC one. The most probable explanation for this discrepancy is the large amplitude of the oscillations, which could mix the two modes. Anyway, the two frequencies of the theory are extracted monitoring two different observables: the relative amplitude between the central and side peak, $A_k(t)$, and the spacing of the side peaks $\bar{k}(t)$ (see Fig. 3.12 A). While $A_k(t)$ is related to the superfluid flow across the droplets, $\bar{k}(t)$ measures the compressibility of the crystal because it depends on the inverse lattice period. Indeed, the two observables oscillate at the two frequencies predicted from the theory and demonstrate the double nature of the supersolid symmetry breaking. Approaching the droplet crystal side, $n(k_x)$ becomes incoherent and prevent from further measurements of the oscillation frequencies.

Similar results have been obtained also by the Innsbruck group [24], as depicted in Fig. 3.13 in the case of erbium. Once that the supersolid forms, collective modes are excited reducing temporarily the harmonic confinement along the weak trap axis. While on the BEC side just one compressional mode gets populated, on the supersolid side this mode opens into two different branches, one of which softens towards the droplet crystal.

The Stuttgart group studied a low-energy Goldstone mode, which embodies both the solid and the superfluid behavior. As depicted in Fig. 3.14, it consists of an out-of-phase oscillation of the droplet array and the superfluid background. When the droplet array is displaced by a quantity Δx from its initial position, a superfluid flow redistributes the atoms in order to keep fixed the position of the center of mass, creating an imbalance η between the two lateral droplets.

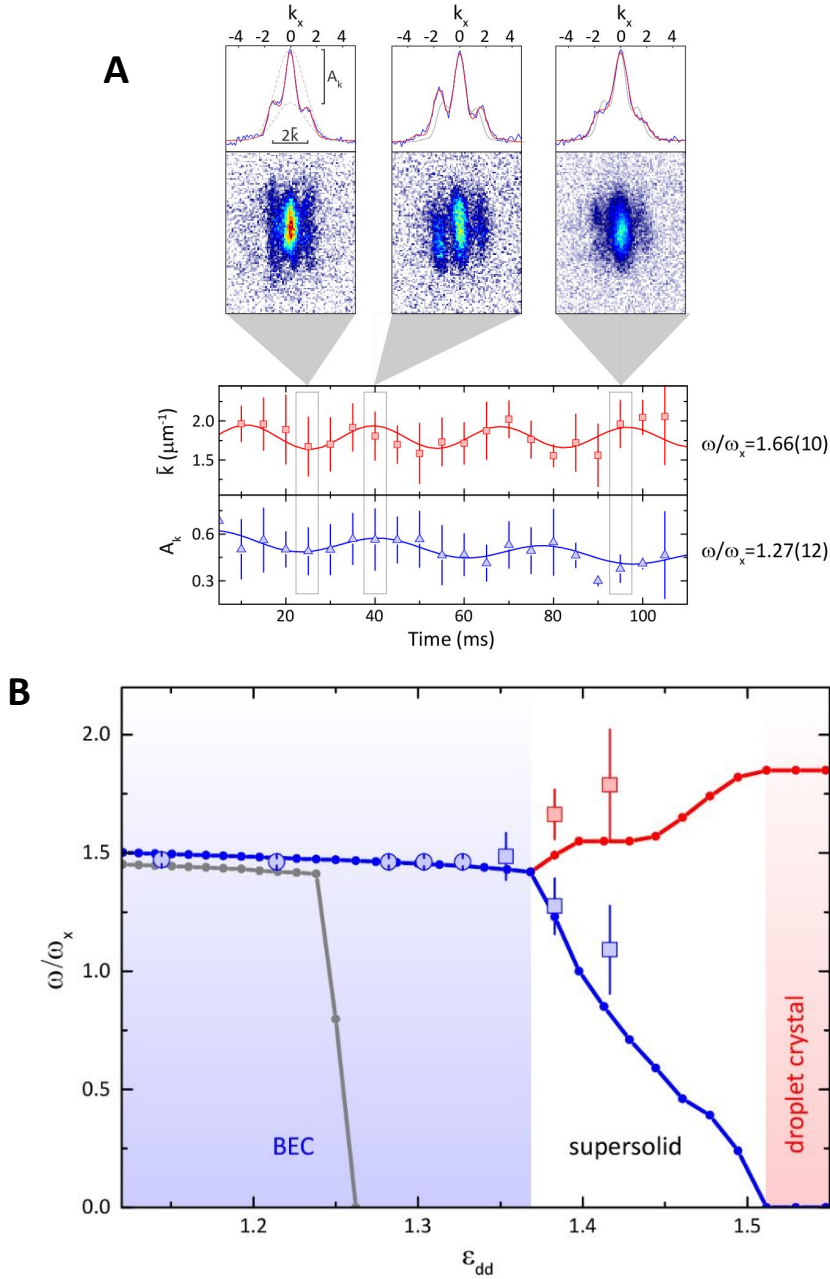


Figure 3.12: Experimental and theoretical results of the axial breathing mode, from [22]. (A) Typical interference patterns in the supersolid regime, and integrated momentum distribution $n(k_x)$, with highlighted the two observables: the relative amplitude A_k and the spacing of the side peaks \bar{k} . In the lower part: time evolution of $A_k(t)$ and $\bar{k}(t)$, fitted with two damped sinusoids which provide two different frequencies. (B) Axial mode frequencies as a function of ϵ_{dd} . Dotted lines are the theoretical frequencies obtained from the simulation of the eGPE. The gray line is the result of the simulation without the LHY term, which predicts the collapse before entering the supersolid regime. Large circles and squares are the experimental frequencies. The splitting of the frequency demonstrates the double symmetry breaking in the supersolid state.

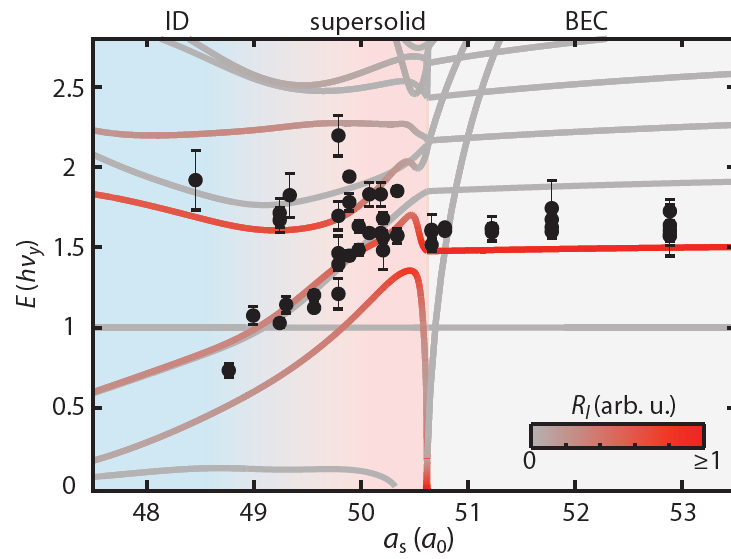


Figure 3.13: Experimental results of the bifurcation of collective modes from [24]. Black dots are experimental frequencies measured inducing a compressional mode. In the supersolid regime, two kinds of excitations appear, signaling the double symmetry breaking. Continuous lines are theoretical excitation energies versus scattering length. The color map indicates the probability to be excited with the actual experimental protocol.

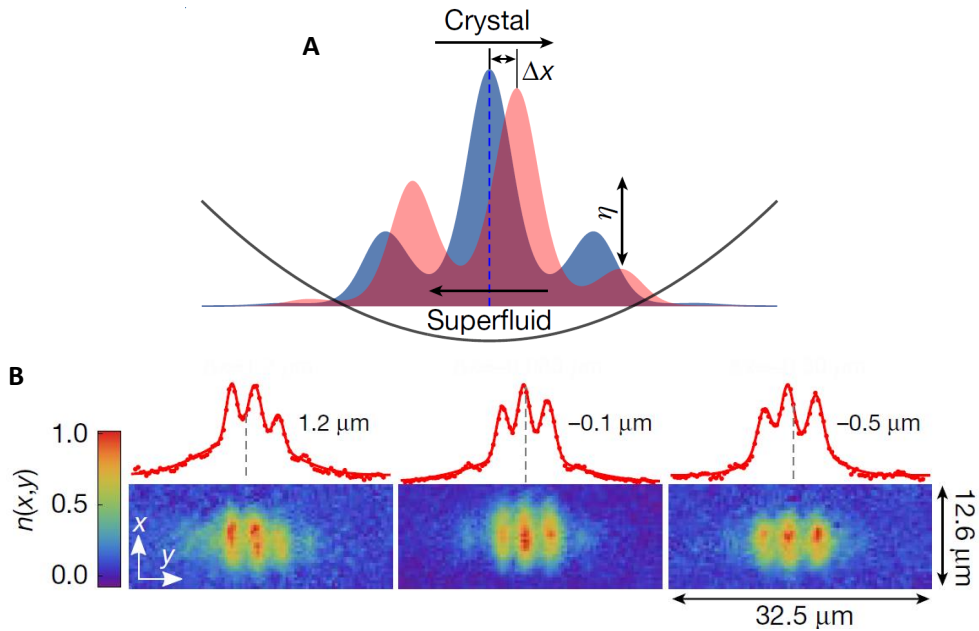


Figure 3.14: Low-energy Goldstone mode observed in the Stuttgart experiment [23]. (A) Sketch of the out-of-phase oscillation of the droplet array and the superfluid background. (B) In-situ images of the supersolid during the oscillation, together with the integrated density and the fit (red lines). The vertical dashed lines indicate the position of the center of mass, which stays unchanged. The numbers indicate the displacement Δx of the droplet array.

Chapter 4

How to make a supersolid

In this chapter, we briefly describe the experimental apparatus for the production of the dipolar BEC and the supersolid. We start discussing the main features of dysprosium, then we review the principal steps for reaching first the quantum degenerate regime and second the supersolid state. At the end of the chapter, we present the fitting procedure used to extract information from the experimental images.

4.1 Dysprosium

Dysprosium is a rare-earth element belonging to the family of lanthanides. Its atomic number is 66, and it is composed of seven isotopes occurring in nature, both fermionic and bosonic. In our experiment, we use the bosonic isotope ^{162}Dy , which has an abundance of 25.45 %. Dysprosium has one of the highest magnetic moment of the periodic table in its ground state, equal to $9.93 \mu_B$, with μ_B the Bohr magneton. This property makes a quantum gas of dysprosium atoms a very interesting platform where to study the effects of the dipolar interaction, and it is the reason why several laboratories in the world are working with this element or are nowadays investing in the building-up of an apparatus for the condensation of dysprosium. The first Dy BEC was obtained in [49], and fermionic Dy was brought to quantum degeneracy in [53].

Some important parameters of ^{162}Dy are reported in Tab. (4.1). The electronic configuration is $[Xe]4f^{10}6s^2$, which is a submerged-shell configuration: the lower-energy $4f$ orbital isn't fully occupied, while the higher-energy orbital $6s^2$ it is. The large magnetic moment arises from this special configuration. In spectroscopic notation, the ground state, determined by the electrons in the open f -shell, is written as 5I_8 , meaning that the total spin is $S = 2$, the total orbital angular momentum is

Table 4.1: Some important properties of the element ^{162}Dy .

μ (μ_B)	mass (amu)	a_{dd} a_0	T_{melting} ($^{\circ}\text{C}$)	T_{boiling} ($^{\circ}\text{C}$)	Ground state	Γ_{421} (MHz)	Γ_{626} (kHz)
9.93	161.93	130	1412	2560	5I_8	$2\pi \times 32.3$	$2\pi \times 136$

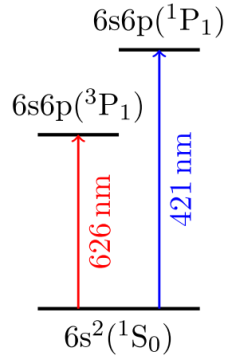


Figure 4.1: The two transitions from the ground state used in the experiment.

$L = 6$, and the quantum number for $\mathbf{J} = \mathbf{L} + \mathbf{S}$ is $J = 8$. Such a high value for J , which means $2J + 1 = 17$ Zeeman sublevels, makes dysprosium interesting for the study of bulk quantum Hall physics [76]. For the bosonic isotopes, the nuclear spin I is zero, so that they don't possess a hyperfine structure. The excitation spectrum is anyway very complicated since excited states can be reached in many different ways, both from the f - and s -electrons. The two transitions used in our experiment are shown in Fig. (4.1). Both are transitions from the ground state with $J = 8$ to an excited state $J' = 9$, involving the s -electrons. As reported in Tab. (4.1), the blue transition at 421 nm has a large linewidth of $\Gamma_{421} = 2\pi \times 32.3$ MHz, while the red one at 626 nm has a narrow linewidth of $\Gamma_{626} = 2\pi \times 136$ kHz. The two transitions are used to cool and trap the atoms. Since the melting temperature for dysprosium is 1412 °C, to obtain an atomic beam we need to heat the sample to very large temperatures. Our experiment begins with an oven at temperature ~ 1275 °C, which is enough for the vapor pressure to produce an acceptable flux of Dy atoms. On the other side, to get an estimate of the critical temperature T_c of condensation for dysprosium, we can use the formula for the non-interacting gas in a harmonic trap with frequencies $\omega_x, \omega_y, \omega_z$ [2]

$$T_c \sim \frac{0.94\hbar}{k_B} (\omega_x \omega_y \omega_z)^{1/3} N^{1/3}, \quad (4.1)$$

where N is the number of atoms and k_B the Boltzmann constant. For our experiment we have $(\omega_x, \omega_y, \omega_z) = 2\pi \times (20, 40, 80)$ Hz and $N \sim 4 \times 10^4$ atoms, so that $T_c \sim 60$ nK. We thus need to lower the temperature of 11 orders of magnitude to reach the quantum degenerate regime, and this is possible thanks to the efficient techniques for cooling and trapping atoms using laser light. Such techniques are well discussed in many textbooks (see for example [2, 77]), and we won't describe them in detail since they are not the central argument of this thesis. In the next section, we touch them briefly, while describing the necessary experimental steps to obtain a dipolar BEC and a dipolar supersolid.

4.2 Experimental apparatus

Here we describe how the two transitions cited previously, the blue line at 421 nm and the red line at 626 nm, are used to cool and trap the atoms. We then discuss the configuration of optical traps in which the BEC is obtained, and how the supersolid transition is induced. Details on the experimental apparatus and sequence can be found in [19, 78, 79].

Blue light and radiative cooling

The main experimental apparatus is depicted in Fig. (4.2). On the extreme right of the figure, we find the oven, where dysprosium is heated up to ~ 1275 °C. From this temperature we can estimate a thermal velocity of the order of $v_{th} \sim 500$ m/s for the atoms exiting from the oven. The interaction with the laser field is used to cool the atoms, exploiting the basic phenomenons of absorption and spontaneous emission of photons. When the atom is in its ground state, it can absorb a photon from the incoming laser, populating an excited state. Then, it can spontaneously emit a photon and come back in the ground state. In each of these processes, the atom gains or loses a momentum equal to $\hbar\mathbf{k}$, with \mathbf{k} the wave vector of the photon. While the absorbed photons have always the same \mathbf{k} , since they come from the laser, the spontaneously emitted photons propagate in random directions, so that after many fluorescence cycles the average momentum which the atom acquires from them is zero. The net effect of the interaction is, therefore, to transfer momentum from the radiation field to the atom, and the resulting force acting on the atom is called the radiation pressure force. The order of magnitude of such a force can be obtained with simple reasoning. During a fluorescence cycle, the mean velocity change of the atom is $\delta v = \hbar k/m$, with m the mass of the atom. The rate R at which photons interact with the atom is the number of fluorescence cycles per second, which is of the order of the inverse of the lifetime τ of the excited state, i.e. $R \sim 1/\tau = \Gamma$, with Γ the linewidth of the transition. The mean velocity change per second is $\delta v/\delta t = R\delta v \sim \hbar k\Gamma/m$, so that the radiation pressure force is

$$F_{RP} = m \frac{\delta v}{\delta t} \sim \hbar k\Gamma. \quad (4.2)$$

The first stage of cooling, after the oven, is done with the blue transition, whose larger linewidth Γ_{421} produces a larger force and then a more efficient cooling. The laser beam propagates against the atom motion so that the atoms are decelerated. Using eq. (4.2) and the values in Tab. (4.1) we obtain $F_{RP} \sim 3 \times 10^{-19}$ N, which corresponds to a deceleration of $a = F_{RP}/m \sim 10^6$ m/s².

The radiation pressure force as a function of the detuning $\delta = \omega_L - \omega_0$, i.e. the difference between the laser frequency ω_L and the atom resonant frequency ω_0 , has a Lorentzian shape: it has the maximum at $\delta = 0$ and decay as δ^{-2} for large detunings. When the atoms move with velocity v , the detuning δ depends on v because of the Doppler effect, $\delta = \omega_L - \mathbf{k} \cdot \mathbf{v} - \omega_0$, and then also the radiation pressure force depends on v . If we limit ourselves to send a laser beam against the moving atoms, the result would be that the atoms with just the right velocity to be resonant with the laser would be slowed down, until they aren't no more in resonance. All the other atoms

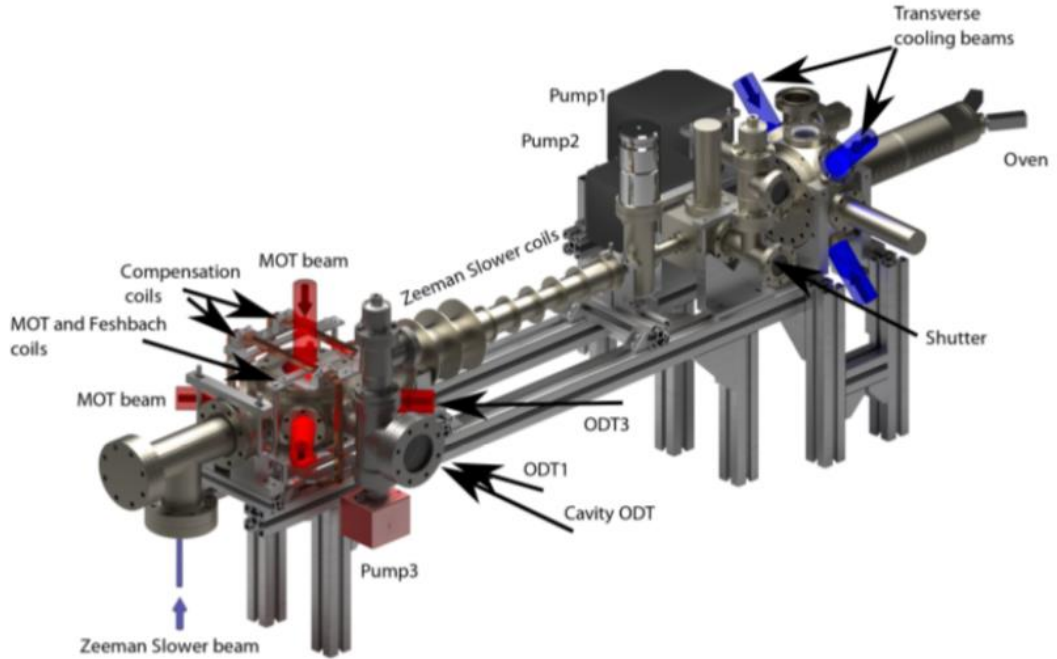


Figure 4.2: Sketch of the experimental apparatus. For a description see the text.

wouldn't be affected by the laser. To produce an efficient slowing, therefore, the Zeeman slower configuration is used. In addition to the blue beam which slows down the atoms, a magnetic field modifies the energies of the Zeeman sublevels, changing the resonant frequency ω_0 and then the detuning δ . With the right configuration of coils, it is possible to produce a magnetic field that keeps the atoms near resonance while their velocity decreases. With a beam power of ~ 150 mW and a negative δ (red detuning) of $\sim 2\pi \times 1.05$ GHz, the final atom's velocity is of the order of 10 m/s.

The blue light at 421 nm is generated in a bow-tie cavity, containing an LBO crystal, which frequency-doubles light at 842 nm emitted by a Ti:Sa laser. Other than the Zeeman slower beam, the blue light is used for three other purposes. Two beams are directed perpendicularly to the Zeeman slower direction just after the oven (see Fig. 4.2), to slow the transverse components of the velocities and limit the divergence of the atomic beam. For this transverse cooling scheme, a power of 75 mW is used. A low-power beam is used to perform saturated absorption spectroscopy directly on Dy atoms: this signal is sent to a PID which actively locks the blue cavity on the atom's resonant frequency. Finally, some of the blue light is used for the imaging system, which is described below.

Red light and MOT

After the Zeeman slower, atoms enter the octagonal science cell, in which ultra-high vacuum is made ($P < 10^{-10}$ Torr). Here they are loaded in the Magneto-Optical-Trap (MOT), which has the double purpose of further cooling the atoms and

trapping them. The MOT is composed of three retro-reflected beams of red light at 626 nm, see Fig. (4.2). The effect of the radiation pressure force from a retro-reflected beam on a moving atom is to produce a velocity-dependent force of the form $F = -\alpha v$, which is a viscous force, with the parameter α depending on detuning and laser intensity. In the MOT, three beams perpendicular one with the other exert a viscous force in all the three dimensions and realize a so-called optical molasse. Such a configuration can slow down atoms but can't trap them. To complete the MOT, hence, two circular coils in anti-Helmholtz configuration are added, which produce a linearly increasing magnetic field along the axes of the coils. As a result, the Zeeman shift is position-dependent and, if the couples of counter-propagating laser beams are respectively σ^+ and σ^- polarized, with considerations based on the conservation of angular momentum in transitions between different Zeeman states, it can be shown that the force acquires a harmonic term: $F = -\alpha v - \beta r$, with r the distance from the center of the trap. Such a position-dependent term allows for atom trapping. In our experiment, the MOT beams have a large waist (1.2-1.8) cm, to increase the capture volume, and the total power is 150 mW. The minimum temperature achievable in a MOT is limited by fluctuations in the radiation pressure force, which arise because of the intrinsically granular nature of the force itself. Indeed, both the fluctuations of the recoil momentum transferred in spontaneous emission processes and of the number of fluorescence cycles per second make the atoms experience a random walk in momentum space [77]. The minimum temperature is called Doppler temperature and it is

$$T_D = \frac{\hbar\Gamma}{2k_B}. \quad (4.3)$$

The narrow linewidth of the 626 nm transition determines a low Doppler temperature of $T_D \sim 3.3 \mu\text{K}$. Such an advantage of the red transition has its negative counterpart in a low capture velocity of the MOT, which is of the order of $v_c \sim 5$ m/s. To increase the number of trapped atoms, during the loading stage the red light is frequency modulated to get a larger effective linewidth and enhance the capture velocity. Then, in the compressional stage, the modulation is switched off and the detuning δ and the intensity I are tuned to achieve the minimum temperature. After the compressional stage typical densities are of the order of 10^{11} cm^{-3} , with atom number $N \sim 5 \times 10^7$, and the temperature is $\sim 20 \mu\text{K}$.

Infrared light and optical dipole traps

To reach the critical temperature for condensation $T_c \sim 60$ nK we need to cool down by three other orders of magnitude. This is done by transferring the system into an optical trap and applying the technique of evaporative cooling. The optical trap is based on the potential energy of an electric dipole \mathbf{d} in an electric field $\mathbf{E}(\mathbf{r})$:

$$U(\mathbf{r}) = -\mathbf{d} \cdot \mathbf{E}(\mathbf{r}). \quad (4.4)$$

When the dipole is induced by the electric field itself, i.e. $\mathbf{d} \propto \mathbf{E}(\mathbf{r})$, the potential energy is proportional to the intensity of the laser, $U(\mathbf{r}) \propto I(\mathbf{r})$. Usually, optical traps operate at large detunings, to avoid the effects of radiation pressure force. Indeed, also the optical potential (4.4) can be recovered as the consequence of a

conservative force acting on the atoms, due to the interaction with light, which scales as $1/\delta$ for large detunings, contrary to the radiation pressure force which decays as $1/\delta^2$. Another physical interpretation of the optical potential is in terms of the position-dependent AC Stark shift of the atomic energy levels [77]. With rigorous treatment, it is found that the sign of the detuning determines the form of the trap

$$U(\mathbf{r}) \propto \frac{I(\mathbf{r})}{\delta}. \quad (4.5)$$

With a focused laser whose intensity has a maximum in space, therefore, a negative detuning produces an optical potential with a minimum, which can trap the atoms. Usually, laser beams have an intensity with a gaussian shape, which, around the intensity maximum (so the potential minimum) can be approximated with harmonic confinement:

$$U(\mathbf{r}) = \frac{1}{2}m(\omega_x x^2 + \omega_y y^2 + \omega_z z^2), \quad (4.6)$$

where the frequencies depend on the laser's powers and waists. Once that the atomic cloud is trapped, it can be cooled via evaporative cooling. This method consists of lowering the optical confinement so that the most energetic atoms leave the trap, while the others thermalize and the final temperature of the sample decreases. Although a fraction of the atoms is lost, and the density decreases, the reachable temperatures are so low that the method allows entering the quantum degenerate regime.

In our experiment, for the optical traps, we use two laser sources with $\lambda = 1064$ nm. The configuration of the optical traps in the science cell is depicted in Fig. 4.3. The first trap is switched on during the MOT compressional stage, and it consists of the standing wave pattern which forms inside an optical resonator. The choice of such a configuration limits the needed power to trap hot MOT atoms at 1 W. The waist of the beam is large, of the order of $300 \mu\text{m}$. The drawback of the resonator is that atoms are transferred from the MOT to an optical lattice with period $d = \lambda/2 = 532$ nm, and this enhances atom losses, which at the end amount to about half of the MOT's atoms. Together with the resonator, another optical dipole trap (ODT1) is switched on, with 1.5 W power and a smaller waist of $41 \mu\text{m}$. The ODT1 traps the atoms while the resonator power is exponentially decreased in 2 s, performing the first stage of evaporative cooling. Afterwards, another beam is ramped up, called ODT3, with an angle $\theta = 40^\circ$ with respect to ODT1 and a power of 2.6 W. The ODT3 is elliptically shaped with the horizontal (vertical) waist of $81 \mu\text{m}$ ($36 \mu\text{m}$) so that the final trap has large vertical confinement with respect to the other directions, which is needed to avoid dipolar collapse. Finally, evaporative cooling is performed in the crossed trap until Bose-Einstein condensation is reached. The BEC's atom number is typically 4×10^4 . The overall sequence is summarized in Fig. 4.3, and, counting also the MOT stage, it lasts 13 s.

Feshbach resonances

As mentioned in chapter 2, the Van der Waals interactions in a gas of ultracold atoms are described, in the mean-field treatment, by a single parameter: the scattering

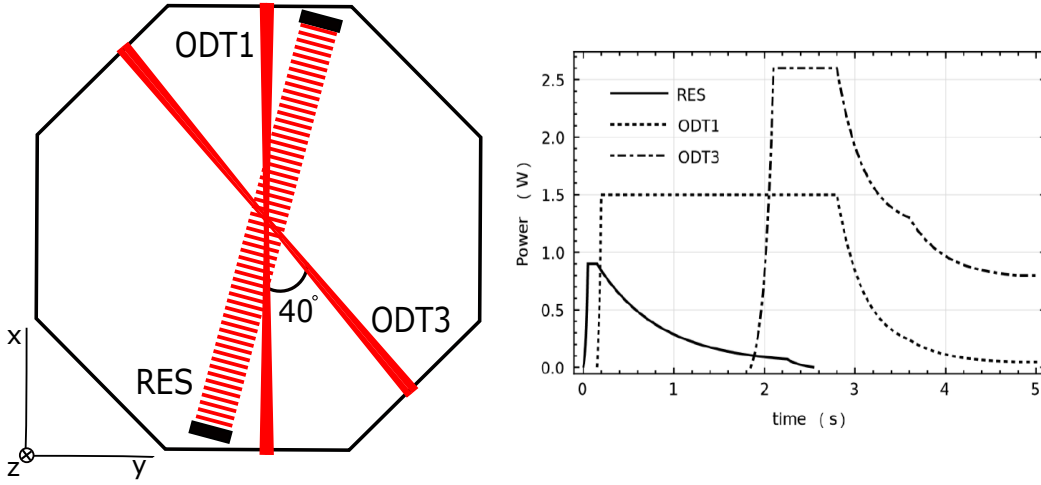


Figure 4.3: Sketch of the optical traps. The symbol 'RES' indicates the optical resonator. On the right, experimental sequence for trapping and evaporative cooling in the optical traps.

length a , which is positive (negative) for repulsive (attractive) interactions. An extremely useful tool in atomic physics is the possibility to tune the scattering length, and then the interactions, through the phenomenon of Feshbach resonances, that appear when, during a collision process, the two colliding atoms pass through a resonant intermediate state where they are bound. In that case, if the energy of the initial state of the two atoms and the energy of the bound state are equal, the scattering length diverges. Since the magnetic moments of the two states are different in general, one can control the difference between their energies applying a static magnetic field B . The typical form of the scattering length around a Feshbach resonance is [77]

$$a = a_{bg} \left(1 - \frac{\Delta}{B - B_0} \right), \quad (4.7)$$

where B_0 is the position of the resonance, Δ its width and a_{bg} is the background scattering length, away from the resonance.

Dy shares with the other lanthanides a rich spectrum of Feshbach resonances, which allow fine-tuning of the interactions. In our experiment, we work in a magnetic field region around 5.1 G, where the scattering length is mainly determined by two Feshbach resonances, shown in Fig. (4.4) [19,80]. The overall systematic uncertainty on the value of a is $3a_0$, which corresponds to an uncertainty on ϵ_{dd} of about 4 %. The main contribution to the uncertainty comes from the value of the background scattering length, which is $a_{bg} = 140(7) a_0$ [80]. In the experimental procedure, the BEC is formed with a close to the background value a_{bg} , where contact interactions dominate over dipolar ones. Then, a magnetic field ramp lasting 70 ms tunes the scattering length at $114 a_0$, near to the BEC-supersolid transition, located at $a \sim 92 a_0$, i.e. $\epsilon_{dd} \sim 1.42$. A second ramp lasting 30 ms brings the system in the supersolid

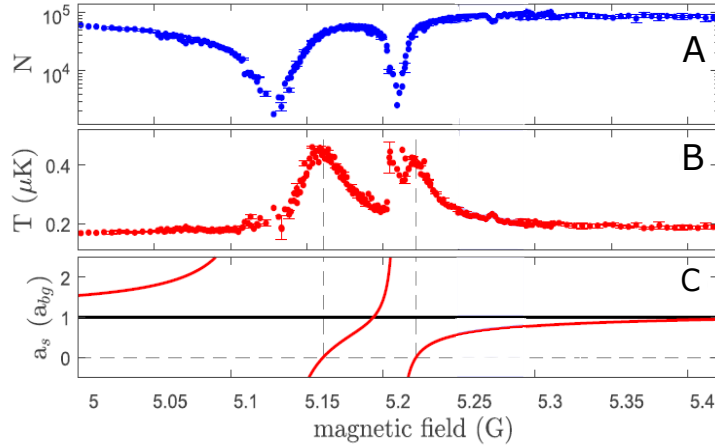


Figure 4.4: Feshbach resonances of ^{162}Dy around $B = 5.1$ G, from [80]. (A-B) Measurement of the resonances through atom number and temperature after a forced evaporation process. At the lowest atom number, the scattering length has its largest value, which induces atom losses. The temperature peaks reveal the points in which $a = 0$, where evaporation is ineffective. (C) Scattering length a as a function of the magnetic field B . Two resonances dominate the behavior of a : the first has $B_0 = 5.126(1)$ G and $\Delta = 35(1)$ mG, the second $B_0 = 5.209(1)$ G and $\Delta = 12(1)$ mG.

regime. The experimental signature of the supersolid transition is the formation of an interference pattern after a free expansion of the cloud (see Fig. 3.9). The interference is the result of the overlap of the coherent matter waves which form, in the trap, the droplets of the supersolid. The onset of the transition can be tracked using simple phenomenological observables that quantify the difference between the observed distribution and that of the BEC. For example, in Fig. 4.5, the mean squared deviation from a Gaussian distribution is employed. In the next section we discuss how to perform another type of analysis, based on a double-slit model. The phase diagram of the system depends on the type of trap: the previously stated values refer to the trap used in our scissors experiment, see chapter 5. Moreover, as pointed out in [19] and also by the simple model of chapter 3, the phase diagram depends also on the number of atoms N . For a given scattering length, if N is too low, one observes a BEC instead of a supersolid. As an example, we report in Fig. 4.5 the phase diagram in the $N - a$ plane observed in [19].

4.3 Imaging and fitting

The information on the atomic sample is obtained switching off all the traps and performing absorption imaging after a free expansion of the cloud. To minimize the effects of the dipolar interaction in the expansion, 200 μs before the release of the atoms from the trapping potential the scattering length is set at $a = 140 a_0$. The absorption imaging is performed with the blue light at 421 nm: the light is

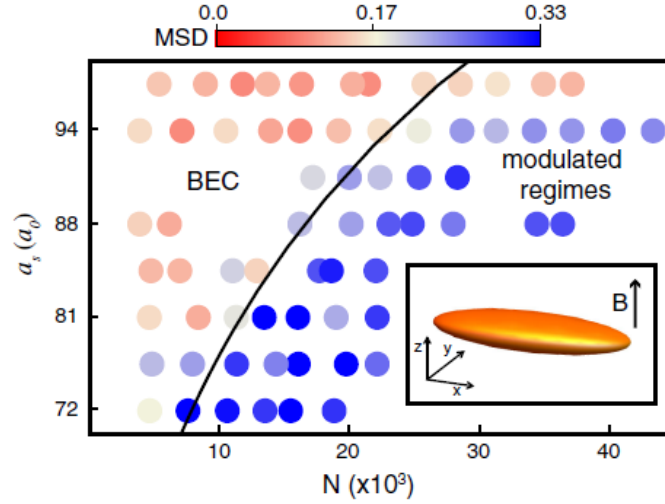


Figure 4.5: Phase diagram in the plane scattering length a versus atom number N from [19]. The colors indicate the mean squared deviation (MSD) of the distribution from a Gaussian, which is employed to quantify the difference between the BEC and the supersolid. For a given scattering length, there is a critical atom number under which the supersolid doesn't form. The inset shows the trap geometry.

absorbed by the atoms and the resulting "shadow" is recorded on a digital camera. Each image is a column density, i.e. a density integrated along the direction of the imaging beam. For example, an image taken in the xy plane with a laser beam propagating in the z direction is a matrix with a value for each pixel in the plane, and it is written as $Img(x, y)$. The imaging procedure is destructive, so a single image is taken for each experimental cycle, which is a composition of three different acquisitions. The first one, Img_1 , is taken with both atoms and lasers; the second one, Img_2 , is taken without the atoms, with only the lasers light. Finally, a third image, Img_3 , is taken with the lasers switched off, to isolate the background light from the room. The final image of the atoms, without the background components, is obtained as

$$Img = -\ln \left(\frac{Img_1 - Img_3}{Img_1 - Img_2} \right). \quad (4.8)$$

We interpret the recorded distribution as a momentum space density $n(k_x, k_y)$. This is valid to a good approximation if we can neglect the initial dimensions of the cloud and if the expansion is free, so that the energy in the trap is transformed in kinetic energy. If we could neglect the interaction energy in the trap, the observed momentum distribution would simply be the Fourier transform of the in-situ density distribution. However this is not our case since, in the trap, both contact and dipolar energies are larger than the kinetic energy. As a matter of fact, there is no model which can relate the observed momentum distribution to the in-situ density distribution so far. Our imaging system has a resolution in momentum space of $0.2 \mu\text{m}^{-1}$ ($1/e$ Gaussian width) [19]. Typical images of both the BEC and the supersolid are shown in Fig. 4.7. To obtain physical information from the images we perform

a fit, which is different in the BEC and supersolid regime. We can perform both 2D or 1D fits, integrating the density in one direction. For the 1D case, the BEC is fitted with a simple gaussian

$$n_{BEC}(k_x) = A e^{-\frac{(k_x - k_0)^2}{2\sigma_x^2}}. \quad (4.9)$$

For example, in the experiment on Goldstone modes [22], the axial breathing mode was revealed as an oscillation of the parameter σ_x . The BEC distribution in momentum space should be a Thomas-Fermi distribution, i.e. an inverted parabola, but the finite resolution of our imaging system makes it appear more similar to a Gaussian. On the other hand, the density distribution of the supersolid shows the two characteristic lateral peaks, which come from the interference of the in-situ droplets after the free expansion. To fit such a distribution, we find that a double slit model works well [19]. In the diffraction of light from a double slit, the intensity recorded on a screen at distance L from the slits, as a function of the distance x along the screen is

$$I(x) = I_0 \frac{\sin^2\left(\frac{\pi dx}{\lambda L}\right)}{\left(\frac{\pi dx}{\lambda L}\right)^2} \cos^2\left(\frac{\pi D x}{\lambda L}\right), \quad (4.10)$$

where d is the dimension of the single slit, D the distance between the slits and λ the light wavelength. The first term is the diffraction pattern from the single slit, while the second term is the interference between the two sources. The cardinal sine function of eq. (4.10) describes the diffraction from a rectangular slit, but in our analogy, the role of the slits is played by the atomic droplets, which don't have sharp edges. Instead of the cardinal sine, we therefore use a gaussian. Moreover, we add a second gaussian with different amplitude but the same width as the first one, to take into account the limited contrast of the interference. Finally, we add a phase ϕ in the interference pattern, which is needed if the droplets have different phases or, in other words, if the modulation develops with a non-zero velocity. The fitting function is

$$n_{ss}(k_x) = A_1 e^{-\frac{(k_x - k_0)^2}{2\sigma_x^2}} \left[1 + A_2 \cos^2\left(\frac{\pi}{k_{rot}}(k_x - k_0) + \phi\right) \right], \quad (4.11)$$

depicted in Fig. 4.6. The distance between two peaks is the rotonic momentum k_{rot} , which depends on the trap geometry and the number of atoms. Assuming the absence of perturbing effects of the interactions during the expansion, it reflects the in-situ distance between the droplets, which is given by $d = 2\pi/k_{rot}$. Typical numbers are $k_{rot} \sim 1.2 - 1.4 \mu\text{m}^{-1}$ and $d \sim 4.5 - 5 \mu\text{m}$ depending on the experimental conditions.

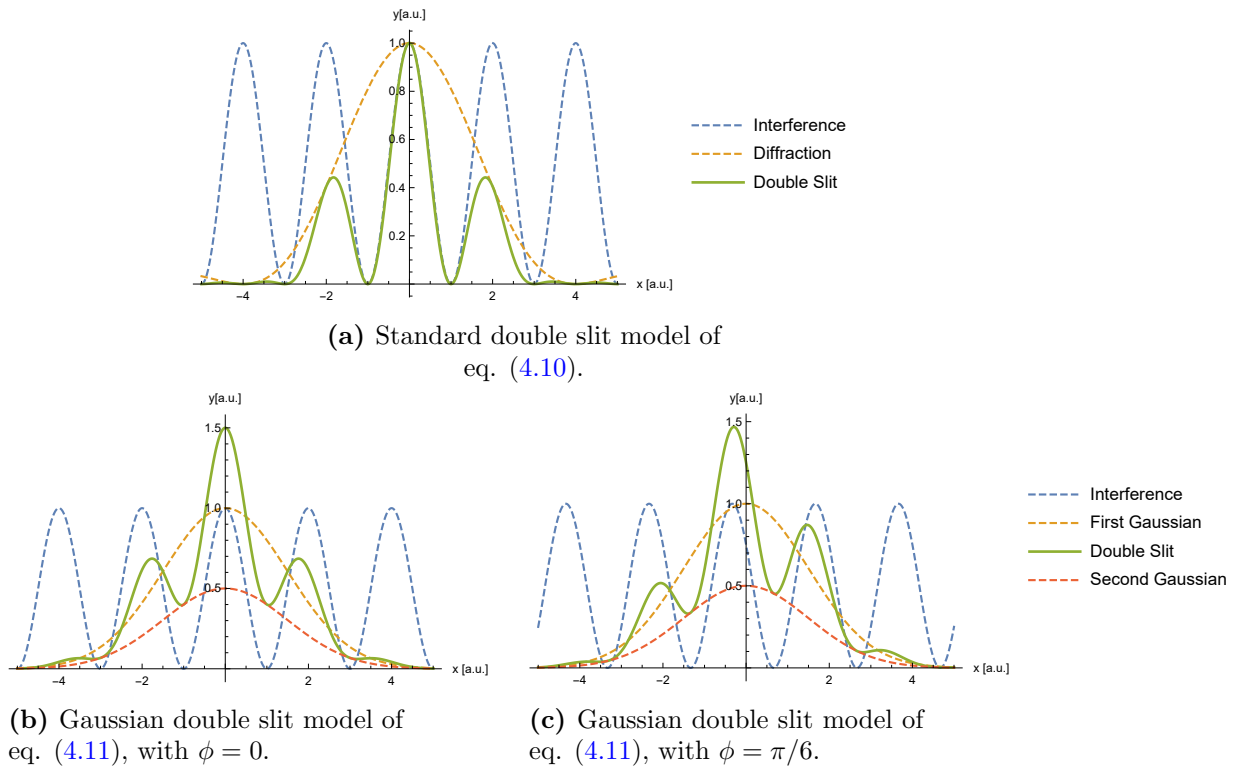


Figure 4.6: Different models for the fitting function of the supersolid density distribution.

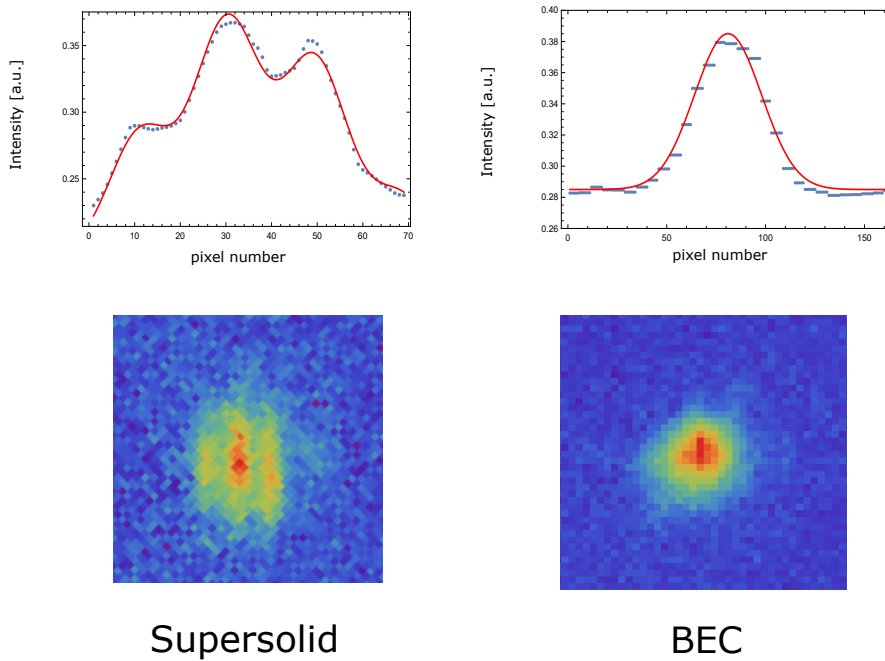


Figure 4.7: Experimental images of the supersolid ($\epsilon_{dd} = 1.45$) and BEC ($\epsilon_{dd} = 1.42$) in time of flight, and corresponding fits of the one-dimensional density distribution with the functions explained in the text.

Chapter 5

NCRI in a Dipolar Supersolid

In this chapter, we present the experimental study of the superfluid nature of the supersolid state of matter, performed through a rotational experiment, which is the central result of the thesis. The moment of inertia of a body quantifies its response to a rotational field. If a rotation of angular velocity Ω is induced around the z axis, the moment of inertia is defined as

$$\Theta = \frac{\langle J_z \rangle}{\Omega}, \quad (5.1)$$

where $\langle J_z \rangle$ is the angular momentum induced by the rotation. The operation $\langle \rangle$ indicates an average on the density distribution. For a fixed Ω , the larger is the angular momentum transferred to the body during the rotation, the larger its moment of inertia is. As discussed in chapter 1, the moment of inertia of a superfluid is quenched with respect to the classical rigid value, because of the irrotational motion which is forced by the locking of the phase of the order parameter. The moment of inertia is, therefore, a useful observable to study the superfluid properties of a system. As first proposed by Leggett, the supersolid phase of matter, being part of the class of the superfluid systems, should show new and interesting features when put under rotation, which are indicated as non-classical rotational inertia effects (NCRI) [9]. The study of the moment of inertia of the dipolar supersolid, therefore, appears as a necessary step in the understanding of this fascinating state of matter. This experimental study has been carried out in synergy with a theoretical investigation of the Trento theory group. The experimental results have been reported in a preprint [26].

5.1 Why the scissors mode?

To reproduce Leggett's ideal experiment, one should dispose of a supersolid confined in an annular trap, make the trap rotate and measure the supersolid moment of inertia. Our system is very different from what Leggett had in mind: we have three or four droplets, each composed by thousands of atoms, trapped in an anisotropic trap (see the simulation of the density distribution in Fig. 3.9). Because of the presence of the trap, our system is said to be inhomogeneous: the edges are different from the center. For the supersolid, this means that the density peaks at the center of

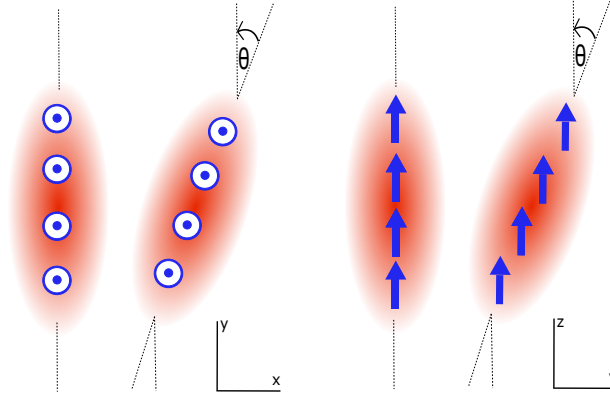


Figure 5.1: Scissors oscillations in different planes. On the left, the scissors oscillation in the xy plane, perpendicular to the dipoles orientation. On the right, the scissors oscillation in the zy plane, which contains the dipoles.

the trap are higher than those at the edges. To produce a homogeneous supersolid confined in an annulus, and therefore perform the exact analog of the Hess-Fairbank experiment, we should be able to produce a supersolid with many more droplets, of the order of 10, so with many more atoms.

Creating a supersolid with many droplets, also arranged in a two-dimensional configuration, involves the need for an improvement in the actual cooling and trapping techniques to increase by one or two orders of magnitude the actual number of atoms. Realizing such improvements will take timescales of the order of years. To understand some fundamental properties of the supersolid, however, we do not have to necessarily overcome such technical challenges. For what concerns the present experiment, i.e. the study of NCRI, we can rely on the scissors mode, which was discussed in Section 1.4. The scissors mode has been a successful tool to study the superfluid behavior of nuclei [43], and, more recently, of Bose-Einstein condensates [25, 44, 45]. The key feature of the scissors mode is that it provides a simple experimental way to measure the moment of inertia, whose quenching with respect to the rigid value is a hallmark of superfluidity. Our idea is, therefore, to study the scissors oscillation of the dipolar supersolid and from that extract the moment of inertia. In parallel to the present experimental work, a theoretical study has been performed by the Trento group [69], which confirms, through simulations of the eGPE, that the scissors mode can be used as a tool to measure the moment of inertia of the dipolar supersolid. We note that a peculiarity of our cold-atoms system, with respect to helium and to other condensed matter systems, is that we can directly compare, in the same experiment, a known superfluid phase of matter, the Bose-Einstein condensate, and the new supersolid. For this reason, we first discuss how the scissors mode is modified in a dipolar BEC.

A detailed study of the collective excitations of a dipolar condensate has been numerically performed in [75]. The theory relies on the GPE without the LHY

correction, so it predicts a mean field collapse before the supersolid transition. We recall that for a non-dipolar condensate the scissors frequency in the xy plane is $\omega_{sc} = \sqrt{\omega_x^2 + \omega_y^2}$. For oscillations in the other planes of the trap, the expressions are analog. For the dipolar BEC, we expect the dipolar interaction to modify the scissors oscillations: in particular, the results will depend on the plane in which the oscillation occurs, compared to the dipole orientation, which we take along the z axis (see Fig. 5.1). For the scissors mode in the xy plane, the dipolar interaction enters only as a geometrical factor: in fact, the torque exerted from the trap depends on the cloud's shape, which is deformed due to magnetostriction. This dependence enters the scissors frequency, which is found to be

$$\omega_{sc} = \sqrt{\frac{\alpha}{\beta}(\omega_x^2 + \omega_y^2)}. \quad (5.2)$$

The geometrical factors α and β are the deformations of the trap and the cloud, respectively, defined in eq. (1.36)-(1.41). In the case of a non-dipolar BEC, we recover the correct result since $\alpha = \beta$. The scissors frequency depends weakly on ϵ_{dd} through the parameter β . On the other hand, the scissors oscillations in the planes yz and xz are more affected by the dipolar interaction, which adds itself to the trap restoring force, as we can see from Fig. 5.1. In fact, when the cloud is tilted, the dipoles are, on average, more side-by-side compared to the initial position, which is an energetic more favorable configuration. As a result, the scissors frequencies depend directly on ϵ_{dd} and have more complicated forms, which can be found in [75]. We note that in this case the scissors mode can be excited also in a cylindrically symmetric trap since the restoring force is provided by the dipolar interaction itself, as observed for dipolar quantum droplets [81].

In our experiment, we excite the scissors mode in the xy plane, so we will confront with eq. (5.2), on the BEC side. Our choice is motivated by the fact that, with this configuration, the dipolar potential is rotationally invariant around the z axes, a prerequisite to link the scissors dynamics to the moment of inertia.

5.2 Measurement of the scissors mode

Here we describe the experimental techniques used to produce and study the scissors oscillation in both BEC and supersolid regimes: the optical trap, the excitation methods, and the fitting procedure. We then present and comment on the result for the scissors frequency through the supersolid transition.

Optical trap

Our system is a dipolar supersolid with typically $N \sim 10^4$ atoms of ^{162}Dy , with no detectable thermal fraction, trapped in an optical trap. To excite the scissors mode we need an anisotropic trap in the xy plane. As described in chapter 4, the experiment starts with the formation of a BEC via evaporative cooling in a trap built with two laser beams, called ODT1 and ODT3, which form an angle of 40° one with the other. The aspect ratio of this trap, used for the experiment on Goldstone

mode [22], is 1:3, given by the frequencies $(\omega_x, \omega_y, \omega_z) = 2\pi \times (18.5, 53, 81)$ Hz. We have seen in section 1.4 that a large anisotropy of the trap ensures the presence of a clear scissors oscillation: in the opposite limit of little anisotropy the scissors mode transforms in a quadrupole mode. However, for values of the anisotropy α close to 1, the superfluid component has lower influence in the rotation and the moment of inertia tends to the classical value, also if the system is completely superfluid, as we can see making the limit for α going to 1 in eq. (1.45). Since our goal is to distinguish between the superfluid behavior of the BEC and that of the supersolid, we can't use a too large anisotropy, which suppresses such a behavior. As a matter of fact, the aspect ratio of 1:3 results enough to hide the difference between BEC and supersolid under the experimental error. We, therefore, use a different trap, adding another laser beam to reach an aspect ratio of 1:2. The new beam is called ODT2 and form an angle of about 40° with the ODT1, and thus of 80° with the ODT3. This configuration allows us to lower the final aspect ratio (see Fig. 5.2). The BEC is still produced in the trap given by the sum of ODT1 and ODT3, and after a waiting time the ODT1 is turned off and the ODT2 turned on so that the system is confined in the final trap made with ODT2 and ODT3. We choose the powers of the beams to produce an aspect ratio of 1:2. The frequencies measured exciting a dipole mode are $(\omega_x, \omega_y, \omega_z) = 2\pi \times (23, 46, 90)$ Hz. These frequencies experience day-by-day variations of the order of a few percent, so they are measured before and after each oscillation experiment. The deformation parameter of the trap is $\alpha = 0.6$. Also with this new geometry, we observe a supersolid phase after a scattering length ramp towards values of a under about $92 a_0$.

Excitation methods

To excite the scissors mode we need to change the orientation of the trap's principal axis compared to the cloud's one. The ideal procedure would rigidly rotate the trap without changing its shape, i.e. maintaining the trap frequencies unaltered so that the coupling to other modes is negligible. In the experiment, we observe that, other than the scissors, the principle mode to be excited is the lowest axial breathing mode, the same studied in the experiment on Goldstone modes [22]. This mode is revealed as an oscillation of the x-width of the cloud and, as previously observed, it is naturally excited crossing the instability with the ramp in the scattering length. Its typical amplitude is 10 %, which is, therefore, the minimal amplitude that we can obtain. We have developed two excitation methods:

First Method The beam ODT1, used to capture atoms from the resonator, is switched off when the supersolid forms. Switching on again the ODT1 at low power, for 5 ms, changes the angle of the trap. The resulting scissors amplitude is about 0.3 rad so that the oscillation is clearly visible and allows for a good fitting procedure. From a simulation of the trap potential, using the known powers and waists, we see that this method changes also the trap frequencies of about 10 %. As a confirmation, in the experiment we see that the breathing mode is excited with amplitudes of more than 20 %.

Second method Since the two laser beams aren't perfectly perpendicular, chang-

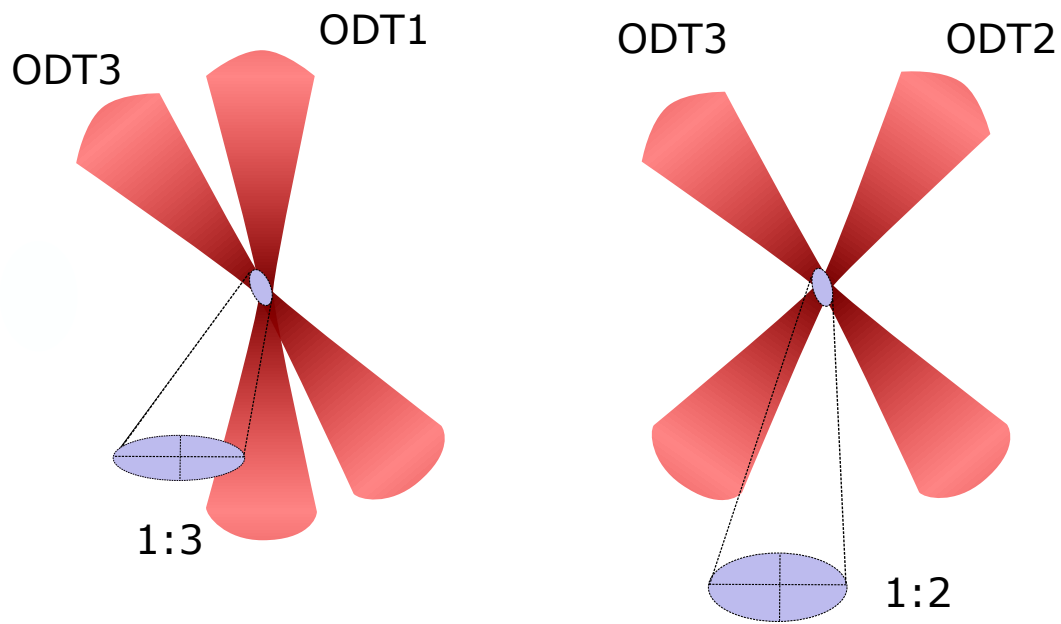


Figure 5.2: Two different optical traps. In the first case (left image), with ODT1 and ODT3 at an angle of 40° , the aspect ratio of the trap in the xy plane is 1:3, and the superfluid behavior for the BEC and the supersolid is indistinguishable. Therefore we add an other beam, ODT2, so that the final trap has an aspect ratio of 1:2 (right image).

ing the respective powers tilts the global trap orientation. The amplitude of the excitation can be regulated choosing the power variations of the beams. From the simulation we can see that this method changes the trap frequencies of only 3 %: indeed, the breathing mode is observed with an amplitude near to the minimum value of 10 %. On the other hand, also the scissors oscillation has a lower amplitude (about 50 mrad after time of flight) so that the precision with which we fit the frequency is lower.

Fitting procedure and results

Our observable is the density distribution obtained with absorption imaging after time of flight. Our goal is to extract the angle of the principal axes of the system (BEC or supersolid) after different oscillation times. We indicate with xy the reference frame of the cloud, which performs an angular oscillation $\theta(t)$ inside the trap, induced by one of the two methods previously described. On the other hand, the reference frame of the imaging camera is fixed, and it is indicated with a prime, $x'y'$ (see Fig. 5.3 A). The angle that we fit from the images is, therefore, the angle $\theta'(t)$ in the fixed reference frame. Note that the variable t is the oscillation time in-situ, which is varied during the experiment. The two angles θ and θ' could be related with a model of the free expansion, which lasts a fixed time $t_{exp} = 95$ ms. However, such a model is very challenging, for two reasons. First, the dipolar interaction complicates considerably the expansion dynamics, although just before the release from the trap the scattering length is increased to $a = 140a_0$, to limit the dipolar effects. Second, for a rotating condensate, the dynamic in time of flight is non-trivial, as observed in non-dipolar condensates [82, 83]. The basic ingredients needed to understand the phenomenon are the conservation of angular momentum and superfluid irrotational flow. When the condensate is released from the trap, it starts expanding in the short direction, but it can't reach a symmetric configuration with unity aspect ratio, because in that case angular momentum would be zero and the conservation law would be violated. When the aspect ratio approaches unity, therefore, the angular velocity rapidly increases until the condensate starts expanding in the other direction, so that the time evolution of the angle isn't linear, as in the case of the thermal gas. The crucial feature is that the frequency isn't affected by the expansion, the only effect being the enhancement of the scissors amplitude of a factor near 2 with respect to the in-situ oscillation. When we refer to the scissors amplitude, we intend the one after the free expansion.

Typical experimental images are reported in Fig. 5.3 (B)-(C). In the BEC regime, for $\epsilon_{dd} < 1.42$, we observe a Gaussian distribution tilted in the $k_{x'}k_{y'}$ plane of an angle θ' . To extract θ' , we use a two-dimensional fit with a rotated Gaussian

$$n(k_{x'}, k_{y'})_{BEC} = Ae^{-\mathbf{r}^T B \mathbf{r}}, \quad (5.3)$$

where

$$\mathbf{r} = \begin{pmatrix} k_{x'} - k_{x'0} \\ k_{y'} - k_{y'0} \end{pmatrix} \quad B = \begin{pmatrix} \frac{\cos^2 \theta'}{2\sigma_x^2} + \frac{\sin^2 \theta'}{2\sigma_y^2} & -\frac{\sin 2\theta'}{4\sigma_x^2} + \frac{\sin 2\theta'}{4\sigma_y^2} \\ -\frac{\sin 2\theta'}{4\sigma_x^2} + \frac{\sin 2\theta'}{4\sigma_y^2} & \frac{\sin^2 \theta'}{2\sigma_x^2} + \frac{\cos^2 \theta'}{2\sigma_y^2} \end{pmatrix}. \quad (5.4)$$

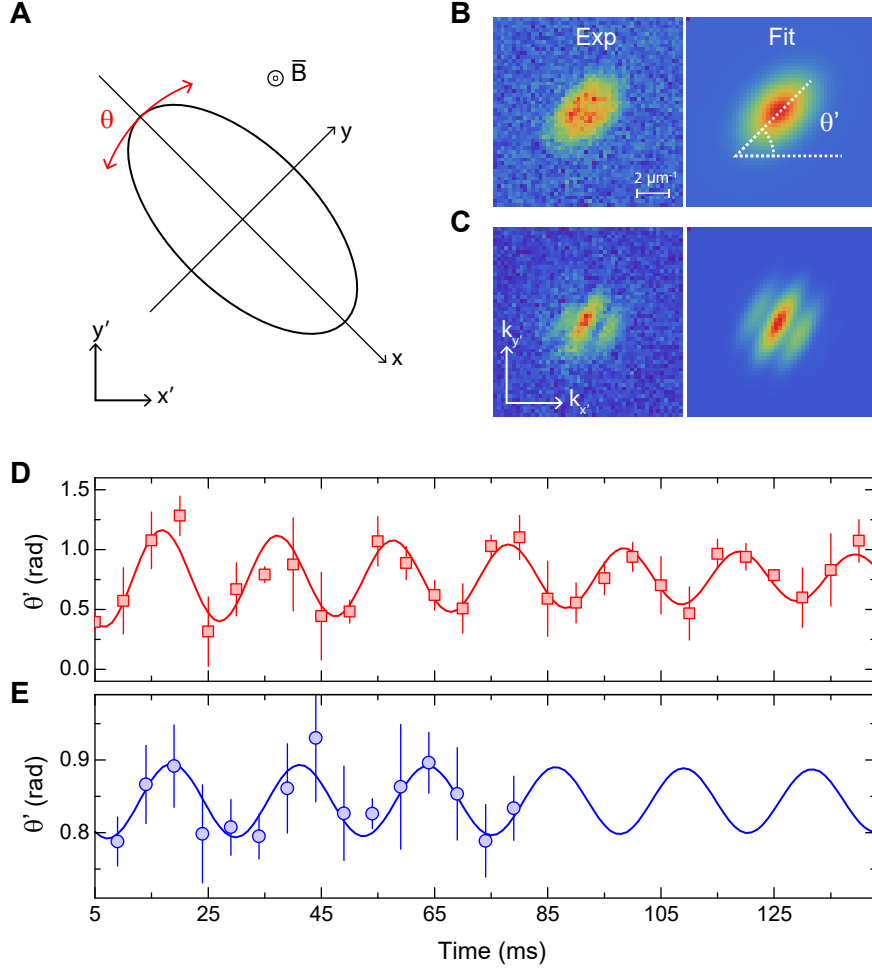


Figure 5.3: Experimental observation of the scissors mode. (A) Sketch of the atomic cloud, trapped in an anisotropic trap with eigenaxes along x and y . The scissors mode is excited through a sudden rotation of the trapping potential, resulting in an oscillation of the angle θ (red arrows). (B)-(C) Experimental images obtained after free expansion and corresponding two-dimensional fit functions used to extract the tilting angle θ' , for both BEC (B), $\epsilon_{dd} = 1.14$, and supersolid (C), $\epsilon_{dd} = 1.45$, regimes. (D)-(E) Time evolution of the angle θ' , in both BEC (D) and supersolid (E) regimes. The time evolution is fitted with a damped sinusoid to extract the scissors frequency. The small-amplitude oscillation in the supersolid regime with respect to the BEC one results from the different methods used to induce the excitation (see text). Error bars are one standard deviation from 4-8 measurements.

The point $(k_{x'0}, k_{y'0})$ is the center of the Gaussian, and σ_x and σ_y its widths. The symbol T indicates the transpose operation. In the supersolid regime, for $\epsilon_{dd} > 1.42$, the droplets produce an interference pattern whose principal axis (corresponding to the in-situ long axis, along which the droplets form) is tilted of an angle θ' . Here we use the rotated double slit model as the fit function

$$n(k_{x'}, k_{y'})_{SS} = n(k_{x'}, k_{y'})_{BEC} \left[1 + C \cos^2 \left(\frac{k_{x'} \cos \theta' - k_{y'} \sin \theta'}{k_{rot}} \pi + \phi \right) \right]. \quad (5.5)$$

The relevant parameters are the angle θ' and the x-width σ_x , whose oscillation is the breathing mode. The typical peak spacing is $k_{rot} = 1.4 \mu\text{m}^{-1}$, from which we deduce the presence of a single row of droplets in the trap, separated by a typical spacing $d = 4.5 \mu\text{m}$. Repeating the fitting procedure at different times t , we obtain the time evolution of the parameters. The presence of the scissors mode is clear from Fig. 5.3 (D)-(E), where we see the sinusoidal oscillation of the angle θ' . Both BEC and supersolid oscillate at a single frequency, which is extracted with a fit of a damped sinusoid with the form

$$\theta'(t) = \theta'_0 + A_s \cos \left(\sqrt{\omega_{sc}^2 + \tau^{-2}} t + \phi \right) e^{-t/\tau}, \quad (5.6)$$

where A_s is the amplitude of the scissors oscillation, ω_{sc} its frequency and τ the damping time. A similar fit is performed also for σ_x , yielding the amplitude A_b and frequency ω_b of the breathing mode.

As previously explained, the presence of the breathing mode is inevitable and it has different effects on the measurement depending on which phase of our system we probe (see Fig. 5.4). In the BEC phase, scissors and breathing mode are normal modes, so that they do not influence one another also if their amplitudes are quite large [75]. For the BEC we can hence use the excitation method which consists of the sudden switch of the ODT1 so that the amplitude of the scissors oscillation is about 0.3 rad (see Fig. 5.3 (D)). Although the relative amplitude of the breathing mode is about 20 %, we measure a value of ω_{sc} in agreement with the hydrodynamic calculations, eq. (5.2), confirming that the two modes don't mix, as it is depicted in Fig. (5.4). On the other hand, we observe that in the supersolid phase such a large excitation produces a scissors frequency similar to the BEC's one, hiding the peculiar supersolid behavior. A similar effect has been previously observed during the study of the bifurcation of the breathing mode [22]: in that case, the large excitation amplitudes destroyed the two-frequencies oscillations of the x-width, producing an oscillation with a frequency near to the BEC's value. The measurement was finally performed using different observables (see section 3.4). We can think of this mixing phenomenon as the result of a temporal average over the supersolid density, which, in the presence of a large breathing mode, tends to average out the density modulation, leading the system to a BEC-type behavior. As a result, to measure the scissors frequency of the supersolid, we need to reduce to the minimum value the breathing excitation. We, therefore, rely on the second excitation method, consisting of a temporary change of the power of the two trapping beams. With this method, we observe the minimum breathing amplitude of 10 % and a scissors

amplitude of about 50 mrad. Such a small amplitude limits the precision with which we fit the angle θ' from the images, and consequently introduce a larger error in the scissors frequency. We note that the precision in the supersolid phase is also reduced by the low lifetime of the sample (about 100 ms), with respect to the BEC, as we can see from Fig. 5.3 (D). A possible improvement in this sense could be to use the isotope ^{164}Dy , which has a lifetime of the order of 200 ms, as proved by the Innsbruck group [20].

The results for the scissors frequency as a function of the parameter ϵ_{dd} are reported in Fig. 5.5, compared to the theoretical predictions of the Trento group [69]. On the left side, in the BEC regime, we observe a frequency in good agreement with the known results [75], with a slow negative slope arising from the dependence of the cloud deformation β on ϵ_{dd} , due to magnetostriction. Crossing the supersolid transition we observe a clear reduction in the scissors frequency, in agreement with the theory, which points out the occurred quantum phase transition. Our uncertainty in ϵ_{dd} prevents us from zooming near the transition point, testing which is the order of the transition, an issue on which there is no agreement at the moment. A first order phase transition, indeed, would imply a discontinuous jump in the frequency, as it seems to be the case from the simulations [69]. The first order nature of the transition is also suggested by the experimental fact that the axial breathing mode is spontaneously excited crossing the transition, despite the efforts to induce an adiabatic process. This could be interpreted as a consequence of the release of latent heat, the hallmark of first order phase transitions. Increasing ϵ_{dd} the frequency decreases even more until we reach the droplet crystal regime, which we can't explore in this experiment for two reasons. First, the lifetime severely decreases because of the increase in density inside the droplets, which favors three-body losses. The lifetime is of the order of one oscillation period, making very difficult the measurement of a frequency. Second, since the droplets have no phase coherence one with the other, the interference pattern observed in time of flight is more complicated and doesn't present a clear principal axis as in the supersolid. The extraction of a tilting angle from the images is, therefore, very challenging.

5.3 Moment of inertia and superfluid fraction

With the measured scissors frequencies we can obtain the moment of inertia through the formula explained in section 1.4, eq. (1.45), that we report here for clarity:

$$\Theta = \Theta_c \alpha \beta \frac{(\omega_y^2 + \omega_x^2)}{\omega_{sc}^2}. \quad (5.7)$$

The trap frequencies, and then also the parameter α , are measured before and after each oscillation experiment. On the other hand, we don't have direct experimental access to the cloud deformation β , for two reasons. First, we do not observe the system in-situ, but after a free expansion, so that we do not know the exact density distribution $\rho(x, y)$ of the cloud in the trap. To perform such in-situ imaging, we would need a resolution of the order of the radius of the droplets, hence smaller than 1 μm , which is not available in the laboratory so far. Second, a theoretical

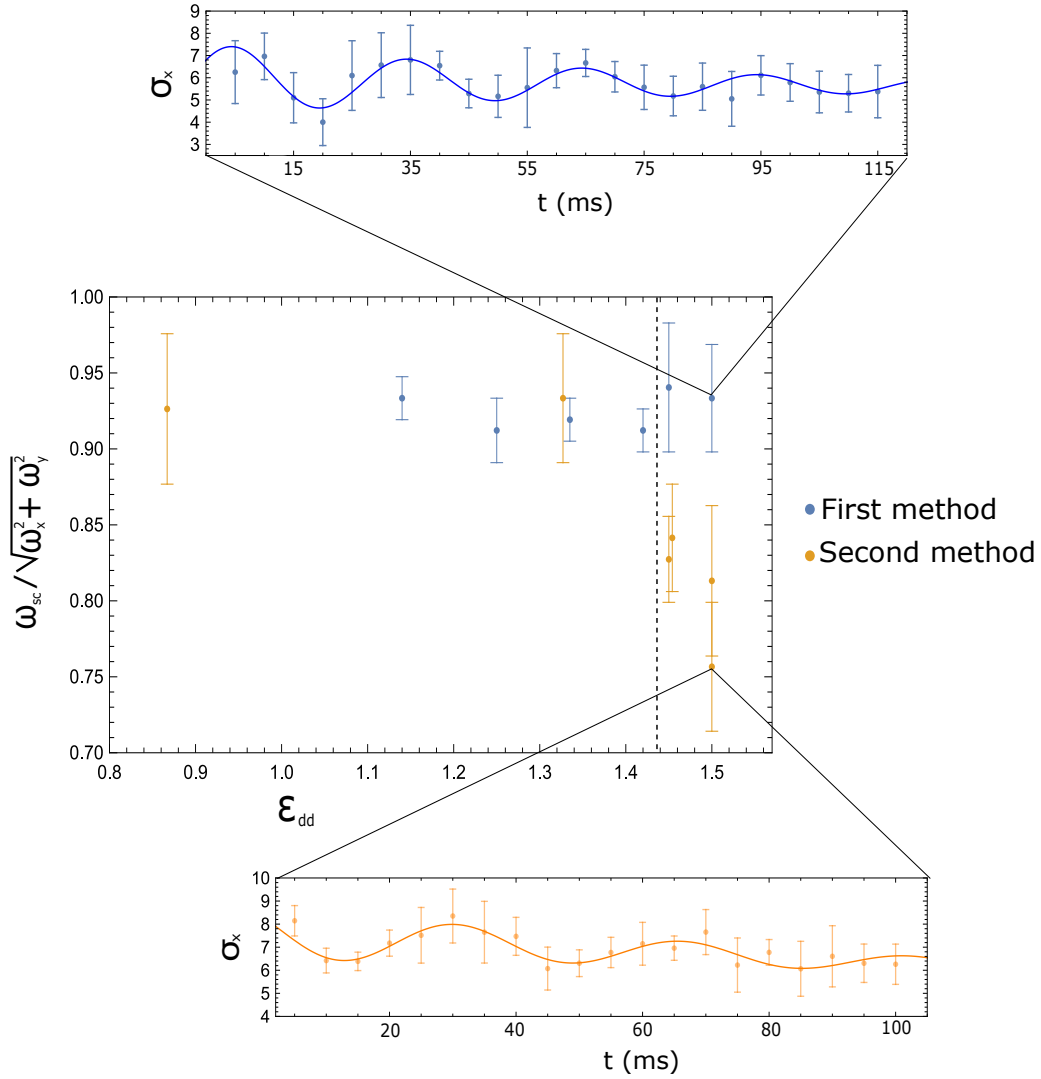


Figure 5.4: Scissors frequencies with different excitation methods. The data in blue are obtained exciting the scissors mode with the sudden switch-on of the ODT1 (first method), while the ones in yellow are obtained changing the powers of the ODT2 and ODT3 (second method). On the BEC side, at the left of the vertical dashed line, the scissors frequencies are unaffected by the type of excitation method. Since the scissors amplitude is lower with the second method, the error bars on the respective scissors frequencies are larger. On the supersolid side, the two methods give different results: a too large excitation shifts the scissors frequency towards the BEC value. We interpret such a shift as an effect of the axial breathing mode which is excited with the scissors. In the insets, we show the oscillations of the x -widths σ_x for two supersolids point. With the first method, the breathing oscillation has an amplitude of about 25 %, while with the second method the amplitude is 11 %, of the order of the minimum reachable amplitude.

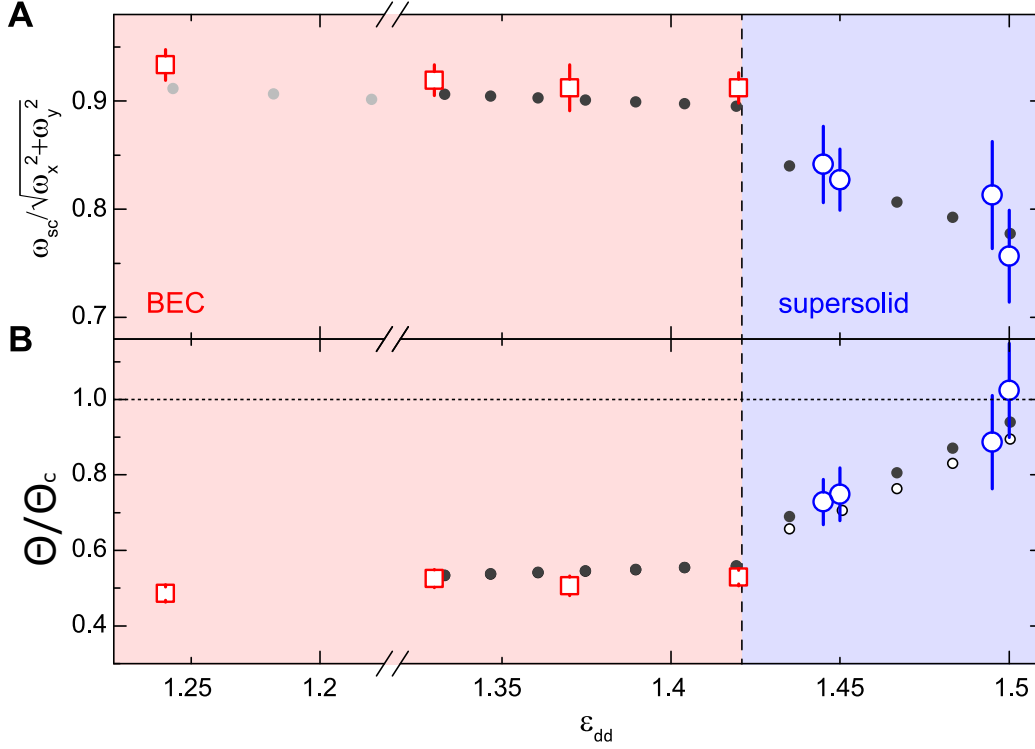


Figure 5.5: Scissors frequencies and moment of inertia as a function of ϵ_{dd} . (A) Scissors frequencies normalized to the non-dipolar value $\sqrt{\omega_x^2 + \omega_y^2}$. Large squares and circles are experimental measurements, while black dots are numerical simulations of the eGPE from [69]. The most remarkable result is the clear reduction of the scissors frequency from the BEC to the supersolid side. Gray dots are theoretical predictions for the dipolar BEC at the mean-field level, from [75]. For greater values of ϵ_{dd} , they predict the collapse of the cloud. (B) Moment of inertia calculated from eq. (5.7), using experimental (large squares and circles) and theoretical (black dots) data. The decrease of the scissors frequency translates to the increase of the moment of inertia. The horizontal dashed line represents the classical moment of inertia. Small open circles are the numerical predictions for a completely superfluid system with the density distribution of the supersolid [69]. The pairs of experimental datapoints in the supersolid regime, at $\epsilon_{dd} = 1.45$ and $\epsilon_{dd} = 1.50$ are displaced horizontally for clarity.

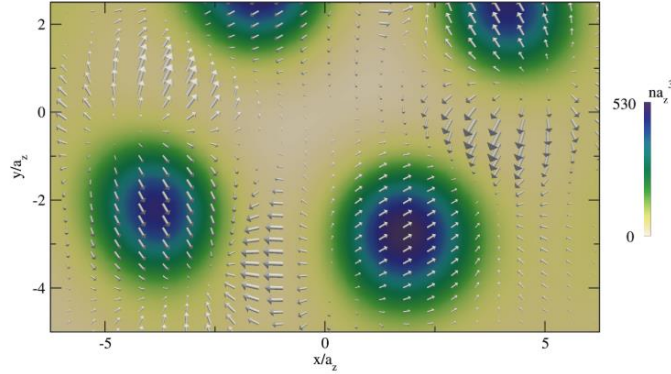


Figure 5.6: Velocity field of a supersolid under rotation, from [69]. The colors indicate the density. The oscillator length in the z direction is indicated with a_z .

model for the expansion of the gas doesn't exist, so we can't extract the density distribution $\rho(x, y)$ from our observable in momentum space $n(k_{x'}, k_{y'})$. To obtain the moment of inertia we, therefore, rely on the theoretical values from [69].

The results for the moment of inertia are reported in Fig. 5.5 (B). For the dipolar BEC, we obtain a result which is perfectly consistent with the theory of ordinary superfluids, the moment of inertia being $\Theta = \beta^2 \Theta_c$, as it is derived from the hydrodynamic equations. For our trap configuration, we obtain a moment of inertia which is about half of the classical value. The moment of inertia slowly increases with ϵ_{dd} because of the change in β . After the supersolid transition, at $\epsilon_{dd} = 1.45$, Θ definitely increases, being however smaller than the classical value. This result demonstrates NCRI for the dipolar supersolid, and therefore constitutes a direct proof of superfluidity, coming from a rotational experiment, for the new supersolid state of matter. For the next point at $\epsilon_{dd} = 1.50$, approaching the droplet crystal regime, the moment of inertia is indistinguishable from the classical value under the experimental error.

As a comparison with Leggett's argument discussed in Section 1.2, it is interesting to have a look at the simulated velocity field of the supersolid under rotation (Fig. 5.6). The simulation, performed in [69], considered a cylindrical trap, rotated at small angular velocities, with a high number of atoms ($N \sim 10^5$) which form droplets in a triangular lattice. The scissors velocity is modified so that the density maxima start rotating in a rigid way around the center of the trap, increasing the moment of inertia. The regions with low density move in the opposite direction so that the velocity stays irrotational. This behavior is clearly analog to the one-dimensional Leggett model, see for example Fig. 1.4.

We note that the increase of the moment of inertia in the supersolid is in principle due to two reasons. The first, main one, is the change in the shape of the system, which develops the lattice structure typical of supersolids, determining a change of

the parameter β . The second reason is the reduction of the superfluid fraction, also due to the formation of the lattice, but which accounts for the tunnelling properties of the atoms in a non-uniform landscape, as pointed out by Leggett's argument. To extract information about the change in superfluid fraction, one could compare the measured moment of inertia with the one of a hypothetically completely superfluid system, with the same density distribution of the supersolid, i.e. with $\Theta = \beta^2 \Theta_c$, where β is calculated for the supersolid. This is done in Fig. 5.5 (B), where the completely superfluid values, numerically calculated in [69], are depicted with little open dots. Although the nominal values of our measurements are slightly above the completely superfluid points, suggesting a superfluid fraction less than one, our uncertainty prevents us from distinguishing between the two scenarios. For a more direct comparison, we define a superfluid fraction in analogy with Leggett's one, i.e. $\Theta = (1 - f_s) \Theta_c$, which is valid for a cylindrically symmetric system. In our anisotropic case, we know that a completely superfluid system (such as the BEC) has a moment of inertia proportional to β^2 . We therefore propose the following definition of superfluid fraction

$$\Theta = (1 - f_s) \Theta_c + f_s \beta^2 \Theta_c. \quad (5.8)$$

We see that we recover the correct results in the limits $f_s = 1$ and $f_s = 0$. Combining eq. (5.8) and (5.7), we obtain a formula which gives the superfluid fraction in terms of the measured scissors frequency

$$f_s = \frac{1 - \alpha\beta(\omega_x^2 + \omega_y^2)/\omega_{sc}^2}{1 - \beta^2}. \quad (5.9)$$

In Fig. (5.7) we plot the superfluid fraction calculated with the previous formula, using the experimental scissors frequencies. On the BEC side, f_s is always consistent with 1, i.e. with a fully superfluid system. The points in the supersolid regime are consistent with 1, although the nominal values are 0.85 and 0.92, reflecting the previous discussion on the moment of inertia. It is remarkable that the dipolar supersolid has a superfluid fraction so close to unity, especially if compared with the helium estimates of 0.01 [11]. Such a large superfluid fraction derives from the cluster characteristics of the dipolar supersolid, which make it more naturally superfluid than the hypothetical helium supersolid.

We have seen in section 1.2 the upper bound to the superfluid fraction derived by Leggett in his seminal paper [9], in which he first proposed the idea of NCRI for a supersolid :

$$f_s \leq \left(\frac{1}{\lambda} \int_0^\lambda \frac{dx}{\rho(x)/\bar{\rho}} \right)^{-1}, \quad (5.10)$$

where λ is the dimension of the supersolid unit cell and $\bar{\rho}$ is the averaged density. As we have discussed at the beginning of the chapter, our system is very different from Leggett's one in many aspects. First, our supersolid is inhomogeneous, in the sense that the trap modifies the density distribution (see the inset in Fig. 5.7), which doesn't possess a perfect discrete translational symmetry. Second, the system isn't confined in an annular geometry: the scissors oscillation happens in the

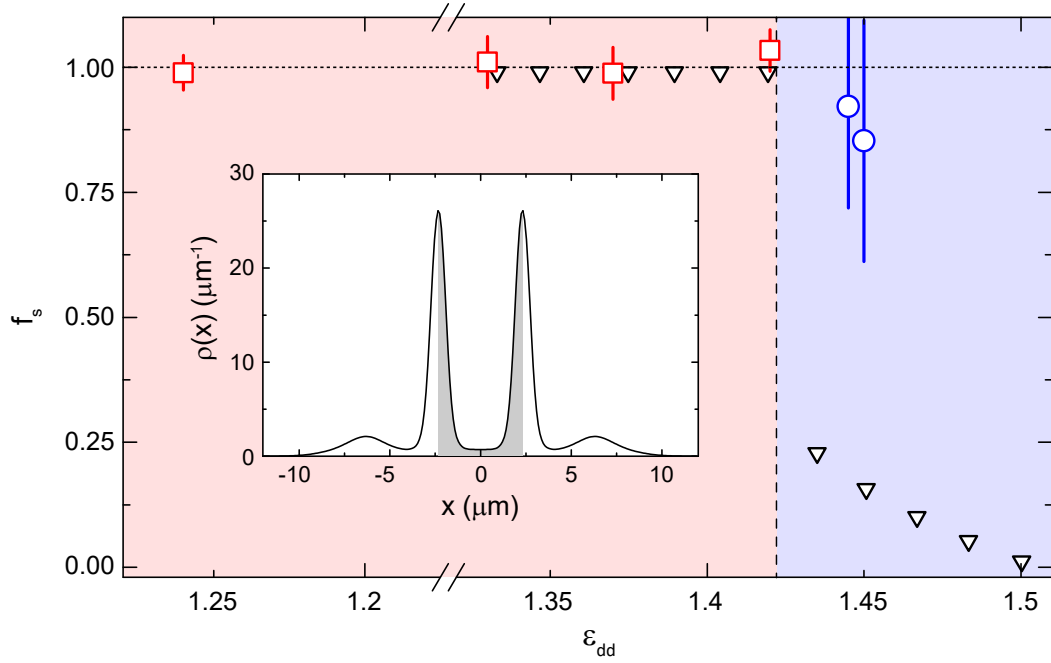


Figure 5.7: Superfluid fraction across the supersolid transition. Large squares and circles are the superfluid fraction from the measured scissors frequencies, from eq. (5.9). Open triangles are the prediction of Leggett’s argument, eq. (5.10), obtained from the numerically calculated density distribution [69]. In the inset: example of the density distribution for $\epsilon_{dd} = 1.45$. The gray region is the region of integration for eq. (5.10).

whole xy plane. We could, therefore, rely on some two-dimensional extensions of Leggett's upper bound [84], but in this case, we would face the problem that our system is smaller than the unit cell of a two-dimensional supersolid. Finally, the one-dimensional approach of Leggett doesn't account for the superfluidity of the single droplet, which we expect to be significant towards the droplet crystal regime, where the absence of overlap between droplets automatically gives $f_s = 0$ in eq. (5.10). Given all these caveats, we think that it is anyway interesting to apply Leggett's formula to our system, keeping in mind that we can't expect a quantitative agreement with our data. Our idea is that eq. (5.10) quantifies the superfluid fraction in terms of the density minima that appear between one maximum and the other, as opposed to a completely superfluid system. Therefore, in our system the superfluid fraction should be dominated by the minimum appearing in the x direction. Moreover, we are interested in a comparison with Leggett for historical reasons: his first estimate for the superfluid fraction in helium was of the order of 10^{-4} [9], in agreement with current experimental bounds and in strong disagreement with the first observations of order 0.01 [11].

Since we do not have access to the density $\rho(x)$, we rely on the numerical profile from [69]. The 1D density $\rho(x)$ is obtained integrating the 3D density $\rho(x, y, z)$ in the y, z directions. The averaged density $\bar{\rho}$ appearing in eq. (5.10) is defined as $\bar{\rho} = 1/d \int_0^d \rho(x) dx$, where d is an interval containing an integer number of unit cells. Due to inhomogeneities, both in the BEC and in the supersolid the density goes to zero at the edges of the system, where the trap potential increases. We need to exclude such regions, since they would artificially lower the superfluid fraction, also for the BEC. Since we want to quantify the effect of the formation of a minimum at the center of the trap, we integrate into the region between the two principal maxima, which we identify as our unit cell (see Fig. 5.8). The same interval is used for the BEC so that we can directly compare the supersolid with a known system. We choose to calculate the mean density $\bar{\rho}$ using the same interval, i.e. with $\lambda = d$, so that we completely ignore any effects from inhomogeneity.

The results of the calculation are shown in Fig. 5.7, together with the experimental points. For the BEC the superfluid fraction is 1 at each point since in our interval the density is quite constant. Once that the density modulation is formed, the superfluid fraction goes down to 0.25. In correspondence to our data, we obtain $f_s = 0.15$. As already specified, we didn't expect a quantitative agreement with our measurements. However, we think that it is a remarkable result the fact that, although developed for a "helium-like" supersolid, and not for a cluster supersolid like the dipolar one, the Leggett's argument predicts a large superfluid fraction, in better agreement with our data than it was with the first helium experiments.

5.4 Thermal Measurements

We have performed some measurements of the scissors oscillation as a function of the temperature, to verify that our system is in the so-called collisionless regime. As explained in Section 1.4, in the opposite hydrodynamic regime, a classical sys-

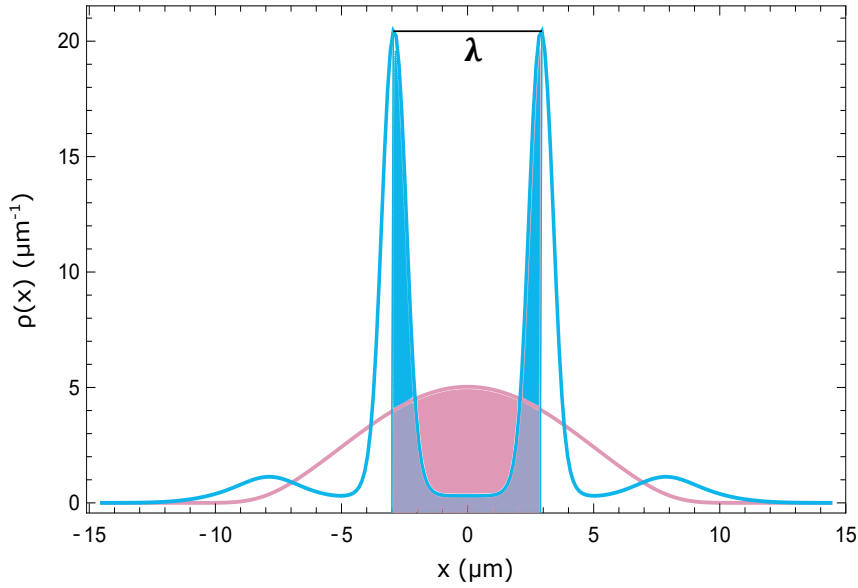


Figure 5.8: Comparison between the density profiles of the supersolid ($\epsilon_{dd} = 1.45$) in blue, and the BEC ($\epsilon_{dd} = 1.30$) in light red. The filled area represents the region of integration for eq. (5.10), in which the BEC is quite constant while the supersolid develops its principal minimum.

tem would produce the same results as a superfluid one. This is the reason why, in some strongly interacting systems such as the Fermi gas across the BEC-BCS crossover [85], the scissors oscillation can't be used as a demonstration of superfluidity.

The critical temperature for condensation in our system is $T_c \approx 60$ nK, for typical atom number. The lowest detectable temperature is about $0.6 T_c \approx 35$ nK, which corresponds to the lowest detectable thermal fraction of about 25 %. The temperature is changed by varying the time at which the evaporative cooling is stopped. For $T < T_c$, the scissors frequency is measured only for the BEC, while the temperature is measured independently with a fit on the thermal cloud, with a shorter expansion time of 25 ms, so that it is not too dilute to be detected. For $T > T_c$ we make a measurement on the thermal cloud, with an expansion time of 4 ms. The results are summarized in Fig. 5.9. For the BEC we observe a single frequency at every temperature, and a slight negative shift for $T > 0.7 T_c$, which comes from the interaction with the thermal component. For the thermal cloud, the result drastically changes: we observe two distinct frequencies, near to the expected values of $\omega_{\pm} = |\omega_x \pm \omega_y|$ [42]. The two-frequency oscillation of the thermal cloud demonstrates that our system is in the collisionless regime and that the dynamics observed for the condensate is a consequence of superfluidity. Our observations are perfectly coherent with the results for non-dipolar BEC (see Fig. 1.11 in section 1.4).

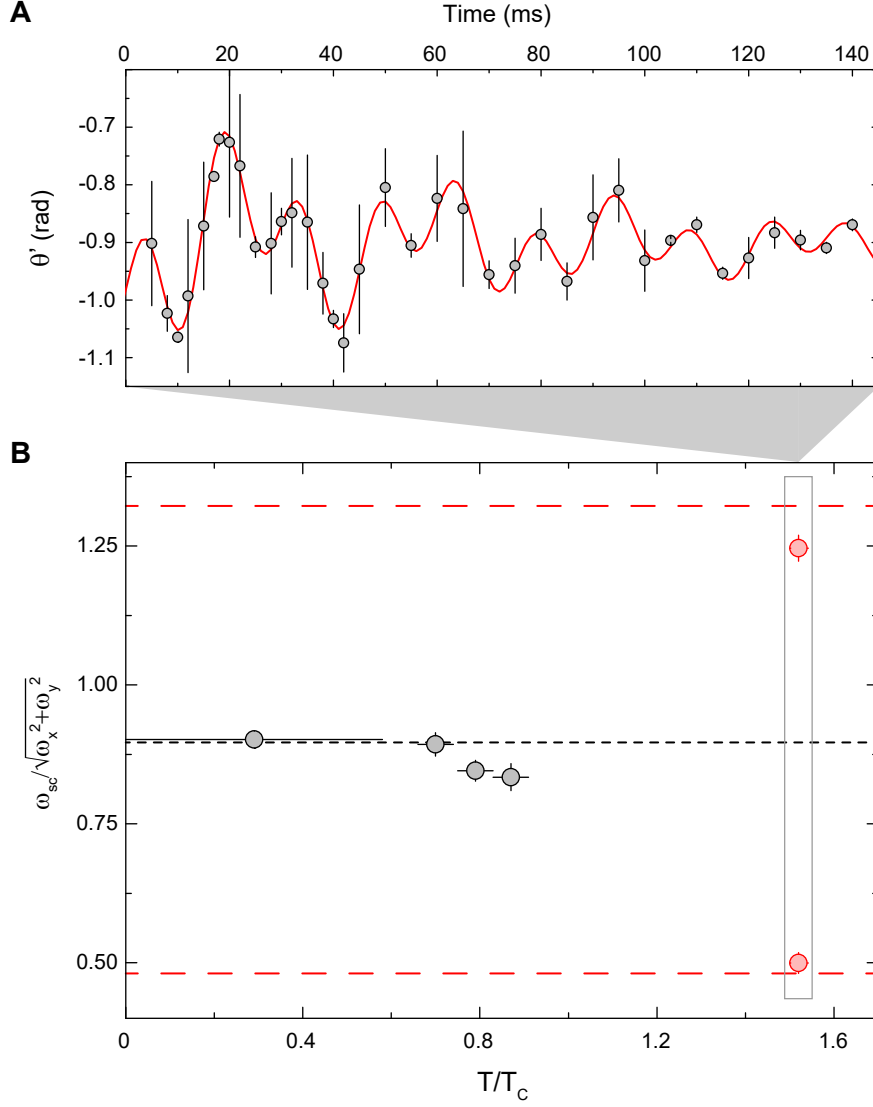


Figure 5.9: Thermal measurements of the scissors mode. For the BEC (gray points) we observe a single frequency at every temperature, which slightly decreases with increasing temperature as a consequence of the interaction with the thermal cloud. The oscillation of the thermal clouds happens with two frequencies (red points), shown in the inset. The horizontal black dashed line is the frequency in the limit of zero temperature. The red dashed lines are $\omega_{\pm} = |\omega_x \pm \omega_y|$ [42]. The errors in temperature are larger when the thermal fraction is lower. In particular, the first point is taken when no thermal fraction is detectable.

Chapter 6

Building an Optical Lattice

This chapter, conceptually disconnected from the previous ones, is devoted to the construction of an optical lattice to be employed in future researches on the supersolid state of matter. We first summarize the main scientific motivations which push us to build such a tool in our laboratory. In the remaining of the chapter, we describe the implementation of the optical lattice in our current experimental set-up and its characterization.

6.1 Scientific motivation

An optical lattice offers a new method to probe the properties of the dipolar supersolid, alternative to the previous experiments in which it was stretched, in the study of Goldstone modes [22], or rotated, in the measurement of the scissors mode described in this thesis [26]. The possible experiments we have thought to perform employing an optical lattice are of two kinds: the study of the phase transition with an external lattice or the Josephson effect between supersolid droplets.

Transition induced by an external lattice

A crucial feature of the dipolar supersolid is that the lattice period isn't imposed externally, as it happens in spin-orbit coupled BECs or in an optical cavity, but emerges directly from the interparticle interactions. It is this property that makes the dipolar supersolid compressible, as a normal solid. In the experiments, the lattice period is observed only indirectly through the measurement of the period of the momentum distribution after a free expansion. Without a theoretical model of the expansion, the exact relationship between the experimental observable and the spatial period in-situ isn't known. Moreover, even the relationship between the spatial period extracted from the ground-state simulations and the period of the supersolids created in the laboratory isn't clear. The latter, indeed, are induced by the roton instability, which has momentum k_{rot} , but how this quantity is linked to the spatial period of the supersolid? And the experimentally observed supersolids are the ground state of the system or some metastable state? To try to answer some of these questions, it would be interesting, from the experimental point of view, to have the possibility to manipulate the system with a weak optical lattice, tuning the

momentum k_L of the lattice. A first theoretical study has been performed in [86], where the authors consider the application of a weak, one-dimensional lattice with momentum k_L on a dipolar BEC. They derive the static density response function, which describes the response of the system to the perturbation, showing that it has a large peak for values of k_L near to k_{rot} . In the paper, this property is suggested to be a tool for the experimental measurement of the excitation spectrum of the dipolar gas, with its typical roton minimum. We think that it could be interesting to observe the effects of the strong susceptibility of the dipolar gas in response to a weak optical lattice, and, in particular, to observe if the induced modulation in the density persists also after the adiabatic removal of the external lattice. If this is the case, we could have access to metastable supersolid states in a region of parameters where the ground state is the BEC, with the possibility to vary the lattice period. Such an enlargement of the available parameter space through an external optical lattice has been proposed [87] and realized [88] in the striped phase of a spin-orbit coupled BEC. In this system, the lowest energy band is characterized by two local minima at distinct momenta. The optical lattice induces a momentum-space hopping between these two minima, whose coherent population produces a density modulation in real space. Other than the technical advantages resulting from the creation of supersolids with different lattice periods and in a broader range of parameters, the population of metastable supersolid states could also contribute to answer more fundamental questions, such as the order of the BEC-supersolid quantum phase transition. A first order transition, indeed, contrary to a second order one, imply the presence of metastable states near to the transition [70].

Josephson effect in a supersolid

The Josephson effect has been firstly proposed in the field of superconductors [89], where it is realized with two superconductors separated by a thin insulating barrier (the so-called Josephson junction). The well-defined phase difference Φ between the two superconductors allows a flow of particles that tunnel through the barrier, which is described by the Josephson relation [3]

$$I = I_c \sin(\Phi) \quad (6.1)$$

where I_c is the critical current, depending on the tunnelling rate. The Josephson relation predicts the flow of a current, which may take a value between $-I_c$ and I_c , through the barrier also if no voltage is applied (the dc Josephson effect). Alternatively, if a constant voltage is applied, the phase Φ increases linearly in time and then an alternate current develops (ac Josephson effect). More generally, the Josephson effect is a manifestation on a macroscopic scale of quantum coherence and, then, is strongly correlated to superfluidity. It has been observed, indeed, in most of the superfluid systems mentioned in chapter 1. In a neutral superfluid, the electrical current is substituted by a flow of particles and the oscillating quantity is the difference z in the number of particles between the two superfluid systems. In superfluid helium, for example, the Josephson junction is realized by coupling two helium baths with nano-apertures. In atomic BECs, the Josephson effect has been predicted [90] and observed [91] with a double-well potential, where two BECs are

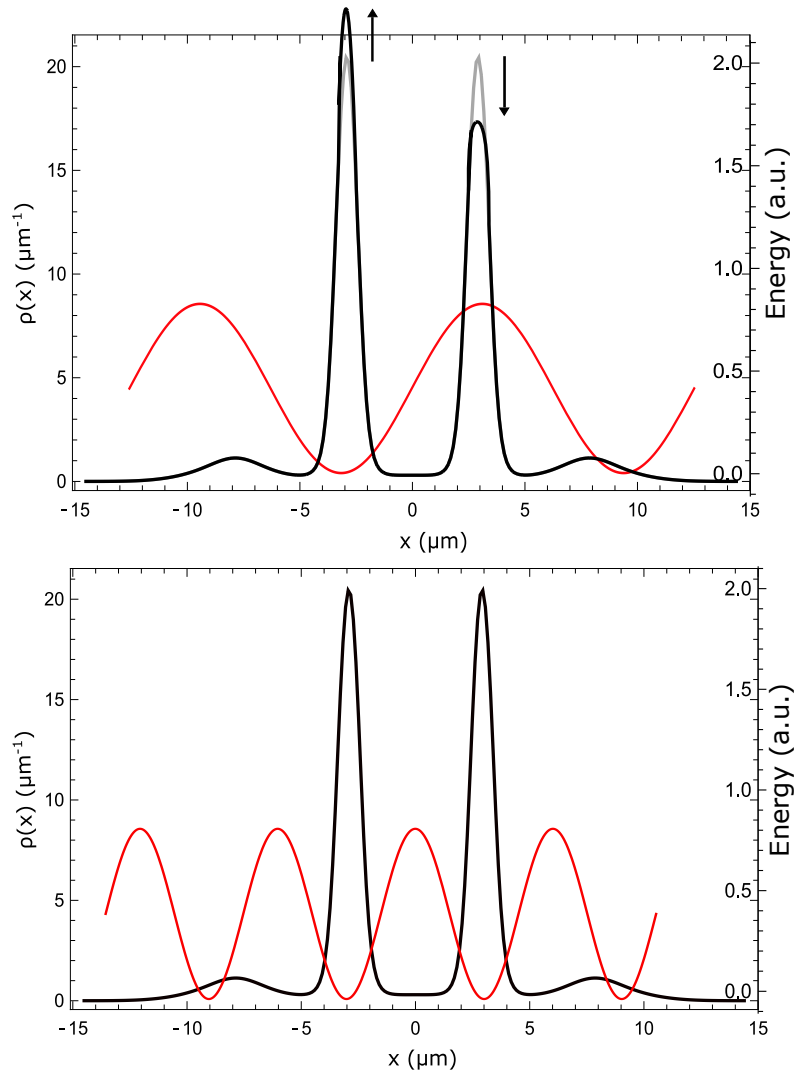


Figure 6.1: Sketch of the two possible experiments with an optical lattice, here shown in red. In the upper panel, a lattice with half the period of the supersolid could induce a Josephson oscillation between the two central peaks. In the lower panel, a lattice with a period near to the supersolid one, imposed on the BEC side, could induce the supersolid transition in a larger parameter space. The supersolid density distribution is taken from [69].

separated by a potential barrier. The role of the interactions in the junction has been extensively studied [92]. Their principal effects are the modification of the oscillation frequencies and the production of new phenomena, such as the macroscopic quantum self-trapping, which happens when the interaction energy is large enough to inhibit a complete inversion of the population.

It is clear that the physics of the supersolid is reminiscent of the Josephson effect since the global coherence allows tunnelling of atoms from one droplet to the other. Contrary to the standard Josephson junction, however, the "supersolid junction" is self-induced because the barrier between the droplets isn't imposed externally, but is produced by the same particles which participate to the superfluid flow. Such a configuration should introduce highly non-linear effects, requiring theoretical treatments to go further the simple two-modes models used so far [90]. From an experimental point of view, it would be interesting to use an optical lattice to excite a Josephson oscillation between the two principal maxima of our supersolid. The in-situ oscillation could be revealed in time of flight monitoring the same observables employed for the study on Goldstone modes [22] (see section 3.4). In this regard, we suggest a possible interpretation of the eventual Josephson-like mode in the dipolar supersolid. We know that the axial breathing mode of the BEC, which is an even mode, bifurcates into two distinct modes, always even, on the supersolid side. We highlight these two modes in the simulated diagram in Fig. 6.2, from [93]. We wouldn't be surprised if a Josephson-like mode, which should be odd, would bifurcate in the same manner on the supersolid side, generating two odd modes related to the superflow and the crystal motion, respectively. Such two odd modes are indeed present in the diagram of Fig. 6.2. An experimental study of the Josephson oscillations could clarify the previous speculations. Also the theoretical group of the University of Florence composed by B. Donelli, L. Pezzé and A. Smerzi is working on the subject, in collaboration with our experimental group.

6.2 Characterization of the lattice

In this section, we describe the construction of the optical lattice to be employed in one, or both, the two experiments described previously. We first review some basic formulae of interference and optical lattices, then we explain how to include the lattice in our current experimental set-up. We describe the two best configurations we have found and compare the results of phase-stability tests we have performed on them.

Basic formulae

As we have briefly seen in chapter 4, a far-detuned laser can act as a trap for the atoms, if its intensity has a maximum in space. More generally, engineering the spatial dependence of the intensity, one can obtain, in principle, potentials with arbitrary forms. One of the most employed configuration is the optical lattice: a periodic modulated laser intensity which produces a periodic potential on the atoms. Such a periodic geometry is easy to obtain exploiting the interference between two

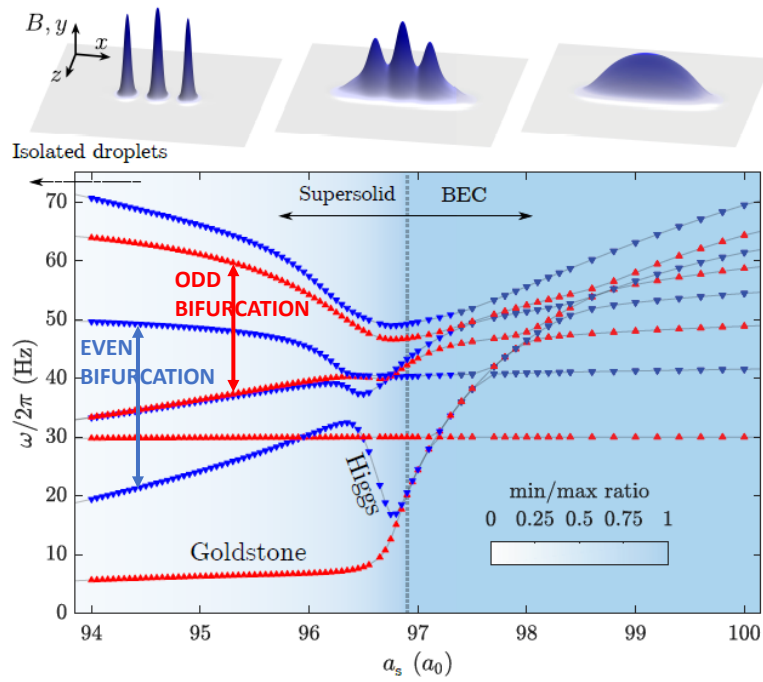


Figure 6.2: Excitation frequencies of the eight lowest modes for a trapped dipolar gas of ^{162}Dy , as a function of the scattering length. Image adapted from [93]. Red (blue) triangles indicate odd (even) modes. The background color indicates the ratio between density in between central and side droplets and peak density of the central droplet (see the inset for a sketch of the density distributions in the different regimes).

coherent laser beams. For simplicity, we consider two plane waves linearly polarized with wavenumbers \mathbf{k}_1 and \mathbf{k}_2 and frequencies ω_1 and ω_2 . The total electric field is the sum of the electric fields of each beam

$$\mathbf{E}(\mathbf{r}, t) = \mathbf{E}_1 \cos(\mathbf{k}_1 \cdot \mathbf{r} - \omega_1 t + \delta_1) + \mathbf{E}_2 \cos(\mathbf{k}_2 \cdot \mathbf{r} - \omega_2 t + \delta_2). \quad (6.2)$$

The link between the electric field and the optical potential U is given by

$$U(\mathbf{r}) = -\frac{1}{2}\alpha(\omega)\langle E(\mathbf{r}, t)^2 \rangle_t, \quad (6.3)$$

where the operation $\langle \rangle_T$ indicates a temporal average over times much larger than $1/(\omega_1 + \omega_2)$. The quantity $\alpha(\omega)$ is the real part of the dynamical polarizability, which describes the response of the atom to an oscillating electric field at the frequency ω . In general, $\alpha(\omega)$ is composed by scalar, vectorial and tensorial parts. Our optical lattice is built with a laser at 1064 nm and, for such a wavelength, the dynamical polarizability of the ^{162}Dy ground state has only a scalar part, to a good approximation. Its value is 184.4(2.4) a.u. [94]. Inserting eq. (6.2) into the optical potential (6.3), we obtain

$$U(\mathbf{r}) = \frac{U_{lat}}{2} \cos \left[(\mathbf{k}_1 - \mathbf{k}_2) \cdot \mathbf{r} + \delta_1 - \delta_2 \right], \quad (6.4)$$

apart from constant terms. The constant U_{lat} is

$$U_{lat} = -\alpha(\omega)\mathbf{E}_1 \cdot \mathbf{E}_2. \quad (6.5)$$

The interference pattern develops in the direction of $\mathbf{k}_1 - \mathbf{k}_2$, but no interference is visible if the two beams have perpendicular polarization. The period d of the interference pattern is calculated with simple geometrical considerations

$$d = \frac{\lambda}{2 \sin(\theta/2)}, \quad (6.6)$$

where λ is the wavelength of the light and θ the angle between the two beams. The less the angle is, the larger the period of the optical lattice is. The depth of the lattice, assuming that the two beams are equally polarized and with the same intensity I , i.e. $\mathbf{E}_1 = \mathbf{E}_2$, is

$$U_{lat} = \frac{2\alpha I}{\epsilon_0 c}. \quad (6.7)$$

The minus sign in eq. (6.5) can be omitted with a suitable choice of the origin. Other than the confining depth U_{lat} , there is an other energy scale associated to the presence of the lattice: the kinetic energy due to the confinement of a particle in one well. This is often defined as the ground-state kinetic energy of a particle confined within a box of length d in one dimension

$$E_0 = \frac{\hbar^2 \pi^2}{2md^2}. \quad (6.8)$$

In the case of two counterpropagating beams with wavevector k ($d = \pi/k$), E_0 becomes the recoil energy $E_r = \hbar^2 k^2 / (2m)$ with which an atom recoils after the

absorption of a photon. To compare the two energy scales, one introduces the parameter

$$s = \frac{U_{lat}}{E_0}. \quad (6.9)$$

When $s \ll 1$, particles are essentially free since they don't "feel" the lattice. When $s \gg 1$, tunnelling between minima of the lattice is suppressed and the wavefunction is confined inside the well.

A priori estimations

To produce the optical lattice, we employ a 1064 nm commercial Mephisto laser, which is used also for the two traps ODT2 and ODT3 (see chapter 5). With a beam splitter we extract some power, controllable with a half-wave plate, from the other two optical traps. The laser is injected into a photonic optical fiber and brought to the main breadboard. To perform the fiber alignment, we add two lenses in telescope configuration to reproduce the optimal beam waist, given the fiber parameter. Moreover, we add an Acusto Optical Modulator (AOM) to control the power and frequency of the beam and to perform power-stabilization with a PID. The fiber is aligned with 70 % efficiency. In principle, several hundreds of mW are available for the lattice.

To produce the optical lattice in the region where the atoms are trapped, we use a lens with $f = 200$ mm and a diameter of 2 inches, which is placed in front of an entrance window of the science cell and is at distance f from the atoms. As depicted in Fig. (6.3), the direction of propagation of the lattice beams is the same as the ODT2 so that the lattice will develop approximately in the direction of propagation of the ODT3, which is the weak-trap direction along which the supersolid forms. To calculate the expected lattice depth on the atoms, we use eq. (6.7) where the intensity I is the maximum intensity of the gaussian beam

$$I = \frac{2P}{\pi w_a^2}, \quad (6.10)$$

where P is the power in the single beam and w_a its waist on the atoms. To calculate w_a , we first measure the waist w after the fiber, resulting in $w \sim 550 \mu\text{m}$. The beam is collimated, in agreement with the calculated Rayleigh length, defined as

$$z_R = \frac{\pi w^2}{\lambda}, \quad (6.11)$$

which is the length after which the waist increases of a factor $\sqrt{2}$. The Rayleigh length after the fiber results $z_R \sim 1$ m, in agreement with a waist $w \sim 750 \mu\text{m}$ measured after 1 m of free propagation. The waist on the atoms, at distance f from the lens, is expected to be $w_a = \lambda f / (\pi w) \sim 105 \mu\text{m}$. Since we want to produce a shallow lattice, we see from eq. (6.7) that a power of 5 mW per beam is enough to produce a depth $U_{lat} \sim 48$ nK, of the order of the temperature of the system.

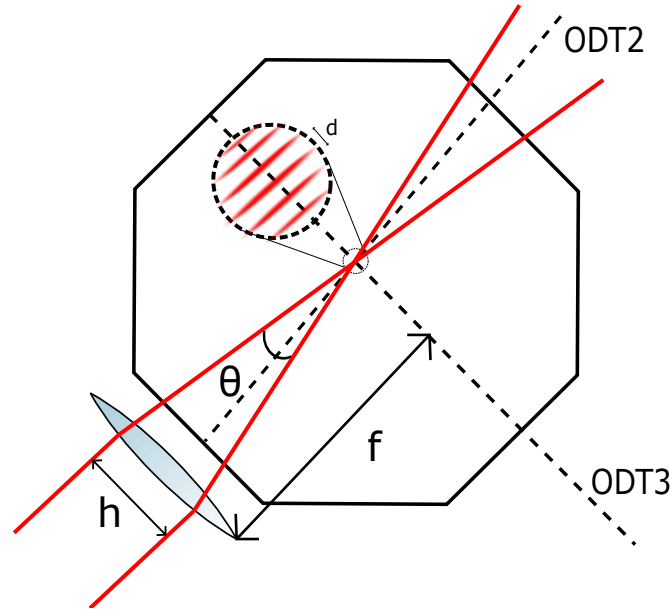


Figure 6.3: Sketch of the optical lattice geometry inside the science cell.

A more important question is the period d of the lattice. Taking into account that the distance between the droplets in our system is about $4 \mu\text{m}$, for the Josephson experiment we need a period $d \sim 8 \mu\text{m}$, while for the study of the transition we need half that value, $d \sim 4 \mu\text{m}$. To obtain the desired values for the period, we can change the horizontal displacement h between the two beams on the lens. With reference to Fig. 6.3, using eq. (6.6) and in the small-angle approximation, we obtain

$$h \sim \frac{f\lambda}{d}. \quad (6.12)$$

For a period of $8 \mu\text{m}$ we need $h = 26.6 \text{ mm}$, while for a period of $4 \mu\text{m}$ we need $h = 53.2 \text{ mm}$.

Two possible configurations

The two kinds of experiments that we have in mind require the optical lattice to satisfy different conditions. For the study of the transition, other than a smaller period of the lattice, we should be able to change the period so that we can observe the behavior of the system in function of the type of lattice imposed over it. We expect the phase stability of the lattice to be important but not so critical since the supersolid density maxima should form following the lattice. An eventual fluctuation of the phase of the lattice from experiment to experiment, although preferably to avoid, would simply translate the positions of the density peaks. On the other hand, for the Josephson experiment, the stability is fundamental, since we want to create a potential minimum exactly in the position of a supersolid density peak. Eventual fluctuations of the lattice, this time, would compromise the excitation of the Josephson oscillation. In the Josephson case, however, we don't need to change the lattice period.

Given these premises, we need to build a set-up which splits the laser beam into two beams to be focalized by the lens, searching for the optimal stability and the possibility to tune the lattice period. We have tested several configurations, finally reducing to the two depicted in Fig. 6.4-6.5. The first one employs a beam splitter and a mirror to realize two different beams, while the second one employs two beam splitters built on the same basis. The first configuration allows tuning of the period assembling the mirror on a translational stage, with which it is possible to change the displacement h . This configuration, in principle, would be suitable for both experiments. The second configuration employs two beam splitters with a side of 1 inch, i.e. 25.4 mm. The displacement h is, therefore, fixed and equal to 25.4 mm. The lattice period from eq. (6.12) is $d \sim 8.4 \mu\text{m}$, a suitable value for the Josephson experiment. Since the relative phase between the two beams depends on the difference in the optical path, we expect the principal cause of fluctuations to be variations in the length traveled by the second beam, produced by thermal drift or acoustic noise. In this sense, the less is the difference in the optical path, the less the fluctuations in the phase should be. Therefore, we expect that the more compact set-up of the two beam splitters should be more stable.

As depicted in Fig. 6.4-6.5, apart from the crucial splitting of the beam, the two configurations are identical. After the Photonic Crystal Fiber (PCF), we employ a $\lambda/2$ waveplate and a beamsplitter to clean the polarization of the beam. This first stage allows also changing the power. Next, a $\lambda/2$ waveplate is needed to equally divide the power between the two beams. After the splitting stage, a second $\lambda/2$ waveplate is employed to change the polarization after the cube, or it would be perpendicular to the other beam and no interference would be visible. Finally, a lens focuses the two beams at the distance f .

Stability of the lattice

To study the phase stability of the lattice, we observe the interference pattern on a CCD camera. The pixel size l of the camera is $4.5 \mu\text{m}$ so that the lattice periods of interest are too little to be observed. Therefore, for the tests, we use a lens with a focal of $f = 1 \text{ m}$, which tilts the beams by a lower angle, producing a larger period on the camera. A typical image of the lattice is shown in Fig. 6.6. Paying care to close the breadboard and to limit the acoustic noise to that of the experiment itself, we take sequences of images with different intervals Δt between one image and the other, and for different acquisition times.

For each sequence of images, with a program written in Mathematica, we isolate a small portion of the lattice so that it has a simple sinusoidal form. We obtain a one-dimensional intensity distribution integrating over ~ 10 pixels in the vertical direction. Then, we fit with a sinusoid

$$f(x) = A \sin(ax + \phi) + cx + of f, \quad (6.13)$$

from which we measure the phase ϕ and the period a of the lattice (in units of the pixel size). An example of the fit is shown in Fig. 6.6. The program repeats automatically the fitting procedure for each image in the sequence so that we obtain the

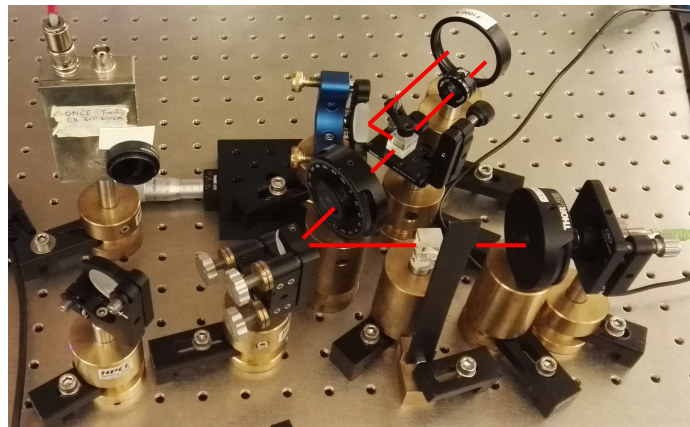
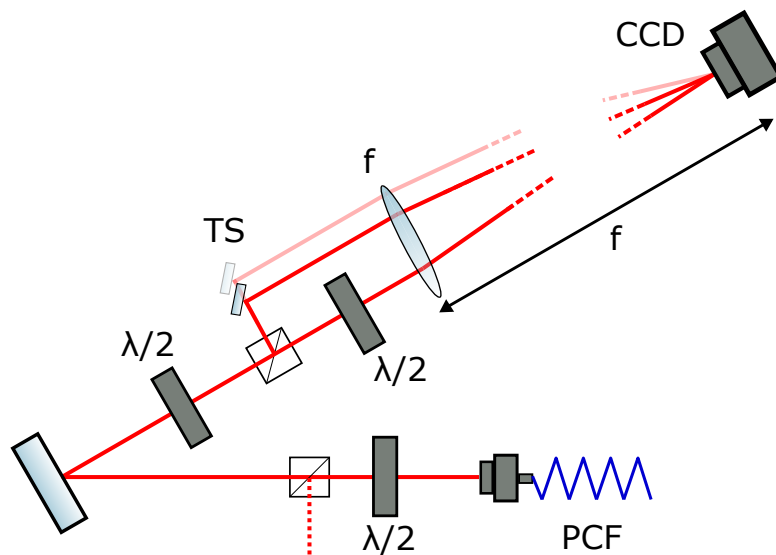


Figure 6.4: Geometry and picture of the set-up with a beam splitter and a mirror. The lattice period d can be tuned changing the position of the mirror, which is built on a translational stage (TS).

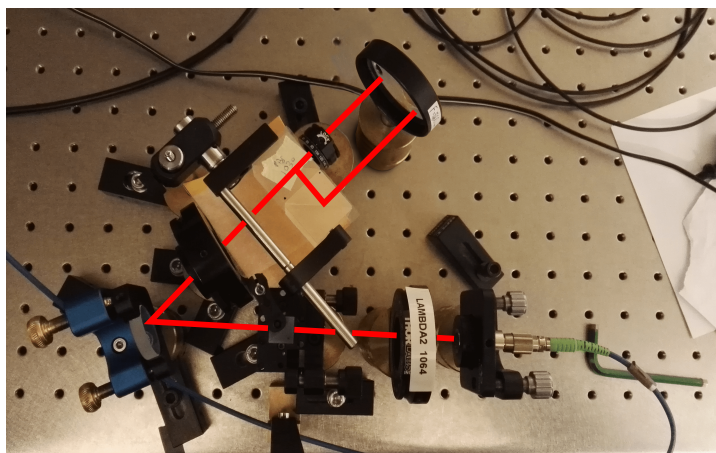
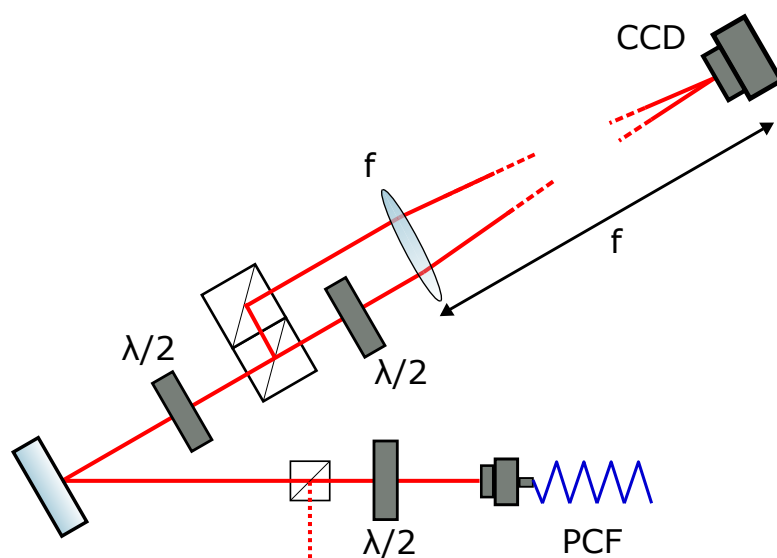


Figure 6.5: Geometry and picture of the set-up with two beam splitters.

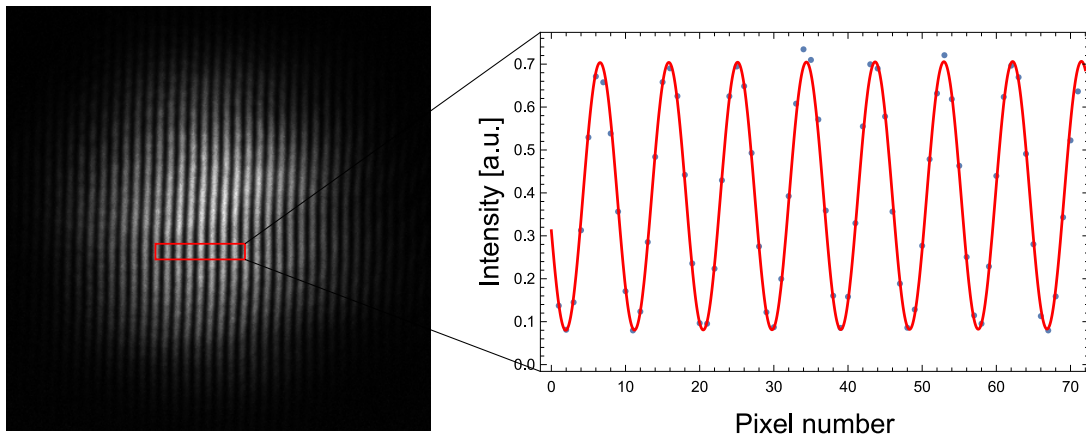


Figure 6.6: On the left, a typical image of the lattice taken with a CCD camera. For each image, a small portion of the lattice is isolated and fitted with a sinusoid function, shown on the right, to extract the phase.

time evolution of the phase. In Fig. 6.7 and Fig. 6.8 we report examples of results for both the two-cubes and the cube-mirror configurations. First, we observe that, in both cases, the measurement performed the day of the construction of the set-up shows a fast drift of the phase, with a velocity ~ 0.15 rad/min. We interpret this drift as the effect of mechanical stabilization after the construction. The following day, in fact, the measurements are different. For the mirror configuration, we observe a slower and more irregular drift with an averaged velocity ~ 0.06 rad/min, while for the two-cubes configuration the lattice is much more stable, with a residual drift of velocity ~ 0.006 rad/min. As expected, the more compact set-up is the more stable. Similar measurements performed with two cubes but with different mounts give results close to that of the mirror configuration, confirming that the common mount is crucial in minimizing the effects of the environmental noise. To observe the phase stability also on faster times, of the order of the timescales of the single experiment, we take sequences of images lasting some seconds with an interval of 100 ms between the images. This kind of test confirms the higher stability of the two-cubes configuration compared to the mirror one: as shown in Fig. 6.8 and Fig. 6.7, the phase fluctuates with standard deviations, respectively, of $\sigma_{cc} \sim 0.05$ rad and $\sigma_{cm} \sim 0.13$ rad. For the Josephson experiment, with a predicted period of $8.4 \mu\text{m}$, these values translate in a fluctuation of the interference fringes of ~ 70 nm for the two-cubes configuration and of ~ 200 nm for the mirror configuration. Although these fluctuations could be both acceptable in the single experiment, the drift at long times in the mirror configuration would produce a drift with velocity ~ 80 nm/min, which could create problems in a sequence of several experiments. In conclusion, we decide to choose the better stability conditions offered by the two-cubes configuration and, therefore, to try to perform the Josephson experiment.

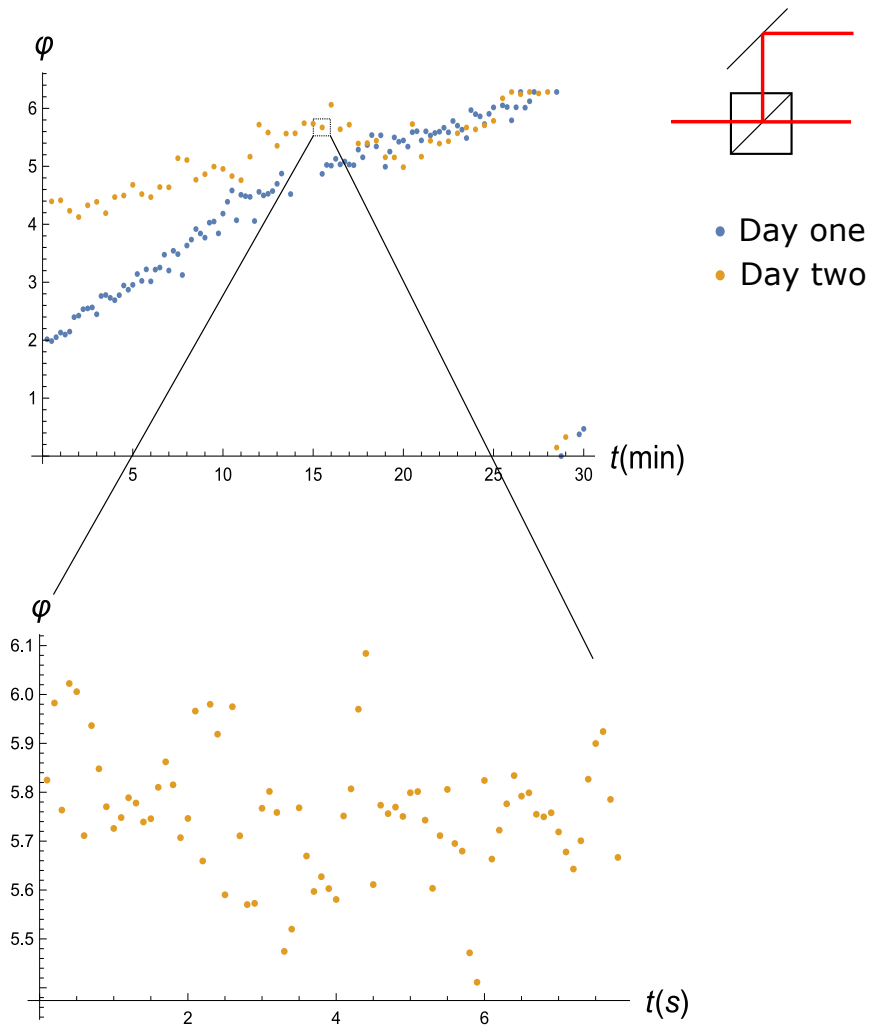


Figure 6.7: Time evolution of the phase of the lattice in the configuration with the mirror. The upper graph shows the phase for a total time of 30 minutes, with an image every 15 seconds. We report in blue a measurement performed the day of the construction of the set-up, while in yellow a measurement performed the following day. In the lower graph, the sequence of images lasts for 7 seconds, with an image every 100 ms.

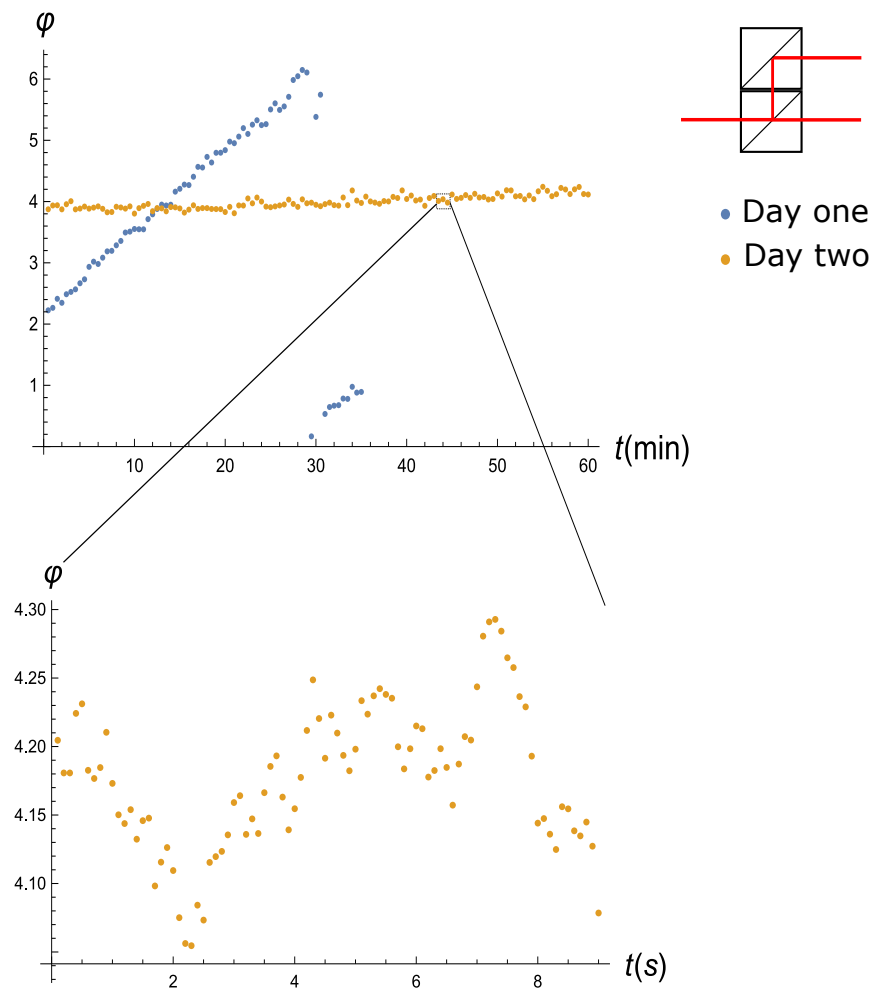


Figure 6.8: Time evolution of the phase of the lattice in the configuration with the mirror. The upper graph shows the phase for a total time of 60 minutes, with an image every 30 seconds. We report in blue a measurement performed the day of the construction of the set-up, while in yellow a measurement performed the following day. In the lower graph, the sequence of images lasts for 9 seconds, with an image every 100 ms.

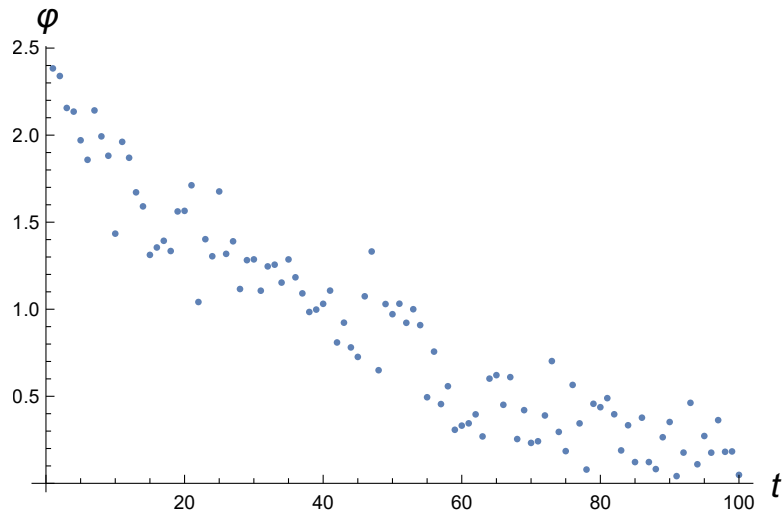


Figure 6.9: Phase of the lattice in the final configuration in a test performed the same day of the construction.

6.3 Observation of the lattice on the atoms

In this section, we show the effects of the lattice on the atoms, observable after the alignment procedure. Unfortunately, the Covid-19 emergency prevented us to complete our project. We just show the first images on the atoms, taken the very first day of measurements, from which, of course, no quantitative results can be achieved.

In the final configuration, the lattice can be observed in two different ways. After the crossing in the position occupied by the atoms, the two lattice beams exit from the opposite window of the science cell, as depicted in Fig. 6.3. We focus the two beams on a CCD camera with an optical system composed of three lenses. Since we don't know exactly the distance between the atoms and the first lens, we can't estimate the final magnification. The camera is placed in the point of intersection between the two beams so that it records a magnified image of the lattice. A measurement of the beam waist on the camera gives $w_c \sim 405 \mu\text{m}$, that, combined with the expected waist on the atoms of $w_a \sim 105 \mu\text{m}$, results in a magnification of $I = w_c/w_a \sim 3.9$. We perform the same stability test described previously, with the result shown in Fig. 6.9. The fluctuation is in agreement with the other tests performed on the same day of the construction. In the future we will make other tests, also at shorter timescales, and we will optimize the stability. The fit gives the value $a \sim 0.94$ for the coefficient in the sine function of eq. (6.13). Since the pixel size is $l = 4.5 \mu\text{m}$, the lattice period on the camera is $d_c = 2\pi l/0.94 \sim 30 \mu\text{m}$. With a magnification $I = 3.9$, the period on the atoms should be $d_a = d_c/I \sim 7.7 \mu\text{m}$, compatible with our a priori estimation and suitable for the Josephson experiment. Since the atoms are observed with blue light while the lattice is made of infrared light, we can't use the same camera to observe both. The refraction indexes of the BK7 glass of the same set of lenses employed at the two different wavelengths differ, indeed, by the 1.5 %. As a consequence, the focus of the atomic imaging system is in a different position compared to the point where the lattice forms.

Anyway, the effects of the lattice on the atoms can be observed with the vertical camera. The interaction with the lattice introduces in the hamiltonian a term of the form $U_{lat} \cos^2(kx)$, with x the direction of the lattice. Note that in our system the wavevector k is given by $k = \pi/d$. Switching on the lattice for a variable time τ , we observe the momentum distribution in time of flight. The optical lattice acts as a diffraction grating for the atoms, whose momentum distribution shows a series of peaks in the direction of the lattice at the values $\pm 2n\hbar k$, with n natural. This phenomenon, exactly opposite compared to the more common diffraction of light from a material grating, is called Kapitza-Dirac effect and its experimental observation has provided the demonstration of the quantized exchange of momentum between the laser field and the atoms [95]. It can be understood, indeed, as a sequence of n absorption-stimulated emission processes involving the two laser beams, in which the atom gains (or loses) a momentum equal to $2n\hbar k$. If the interaction time τ is much less than the oscillation period T in one potential well, we can neglect the dynamics in the lattice. Under this approximation, the population of the n -th diffracted order is [96]

$$P_n = J_n^2\left(\frac{U_{lat}\tau}{\hbar}\right), \quad (6.14)$$

where $J_n(x)$ is the n -th Bessel function of the first kind. In the experiment we choose $\tau = 1$ ms so that, with our parameters, we have $\tau/T \sim 0.02$. We observe the cloud on the vertical camera, whose pixel size is $l = 6.5 \mu\text{m}$, after an expansion time $t_{exp} = 56$ ms. The magnification of the optical system is $I = 1.5$. With this numbers and assuming the period of the optical lattice to be $d = 7.7 \mu\text{m}$, we can estimate the period of the diffraction pattern on the camera $\bar{k}_c = \frac{2\pi\hbar t_{exp}}{md} \frac{I}{l} \sim 4$ pixels. This is at the limit of our resolution and makes a quantitative measurement very challenging (see Fig. 6.10). Of course in future acquisitions it will be convenient to set a larger expansion time. Note that the n -th Bessel function, appearing in the populations of eq. (6.14), is an oscillating function that is significantly different from zero when its argument is of order n or larger. This means that, depending on the value of the argument, a different number of diffraction orders may be populated. For our experimental configuration, with a potential of the order $U_{lat} \sim 100$ nK and $\tau = 1$ ms, the argument of the Bessel functions is ~ 10 so that 10 diffraction orders are likely to be populated. Moreover, there is no warranty that the intensity is maximum for the lowest-order peaks and decreases increasing the order, as it happens in the standard diffraction of light from a grating, since the amplitude of the Bessel functions oscillates. As a consequence, some orders may also be suppressed. This is depicted in Fig. 6.10. Although we are at the limit of the resolution of the camera, we perform a fit with six equispaced Gaussian, grouped two by two, verifying that two diffraction orders every three are populated. The fitted period is $\bar{k}_c \sim 4$ pixels, confirming again that the period of the lattice on the atoms is about $8 \mu\text{m}$.

To perform a first stability test, we focus on a group of experimental images in which the diffraction pattern is particularly well resolved, with an average period of $\bar{k}_c \sim 11$ pixels. An example is reported in Fig. 6.11. If the previous estimation is correct, this would correspond to a situation in which we have one peak visible

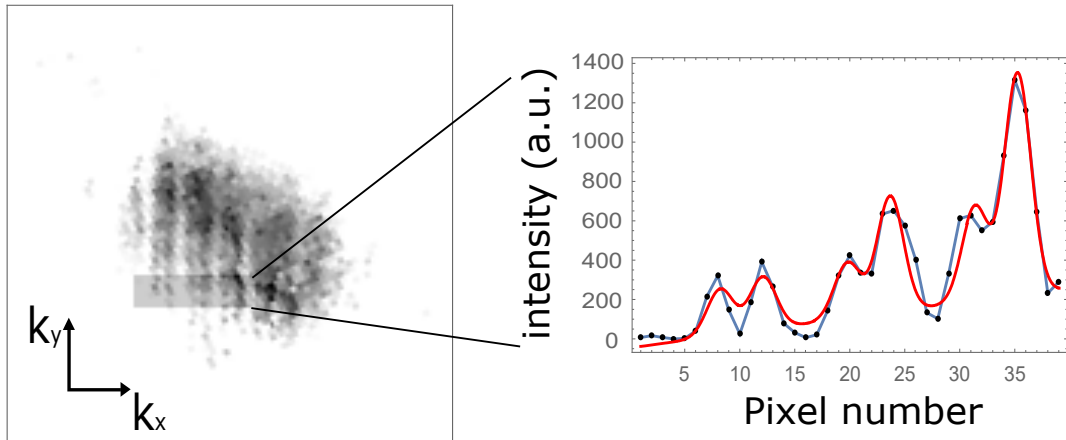


Figure 6.10: Kapitza-Dirac diffraction. Experimental image of the density distribution of the atoms diffracted by the optical lattice and corresponding fit performed on a small portion of the image. The fit is performed with six Gaussians and confirms that the period on the camera is $\bar{k}_c \sim 4$ pixels, corresponding to the expected value on the atoms of about $8 \mu\text{m}$. From the fit, we also see that, in this particular image, two diffraction orders are populated every three.

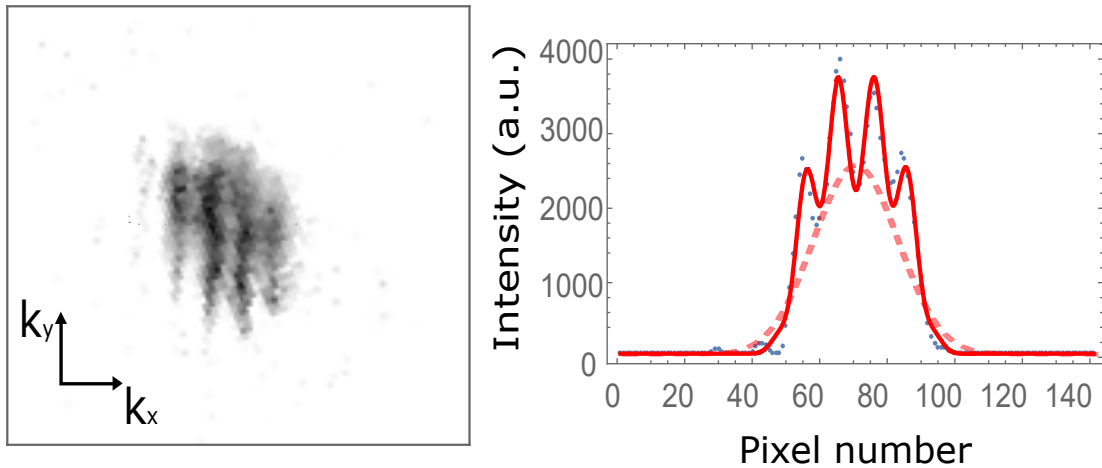


Figure 6.11: Kapitza-Dirac diffraction for an image with well-resolved peaks, corresponding to the population of one diffraction order every three. On the left, the momentum distribution of the atoms after the diffraction from the optical lattice. On the right, one-dimensional distribution and fit with the double-slit model to extract the phase of the interference. The Gaussian envelope, which provides the position of the cloud, is plotted with a dashed line.

every three. In addition to the fluctuations of the optical lattice, we expect also fluctuations of the atomic cloud itself, which can be caused by small displacements of the mirrors of the optical traps or by magnetic field fluctuations, for example. We can't even exclude fluctuations of the CCD. The measurement of the lattice phase in Fig. 6.9 suggests that the system lattice plus CCD is stable at the level of the preliminary tests, although the CCD employed in that case is the horizontal one. From the diffraction pattern we measure the center of the Gaussian envelope and the phase of the interference with the double-slit fitting function, used also for the supersolid distribution (see chapter 4). The results are reported in Fig. 6.12. We observe indeed a fluctuation in the center x_0 of the envelope, which probably reflects a relative velocity between the atoms and the lattice. The standard deviation $\sigma_k = 1.4$ pixels translates into an in-trap velocity of $\delta v \sim 100$ nm/ms, which could be a reasonable value for fluctuations of the atomic cloud induced by the optical traps. We find a strong fluctuation also in the phase, with $\sigma_p = 0.6$ rad. Note that in this case, we use a $\sin^2 x$ function so that the period is π and not 2π as in the fit of eq. (6.13). A fluctuation of the CCD would produce a phase shift proportional to the shift in x_0 , i.e. $\delta\phi = \bar{k}_c \delta x_0$. The plot of the phase versus x_0 shows no correlation so that we can rule out this possibility as the main contribution to fluctuations.

To summarize, we have performed preliminary tests of the stability of the system composed of the optical lattice plus the atomic cloud. Due to the Covid-19 emergency, we have been forced to use just the images of the very first day of measurements. Although we haven't been able to extract quantitative results from these images, with the previous preliminary analysis we set the stage for further investigations which we will conduct as soon as possible. Once that we will reach acceptable stability, we will study the Josephson effect in the supersolid.

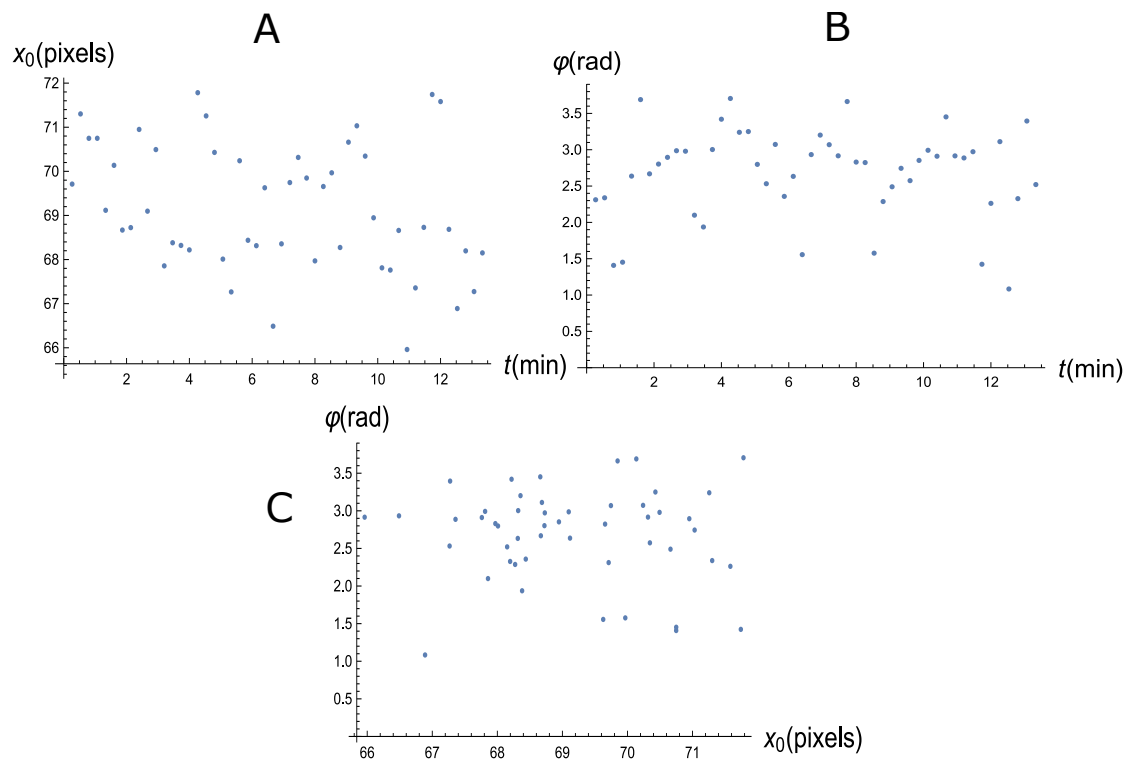


Figure 6.12: Results of the fit of the diffraction pattern. (A) Fluctuations of the centers of the Gaussian envelope, with standard deviation $\sigma_k = 1.4$ pixels. (B) Fluctuations in the phase of the interference with standard deviation $\sigma_p = 0.6$ rad. (C) Absence of correlation between the two fluctuations.

Conclusions

The principal result of the thesis is the demonstration of the superfluid behavior of the recently discovered dipolar supersolid. Such a demonstration has been carried out studying the supersolid response to a rotation excitation and, therefore, constitutes a direct proof of its superfluidity. The experiment described in the thesis can be considered as the first successful realization of the original proposal by Leggett [9] and the prosecution, in the field of quantum gases, of the many experiments carried out in the helium community for over a decade. Of course, the dipolar supersolid is very different compared to the helium supersolid: it is a cluster supersolid in an optical trap so that it is a non-homogeneous system. To study the rotational properties of such a system, I employed the scissors mode, an excitation mode of a trapped system also used as an experimental tool for the probing of the superfluid properties of standard BECs [25]. The scissors mode, in the small-angle limit, corresponds to an oscillation of the cloud around one of its axes, which resembles the torsional oscillator experiments attempted with solid helium. As in the helium case, the measurement of the frequency of the oscillation allows the determination of the moment of inertia of the system. The main difficulty of such a measurement is the presence of an unavoidable axial-breathing mode, which gets excited crossing the transition with an amplitude of about 10 %. If the amplitude is too large, the peculiar supersolid behavior is washed out. To optimize the measurement of the scissors frequency, I developed an excitation method that constitutes a good balance between the requirements of having a strong signal and avoiding a too large excitation of the axial-breathing mode. The results show a clear reduction of the scissors frequency crossing the BEC-supersolid transition, which corresponds to an increase in the moment of inertia. The latter, however, keeps well below the classical value, demonstrating the superfluid behavior of the supersolid under rotation. I also estimate the superfluid fraction of the dipolar supersolid generalizing the usual definition for a cylindrical system. The nominal values give a superfluid fraction of the order of 90 %, in agreement with the expectation that the supersolid isn't fully superfluid even at zero temperature due to the breaking of translation invariance. However, the experimental uncertainty prevents from claiming a superfluid fraction less than 100 %. Such large values of the superfluid fraction compared with the helium case (current estimations are $f_s < 10^{-4}$) derive from the clustering nature of the dipolar supersolid. Finally, I employed simulated density profiles of the supersolid for our specific experimental configuration, performed in [69], to apply Leggett's original estimation of the superfluid fraction to our system. Remarkably, I obtained an agreement within one order of magnitude, despite the many differences between our system and Leggett's one, thought for a helium-like supersolid.

With an increase of the supersolid lifetime and the atom number, which could be obtained, for example, employing the isotope ^{164}Dy , the experimental techniques developed in this thesis could be applied to lower the experimental error and test if the superfluid fraction is indeed lower than 100 %. More generally, a larger system might allow a deeper study of the connection between density modulation and superfluid fraction, getting closer to Leggett's ideal experiment. Reaching a regime of higher angular velocities, moreover, could give access to the exciting physics of vortices in a supersolid.

Throughout the thesis, I have developed two other interesting lines of research, which I intend to pursue in the future. First, I have built the minimal form of a theoretical model that explains the supersolid transition linking the dipolar interaction in a trapped system to a soft-core interaction. In the context of the thesis, this model has been employed just as a qualitative explanation of the reason why the energy terms into play should give rise to the supersolid phase observed in the experiments. However, it would be interesting to make the model more realistic, also with the implementation of some simulations, to predict properties of a two-dimensional supersolid, as, for example, the regime of parameters in which it should exist. This theoretical task would also be of great experimental relevance since one of the goals of our experiment is to produce a two-dimensional supersolid with more droplets and fewer atoms per droplet. Second, I have built and characterized an optical lattice for a new experimental study of the dipolar supersolid. As I have explained in chapter 6, the optical lattice could be used for both technical improvements and the study of fundamental physics. In the first case, there is the possibility of the enlargement of the parameter space of existence of the supersolid and the opportunity of tuning the supersolid lattice constant. In the second case, there is the study of the order of the transition and of the Josephson effect in the supersolid, which would be the first Josephson junction auto-induced ever observed. The next step in these directions is the accomplishment of the stability tests comprising both the atomic cloud and the optical lattice, just started during the thesis, which have been stopped due to the Covid-19 emergency.

Bibliography

- [1] Anthony J Leggett. *Quantum Liquids: Bose condensation and Cooper pairing in condensed-matter systems*, volume 9780198526438. Oxford University Press, United States, 2008.
- [2] C. Pethick and H. Smith. *Bose-Einstein condensation in dilute gases*. Cambridge University Press, 2002.
- [3] L. Pitaevskii and S. Stringari. *Bose-Einstein Condensation and Superfluidity*. International Series of Monographs on Physics. OUP Oxford, 2016.
- [4] A. J. Leggett. Superfluidity. *Rev. Mod. Phys.*, 71:S318–S323, 1999.
- [5] Massimo Boninsegni and Nikolay V. Prokof'ev. Colloquium: Supersolids: What and where are they? *Rev. Mod. Phys.*, 84:759–776, 2012.
- [6] Eugene P. Gross. Unified theory of interacting bosons. *Phys. Rev.*, 106:161–162, 1957.
- [7] Aleksandr F Andreev and I M Lifshitz. Quantum theory of defects in crystals. *Soviet Physics Uspekhi*, 13(5):670–670, 1971.
- [8] G. V. Chester. Speculations on bose-einstein condensation and quantum crystals. *Phys. Rev. A*, 2:256–258, 1970.
- [9] A. J. Leggett. Can a solid be "superfluid"? *Phys. Rev. Lett.*, 25:1543–1546, 1970.
- [10] E. Kim and M. H. W. Chan. Probable observation of a supersolid helium phase. *Nature*, 427(6971):225–227, 2004.
- [11] E. Kim and M. H. W. Chan. Observation of superflow in solid helium. *Science*, 305(5692):1941–1944, 2004.
- [12] Sebastien Balibar. The enigma of supersolidity. *Nature*, 464(7286):176–182, 2010.
- [13] Duk Y. Kim and Moses H. W. Chan. Absence of supersolidity in solid helium in porous vycor glass. *Phys. Rev. Lett.*, 109:155301, 2012.
- [14] M. Boninsegni. Supersolid phases of cold atom assemblies. *Journal of Low Temperature Physics*, 168(3):137–149, 2012.

- [15] Jun-Ru Li, Jeongwon Lee, Wujie Huang, Sean Burchesky, Boris Shteynas, Furkan Çagri Top, Alan O. Jamison, and Wolfgang Ketterle. A stripe phase with supersolid properties in spin-orbit-coupled bose-einstein condensates. *Nature*, 543(7643):91–94, 2017.
- [16] Julian Léonard, Andrea Morales, Philip Zupancic, Tilman Esslinger, and Tobias Donner. Supersolid formation in a quantum gas breaking a continuous translational symmetry. *Nature*, 543(7643):87–90, 2017.
- [17] T Lahaye, C Menotti, L Santos, M Lewenstein, and T Pfau. The physics of dipolar bosonic quantum gases. *Reports on Progress in Physics*, 72(12):126401, 2009.
- [18] Igor Ferrier-Barbut, Holger Kadau, Matthias Schmitt, Matthias Wenzel, and Tilman Pfau. Observation of quantum droplets in a strongly dipolar bose gas. *Phys. Rev. Lett.*, 116:215301, 2016.
- [19] L. Tanzi, E. Lucioni, F. Famà, J. Catani, A. Fioretti, C. Gabbanini, R. N. Bisset, L. Santos, and G. Modugno. Observation of a dipolar quantum gas with metastable supersolid properties. *Phys. Rev. Lett.*, 122:130405, 2019.
- [20] L. Chomaz, D. Petter, P. Ilzhöfer, G. Natale, A. Trautmann, C. Politi, G. Durastante, R. M. W. van Bijnen, A. Patscheider, M. Sohmen, M. J. Mark, and F. Ferlaino. Long-lived and transient supersolid behaviors in dipolar quantum gases. *Phys. Rev. X*, 9:021012, 2019.
- [21] Fabian Böttcher, Jan-Niklas Schmidt, Matthias Wenzel, Jens Hertkorn, Mingyang Guo, Tim Langen, and Tilman Pfau. Transient supersolid properties in an array of dipolar quantum droplets. *Phys. Rev. X*, 9:011051, 2019.
- [22] L. Tanzi, S. M. Rocuzzo, E. Lucioni, F. Famà, A. Fioretti, C. Gabbanini, G. Modugno, A. Recati, and S. Stringari. Supersolid symmetry breaking from compressional oscillations in a dipolar quantum gas. *Nature*, 574(7778):382–385, 2019.
- [23] Mingyang Guo, Fabian Böttcher, Jens Hertkorn, Jan-Niklas Schmidt, Matthias Wenzel, Hans Peter Büchler, Tim Langen, and Tilman Pfau. The low-energy goldstone mode in a trapped dipolar supersolid. *Nature*, 574(7778):386–389, 2019.
- [24] G. Natale, R. M. W. van Bijnen, A. Patscheider, D. Petter, M. J. Mark, L. Chomaz, and F. Ferlaino. Excitation spectrum of a trapped dipolar supersolid and its experimental evidence. *Phys. Rev. Lett.*, 123:050402, 2019.
- [25] O. M. Maragò, S. A. Hopkins, J. Arlt, E. Hodby, G. Hechenblaikner, and C. J. Foot. Observation of the scissors mode and evidence for superfluidity of a trapped bose-einstein condensed gas. *Phys. Rev. Lett.*, 84:2056–2059, 2000.
- [26] L. Tanzi, J. G. Maloberti, G. Biagioni, A. Fioretti, C. Gabbanini, and G. Modugno. Evidence of superfluidity in a dipolar supersolid from non-classical rotational inertia, 2019. Preprint: [arXiv:1912.01910](https://arxiv.org/abs/1912.01910). Submitted to Science.

- [27] P. Kapitza. Viscosity of liquid helium below the λ -point. *Nature*, 141(3558):74–74, 1938.
- [28] J. F. Allen and A. D. Misener. Flow of liquid helium ii. *Nature*, 141(3558):75–75, 1938.
- [29] Dany Page, Madappa Prakash, James M. Lattimer, and Andrew W. Steiner. Rapid cooling of the neutron star in cassiopeia *a* triggered by neutron superfluidity in dense matter. *Phys. Rev. Lett.*, 106:081101, 2011.
- [30] K. G. Lagoudakis, M. Wouters, M. Richard, A. Baas, I. Carusotto, R. André, Le Si Dang, and B. Deveaud-Plédran. Quantized vortices in an exciton-polariton condensate. *Nature Physics*, 4(9):706–710, 2008.
- [31] Lasha Berezhiani and Justin Khoury. Theory of dark matter superfluidity. *Phys. Rev. D*, 92:103510, 2015.
- [32] G. B. Hess and W. M. Fairbank. Measurements of angular momentum in superfluid helium. *Phys. Rev. Lett.*, 19:216–218, 1967.
- [33] Eric Varoquaux. Anderson’s considerations on the flow of superfluid helium: Some offshoots. *Rev. Mod. Phys.*, 87:803–854, 2015.
- [34] I. Coddington, P. Engels, V. Schweikhard, and E. A. Cornell. Observation of tkachenko oscillations in rapidly rotating bose-einstein condensates. *Phys. Rev. Lett.*, 91:100402, 2003.
- [35] Olli V. Lounasmaa and Erkki Thuneberg. Vortices in rotating superfluid ^3He . *Proceedings of the National Academy of Sciences*, 96(14):7760–7767, 1999.
- [36] F. Chevy, K. W. Madison, and J. Dalibard. Measurement of the angular momentum of a rotating bose-einstein condensate. *Phys. Rev. Lett.*, 85:2223–2227, 2000.
- [37] M. W. Zwierlein, J. R. Abo-Shaeer, A. Schirotzek, C. H. Schunck, and W. Ketterle. Vortices and superfluidity in a strongly interacting fermi gas. *Nature*, 435(7045):1047–1051, 2005.
- [38] Charles Kittel. *Introduction to Solid State Physics*. Wiley, 8 edition, 2004.
- [39] A. J. Leggett. On the superfluid fraction of an arbitrary many-body system at $T=0$. *Journal of Statistical Physics*, 93(3):927–941, 1998.
- [40] M. H. W. Chan, R. B. Hallock, and L. Reatto. Overview on solid ^4He and the issue of supersolidity. *Journal of Low Temperature Physics*, 172(5):317–363, 2013.
- [41] James Day and John Beamish. Low-temperature shear modulus changes in solid ^4He and connection to supersolidity. *Nature*, 450(7171):853–856, 2007.
- [42] D. Guéry-Odelin and S. Stringari. Scissors mode and superfluidity of a trapped bose-einstein condensed gas. *Phys. Rev. Lett.*, 83:4452–4455, 1999.

- [43] N. Lo Iudice and F. Palumbo. New isovector collective modes in deformed nuclei. *Phys. Rev. Lett.*, 41:1532–1534, 1978.
- [44] Onofrio Maragò, Gerald Hechenblaikner, Eleanor Hodby, and Christopher Foot. Temperature dependence of damping and frequency shifts of the scissors mode of a trapped bose-einstein condensate. *Phys. Rev. Lett.*, 86:3938–3941, 2001.
- [45] O M Maragò, G Hechenblaikner, E Hodby, S A Hopkins, and C J Foot. The moment of inertia and the scissors mode of a bose-condensed gas. *Journal of Physics: Condensed Matter*, 14(3):343–354, 2001.
- [46] J. Stuhler, A. Griesmaier, T. Koch, M. Fattori, T. Pfau, S. Giovanazzi, P. Pedri, and L. Santos. Observation of dipole-dipole interaction in a degenerate quantum gas. *Phys. Rev. Lett.*, 95:150406, 2005.
- [47] Q. Beaufils, R. Chicireanu, T. Zanon, B. Laburthe-Tolra, E. Maréchal, L. Vernac, J.-C. Keller, and O. Gorceix. All-optical production of chromium bose-einstein condensates. *Phys. Rev. A*, 77:061601, 2008.
- [48] K. Aikawa, A. Frisch, M. Mark, S. Baier, A. Rietzler, R. Grimm, and F. Ferlaino. Bose-einstein condensation of erbium. *Phys. Rev. Lett.*, 108:210401, 2012.
- [49] Mingwu Lu, Nathaniel Q. Burdick, Seo Ho Youn, and Benjamin L. Lev. Strongly dipolar bose-einstein condensate of dysprosium. *Phys. Rev. Lett.*, 107:190401, 2011.
- [50] A. Campa, T. Dauxois, D. Fanelli, and S. Ruffo. *Physics of Long-range Interacting Systems*. Oxford University Press, 2014.
- [51] Fabio Cinti and Massimo Boninsegni. Absence of superfluidity in 2d dipolar bose striped crystals. *Journal of Low Temperature Physics*, 196(5):413–422, 2019.
- [52] K. Aikawa, A. Frisch, M. Mark, S. Baier, R. Grimm, and F. Ferlaino. Reaching fermi degeneracy via universal dipolar scattering. *Phys. Rev. Lett.*, 112:010404, 2014.
- [53] Mingwu Lu, Nathaniel Q. Burdick, and Benjamin L. Lev. Quantum degenerate dipolar fermi gas. *Phys. Rev. Lett.*, 108:215301, 2012.
- [54] Claudia Eberlein, Stefano Giovanazzi, and Duncan H. J. O’Dell. Exact solution of the thomas-fermi equation for a trapped bose-einstein condensate with dipole-dipole interactions. *Phys. Rev. A*, 71:033618, 2005.
- [55] L. Santos, G. V. Shlyapnikov, and M. Lewenstein. Roton-maxon spectrum and stability of trapped dipolar bose-einstein condensates. *Phys. Rev. Lett.*, 90:250403, 2003.

- [56] L. Chomaz, R. M. W. van Bijnen, D. Petter, G. Faraoni, S. Baier, J. H. Becher, M. J. Mark, F. Wächtler, L. Santos, and F. Ferlaino. Observation of roton mode population in a dipolar quantum gas. *Nature Physics*, 14(5):442–446, 2018.
- [57] A. R. P. Lima and A. Pelster. Beyond mean-field low-lying excitations of dipolar bose gases. *Phys. Rev. A*, 86:063609, 2012.
- [58] D. S. Petrov. Quantum mechanical stabilization of a collapsing bose-bose mixture. *Phys. Rev. Lett.*, 115:155302, 2015.
- [59] G. Semeghini, G. Ferioli, L. Masi, C. Mazzinghi, L. Wolswijk, F. Minardi, M. Modugno, G. Modugno, M. Inguscio, and M. Fattori. Self-bound quantum droplets of atomic mixtures in free space. *Phys. Rev. Lett.*, 120:235301, 2018.
- [60] C. R. Cabrera, L. Tanzi, J. Sanz, B. Naylor, P. Thomas, P. Cheiney, and L. Tarruell. Quantum liquid droplets in a mixture of bose-einstein condensates. *Science*, 359(6373):301–304, 2018.
- [61] Holger Kadau, Matthias Schmitt, Matthias Wenzel, Clarissa Wink, Thomas Maier, Igor Ferrier-Barbut, and Tilman Pfau. Observing the rosenzweig instability of a quantum ferrofluid. *Nature*, 530(7589):194–197, 2016.
- [62] M. Rossi, S. L. Zavattari, D. E. Galli, and L. Reatto. Off-diagonal long-range order studied in a soft-core solid: Two-dimensional screened coulomb bosons. *Phys. Rev. B*, 84:052504, 2011.
- [63] F. Cinti, T. Macrì, W. Lechner, G. Pupillo, and T. Pohl. Defect-induced supersolidity with soft-core bosons. *Nature Communications*, 5(1):3235, 2014.
- [64] F. Cinti, P. Jain, M. Boninsegni, A. Micheli, P. Zoller, and G. Pupillo. Supersolid droplet crystal in a dipole-blockaded gas. *Phys. Rev. Lett.*, 105:135301, 2010.
- [65] N. Henkel, R. Nath, and T. Pohl. Three-dimensional roton excitations and supersolid formation in rydberg-excited bose-einstein condensates. *Phys. Rev. Lett.*, 104:195302, 2010.
- [66] C. N. Likos, A. Lang, M. Watzlawek, and H. Löwen. Criterion for determining clustering versus reentrant melting behavior for bounded interaction potentials. *Phys. Rev. E*, 63:031206, 2001.
- [67] T. Boulier, E. Magnan, C. Bracamontes, J. Maslek, E. A. Goldschmidt, J. T. Young, A. V. Gorshkov, S. L. Rolston, and J. V. Porto. Spontaneous avalanche dephasing in large rydberg ensembles. *Phys. Rev. A*, 96:053409, 2017.
- [68] D. Baillie, R. M. Wilson, R. N. Bisset, and P. B. Blakie. Self-bound dipolar droplet: A localized matter wave in free space. *Phys. Rev. A*, 94:021602, 2016.
- [69] S. M. Roccuzzo, A. Gallemí, A. Recati, and S. Stringari. Rotating a supersolid dipolar gas. *Phys. Rev. Lett.*, 124:045702, 2020.

- [70] N. Goldenfeld. *Lectures On Phase Transitions And The Renormalization Group*. CRC Press, 2018.
- [71] P. M. Chaikin and T. C. Lubensky. *Principles of Condensed Matter Physics*. Cambridge University Press, Cambridge, 1995.
- [72] S. Saccani, S. Moroni, and M. Boninsegni. Excitation spectrum of a supersolid. *Phys. Rev. Lett.*, 108:175301, 2012.
- [73] S. Stringari. Collective excitations of a trapped bose-condensed gas. *Phys. Rev. Lett.*, 77:2360–2363, 1996.
- [74] M.-O. Mewes, M. R. Andrews, N. J. van Druten, D. M. Kurn, D. S. Durfee, C. G. Townsend, and W. Ketterle. Collective excitations of a bose-einstein condensate in a magnetic trap. *Phys. Rev. Lett.*, 77:988–991, 1996.
- [75] R. M. W. van Bijnen, N. G. Parker, S. J. J. M. F. Kokkelmans, A. M. Martin, and D. H. J. O’Dell. Collective excitation frequencies and stationary states of trapped dipolar bose-einstein condensates in the thomas-fermi regime. *Phys. Rev. A*, 82:033612, 2010.
- [76] Thomas Chalopin, Tanish Satoor, Alexandre Evrard, Vasiliy Makhlov, Jean Dalibard, Raphael Lopes, and Sylvain Nascimbene. Exploring the topology of a quantum hall system at the microscopic level, 2020. Preprint: [arXiv:2001.01664](https://arxiv.org/abs/2001.01664).
- [77] C. Cohen-Tannoudji and D. Guéry-Odelin. *Advances in Atomic Physics: An Overview*. World Scientific, 2011.
- [78] E. Lucioni, G. Masella, A. Fregosi, C. Gabbanini, S. Gozzini, A. Fioretti, L. Del Bino, J. Catani, G. Modugno, and M. Inguscio. A new setup for experiments with ultracold dysprosium atoms. *The European Physical Journal Special Topics*, 226(12):2775–2780, 2017.
- [79] E. Lucioni, L. Tanzi, A. Fregosi, J. Catani, S. Gozzini, M. Inguscio, A. Fioretti, C. Gabbanini, and G. Modugno. Dysprosium dipolar bose-einstein condensate with broad feshbach resonances. *Phys. Rev. A*, 97:060701, 2018.
- [80] Fabian Böttcher, Matthias Wenzel, Jan-Niklas Schmidt, Mingyang Guo, Tim Langen, Igor Ferrier-Barbut, Tilman Pfau, Raúl Bombín, Joan Sánchez-Baena, Jordi Boronat, and Ferran Mazzanti. Dilute dipolar quantum droplets beyond the extended gross-pitaevskii equation. *Phys. Rev. Research*, 1:033088, 2019.
- [81] Igor Ferrier-Barbut, Matthias Wenzel, Fabian Böttcher, Tim Langen, Mathieu Isoard, Sandro Stringari, and Tilman Pfau. Scissors mode of dipolar quantum droplets of dysprosium atoms. *Phys. Rev. Lett.*, 120:160402, 2018.
- [82] M. Modugno, G. Modugno, G. Roati, C. Fort, and M. Inguscio. Scissors mode of an expanding bose-einstein condensate. *Phys. Rev. A*, 67:023608, 2003.

- [83] G. Hechenblaikner, E. Hodby, S. A. Hopkins, O. M. Maragò, and C. J. Foot. Direct observation of irrotational flow and evidence of superfluidity in a rotating bose-einstein condensate. *Phys. Rev. Lett.*, 88:070406, 2002.
- [84] N. Sepúlveda, C. Josseland, and S. Rica. Superfluid density in a two-dimensional model of supersolid. *The European Physical Journal B*, 78(4):439–447, 2010.
- [85] M. J. Wright, S. Riedl, A. Altmeyer, C. Kohstall, E. R. Sánchez Guajardo, J. Hecker Denschlag, and R. Grimm. Finite-temperature collective dynamics of a fermi gas in the bec-bcs crossover. *Phys. Rev. Lett.*, 99:150403, 2007.
- [86] R. N. Bisset, P. B. Blakie, and S. Stringari. Static-response theory and the roton-maxon spectrum of a flattened dipolar bose-einstein condensate. *Phys. Rev. A*, 100:013620, 2019.
- [87] Giovanni I. Martone, Tomoki Ozawa, Chunlei Qu, and Sandro Stringari. Optical-lattice-assisted magnetic phase transition in a spin-orbit-coupled bose-einstein condensate. *Phys. Rev. A*, 94:043629, 2016.
- [88] Thomas M. Bersano, Junpeng Hou, Sean Mossman, Vandna Gokhroo, Xi-Wang Luo, Kuei Sun, Chuanwei Zhang, and Peter Engels. Experimental realization of a long-lived striped bose-einstein condensate induced by momentum-space hopping. *Phys. Rev. A*, 99:051602, 2019.
- [89] B.D. Josephson. Possible new effects in superconductive tunnelling. *Physics Letters*, 1(7):251 – 253, 1962.
- [90] S. Raghavan, A. Smerzi, S. Fantoni, and S. R. Shenoy. Coherent oscillations between two weakly coupled bose-einstein condensates: Josephson effects, π oscillations, and macroscopic quantum self-trapping. *Phys. Rev. A*, 59:620–633, 1999.
- [91] Michael Albiez, Rudolf Gati, Jonas Fölling, Stefan Hunsmann, Matteo Cristiani, and Markus K. Oberthaler. Direct observation of tunneling and nonlinear self-trapping in a single bosonic josephson junction. *Phys. Rev. Lett.*, 95:010402, 2005.
- [92] G. Spagnolli, G. Semeghini, L. Masi, G. Ferioli, A. Trenkwalder, S. Coop, M. Landini, L. Pezzè, G. Modugno, M. Inguscio, A. Smerzi, and M. Fattori. Crossing over from attractive to repulsive interactions in a tunneling bosonic josephson junction. *Phys. Rev. Lett.*, 118:230403, 2017.
- [93] J. Hertkorn, F. Böttcher, M. Guo, J. N. Schmidt, T. Langen, H. P. Büchler, and T. Pfau. Fate of the amplitude mode in a trapped dipolar supersolid. *Phys. Rev. Lett.*, 123:193002, 2019.
- [94] C. Ravensbergen, V. Corre, E. Soave, M. Kreyer, S. Tzanova, E. Kirilov, and R. Grimm. Accurate determination of the dynamical polarizability of dysprosium. *Phys. Rev. Lett.*, 120:223001, 2018.

- [95] Phillip L. Gould, George A. Ruff, and David E. Pritchard. Diffraction of atoms by light: The near-resonant kapitza-dirac effect. *Phys. Rev. Lett.*, 56:827–830, 1986.
- [96] Bryce Gadway, Daniel Pertot, René Reimann, Martin G. Cohen, and Dominik Schneble. Analysis of kapitza-dirac diffraction patterns beyond the raman-nath regime. *Opt. Express*, 17(21):19173–19180, 2009.